Forschungsbericht 2020-25

Modeling of stratospheric transport time distributions for inert and chemically active species

Frauke R. L. Fritsch

Deutsches Zentrum für Luft- und Raumfahrt
Institut für Physik der Atmosphäre
Oberpfaffenhofen

Dissertation
an der Fakultät für Physik
der Ludwig-Maximilians-Universität

105 Seiten
63 Bilder
5 Tabellen
72 Literaturstellen

Deutsches Zentrum
DLR für Luft- und Raumfahrt

Erstgutachterin: Prof. Dr. Hella Garny
Zweitgutachter: Prof. Dr. Thomas Birner
Datum der Abgabe: 25.05.2020
Datum der mündlichen Prüfung: 09.07.2020

MODELING OF STRATOSPHERIC TRANSPORT TIME DISTRIBUTIONS FOR INERT AND CHEMICALLY ACTIVE SPECIES

Frauke R. L. Fritsch

Dissertation

an der Fakultät für Physik

der Ludwig–Maximilians–Universität München

vorgelegt von

Frauke R. L. Fritsch

aus Essen

München 2020

Erstgutachterin: Prof. Dr. Hella Garny

Zweitgutachter: Prof. Dr. Thomas Birner

Datum der der Abgabe: 25.05.2020
Tag der mündlichen Prüfung: 09.07.2020

Contents

Publications **xi**

Zusammenfassung **xii**

Abstract **xiii**

1 Introduction **1**

1.1 Motivation 1

1.2 Aims 2

2 Scientific Background **3**

2.1 The Brewer-Dobson circulation 3

2.2 Tracer Species 5

2.2.1 Sulfur hexafluoride - SF_6 5

2.2.2 Ozone and ozone depleting substances 6

2.3 Transport time distributions and diagnostics 7

2.3.1 Inert case - Age of Air 8

2.3.2 Integrated path assumption 12

2.3.3 EESC calculation 13

3 Model Description and Set-ups **17**

3.1 EMAC 17

3.2 Model implementation of chemically depleted spectra 18

3.2.1 Time varying, non-transient transport time distributions 18

3.2.2 Cheap, easy loss for Pulses 20

3.3 Set-ups 22

3.3.1 RC1-base-07 22

3.3.2 slicePul 22

3.3.3 tranPul 22

3.3.4 chemPul-2000 and chemPul-2050 23

4 Mean Age of Air trend evaluation **25**

4.1 Age spectra 25

4.1.1 Sensitivity of mean AoA and AoA trends on parameter choice in the fit method 27

4.2 AoA calculations via the Convolution Method 34

4.3 Discussion 35

4.3.1 Model Results 35

4.3.2 Recalculation of AoA from balloon borne observations 36

4.4 Conclusions 38

5 Transit time distributions of chemically depleted species 39
5.1 Age of Air measures in the year 2000 39
5.2 Discussion of the local path integrated lifetime 41
5.3 Discussion 47
5.3.1 Mean AoA and Lifetime 47
5.3.2 EESC 48
5.4 Conclusion 51

6 Impact of changing climate on transport time distributions 53
6.1 Changes in dynamics 53
6.2 Comparison of representative N_2O and ODS of 2000 and 2050 56
6.3 Changes in transport and depletion diagnostics 62
6.4 Relevance to mixing ratio projection 70
6.5 Discussion 72

7 Concluding Remarks 77
7.1 Summary and Conclusions 77
7.2 Outlook 79

Acronyms 80

Bibliography 83

Danksagung 90

List of Figures

2.1 Schematic sketch Brewer-Dobson circulation 4
2.2 Globally averaged SF_6 time series on the ground. 5
2.3 Sketch of theoretical transport time distributions. 8
2.4 Example age spectra 9
2.5 Example Mean Age 10
2.6 Sketch fraction of input 11
2.7 Illustration path dependent Loss 12
2.8 Illustration transport time distribution of a tracer with constant lifetime. . . . 13

3.1 Illustration to explain derivation of spectra from pulses. 18
3.2 Error of mean spectrum when considering four spectra. 19
3.3 Cumulative standard deviation of mean spectrum when considering four pulse sets. 20
3.4 Comparison of method to prescribe loss. 21

4.1 Age spectra at $59°$ N and 106 hPa from the tranPul simulation. 26
4.2 Mean ratio $^{\Delta^2}/_{\Gamma}$ derived from age spectra in the tranPul simulation. 26
4.3 Trends in mean AoA at 40° N using the fit method with different parameters. . 27
4.4 Deviation of mean AoA using the fit method for different parameters and the difference in trends 28
4.5 Ratio of moments at 20 hPa and 40° N 29
4.6 Trends of mean AoA using the fit method 30
4.7 Mean AoA and its trend at 20 hPa and $40°$ N using the fit method and their differences. 31
4.8 Coefficients of the second order polynomial fit to the reference time series. . . 32
4.9 Lag time τ for fit interval length 9 to 15 years at 20 hPa and $40°$ N 32
4.10 Mean AoA for the range of magnitude of the coefficients a and b using a fixed τ. 33
4.11 Mean AoA and its trend using the convolution method at 20 hPa and $40°$ N and the differences. 34
4.12 Deviation of mean AoA using the convolution method with different widths and the difference in trends 35
4.13 Trend in AoA from the observations for the respective methods and parameters. 36
4.14 Example AoA time series from the observations and the spread for the respective parameters and methods. 37

5.1 Seasonal Γ from age spectra. 39
5.2 Relative difference of Γ from Spectra and a linear tracer 40
5.3 Monthly standard deviation σ of Γ from linear tracer. 41
5.4 Γ and $\bar{\tau}$ for N_2O. 42
5.5 Γ vs. $\bar{\tau}$ for N_2O. 43
5.6 Γ vs. $\bar{\tau}$ for CH_3Br. 43
5.7 $G(t)$ and $\tau(t)$ for $\Gamma = 3$ years for CF_2Cl_2 for DJF. 44
5.8 Seasonal mean Δ^2 of the age spectrum. 44

5.9 Seasonal mean Δ^2/Γ of the age spectrum. 45
5.10 Comparison calculating mixing ratio using $\bar{\tau}$ 46
5.11 Seasonal difference calculating mixing ratio using $\tau(t)$ 47
5.12 EESC for $\Gamma = 3$ years for assumed and modeled G and $G^{\#}$ 50
5.13 Mean AoA vs. mean fractional release for $CFCl_3$ and CH_3CCl_3. 51

6.1 Seasonal mean u for the chemPul-2000 simulation. 53
6.2 Seasonal mean difference of u of the chemPul simulations. 54
6.3 Seasonal Ψ^* for chemPul-2000. 55
6.4 Seasonal mean difference of Ψ^* of the chemPul simulation. 55
6.5 Boundary conditions 2000 and 2050 56
6.6 Relative change in mixing ratio for N_2O. 58
6.7 Relative change in mixing ratio for CF_2Cl_2. 58
6.8 Overview plot to mark regions. 59
6.9 Absolute change in mixing ratio for N_2O. 60
6.10 Relative loss of N_2O. 61
6.11 Difference of relative loss of N_2O. 62
6.12 Difference Γ 2050-2000. 63
6.13 Change in fraction of air younger than 0.5 years. 64
6.14 Change in fraction of air older than 2 years. 64
6.15 Change in fraction of air younger than 3.5 years. 65
6.16 Change in fraction of air older than 5 years. 66
6.17 Change in $\bar{f}$ of CF_2Cl_2. 67
6.18 Relative change in $\bar{\tau}$ for CF_2Cl_2. 68
6.19 Relative change in $\bar{\tau}$ for CH_3Br. 68
6.20 Transport distributions of CF_2Cl_2 in MAM in the NH LMS. 69
6.21 Difference of 2050 projected CF_2Cl_2 mixing ratio using G^*_{2000} and G^*_{2050}. 70
6.22 Difference of projected EESC using $G^{\#}_{2000}$ and $G^{\#}_{2050}$ and the respective $G^{\#}$. . . 71
6.23 EESC for $\Gamma = 3$ years for assumed and modeled $G^{\#}$ for 2000 and 2050. 72
6.24 Seasonal relative change in ClO_X between 2000 and 2050. 74

List of Tables

3.1 Years of pulses in chemPul simulations. 23
3.2 Species considered in the chemPul simulations. 24

4.1 AoA trends recalculated from observations using fit and convolution method. 36

5.1 Γ^{*}, $\Gamma^{\#}$ and $\bar{f}$ from inverse Gaussian and Model. 49

6.1 Boundary condition mixing ratios in chemPul simulations. 57

Publications

Parts of the results of this work were previously published in the following preprint and are reprinted here, in particular in Chapter 4. The paper is already accepted.

- Fritsch, F., Garny, H., Engel, A., Bönisch, H., and Eichinger, R. (2019). **Sensitivity of age of air trends on the derivation method for non-linear increasing tracers.** Atmospheric Chemistry and Physics Discussions, [Fritsch et al., 2019]

Further, results of some of the simulation already contributed to the publication

- Hauck, M., Fritsch, F., Garny, H., and Engel, A. (2019). **Deriving stratospheric age of air spectra using an idealized set of chemically active trace gases.** Atmospheric Chemistry and Physics, [Hauck et al., 2019]

Zusammenfassung

Die Atmosphäre ist einem sich ändernden Klima unterworfen, welches aufgrund der Zirkulationsänderungen Verteilungen von Spurengasen beeinflusst. Da diese Spurengase mit Strahlung und Chemie wechselwirken, ist ein Verständnis ihrer gegenwärtigen und zukünftigen Verteilung wichtig. Dieses Verständnis beruht auf der Interpretation dynamischer und chemischer Einflüsse. Während Klima-Chemiemodell (CCM) leicht Kenngrößen dieser Einflüsse liefern, stützen sich Beobachtungen auf abgeleitete Diagnostiken, welche Annahmen erfordern. Insbesondere anhaltende Diskrepanz zwischen beobachteten und modellierten Trends der mittleren Transitzeit geben Anlass zur Untersuchung dieser Annahmen.

Die vorliegende Arbeit konzentriert sich auf Diagnostiken von Transport und Chemie der Stratosphäre, die auf Transportzeitverteilungen von inerten und chemisch abgebauten Spurengasen basieren. Effektiv verbinden Transportzeitverteilungen als Greensche Funktion Spurengasmischungsverhältnisse zwischen zwei Punkten. Daher wurden die Transportzeitverteilungen eines inerten Tracers und ozonabbauender Substanzen (ODS), wie z.B. Fluorchlorkohlenwasserstoffe und Distickstoffoxid (N_2O), in einem Klima-Chemiemodell implementiert. Im Falle eines inerten Tracers ist die Transportzeitverteilung das Altersspektrum.

Zunächst wurden die Ableitung der mittleren Transportzeit, das mittlere Alter der Luft (AoA), und dessen Trend aus einem nichtlinear ansteigenden Tracer ähnlich Sulfurhexafluorid (SF_6) untersucht. Es konnte gezeigt werden, dass sowohl für das modell- als auch für das beobachtungsbasierte mittlere AoA systematische Fehler im Trend gefunden werden, welche abhängig von den Annahmen über das Altersspektrum bei der Altersableitung sind. Wenn Werte des Verhältnisses von erstem und zweitem Moment des Altersspektrums von 1,25-2,0 Jahre anstatt von wie bisher 0,7 Jahre angenommen werden, können modellierte und beobachtete Trends von mittlerem AoA in mittleren Breiten innerhalb ihrer Varianz übereinstimmen. Diese Werte des Verhältnisses der Momente werden durch die simulierten Altersspektren, den simulierten SF_6 Tracer und Literatur bestätigt.

Als nächstes wurden die Transportzeitverteilungen für ODS in einem Gegenwartsszenario untersucht. Daraus abgeleitet konnte der Zusammenhang von mittlerem AoA und pfandintegrierter Lebenszeit betrachtet werden. Hierbei konnte gezeigt werden, dass die pfadintegrierte Lebenszeitannahme von [Schoeberl et al., 2005] für die Projektion der Spurengaseverteilungen eine gute Annäherung in der Stratosphäre ist, mit Ausnahme der außertropischen Stratosphäre unmittelbar über 100 hPa. Der mittlere fractional release, der zum ersten Mal explizit in einer CCM-Simulation berechnet wurde, ist im Vergleich zu früheren Schätzungen, die auf einfachen Annahmen basierten, größer.

Im letzten Schritt wurden die Transportzeitverteilungen in Jahr 2000 und 2050 Klimazuständen verglichen. Mit Hilfe des mittleren AoA, des mittleren fractional release und der pfadintegrierten Lebenszeit konnten Zusammenhänge zwischen Transportveränderungen und Spurengasemischungsverhältnissen erklärt werden. Dies ist einzigartig, da so der Effekt des Transports auf die effektive Änderung des Mischungsverhältnisses eines chemisch abgebauten Spurengases isoliert werden kann. Für den Großteil der Stratosphähre wurde eine Abnahme des mittleren fractional release festgestellt. Am auffälligsten bei den Ergebnissen ist der Anstieg des mittlere AoA im Südsommer aufgrund des verzögerten Zusammenbruchs des Polarwirbels, der zu einem Anstieg des fractional release der ODS führt. Dies könnte auf eine Verzögerung der Erholung des Ozonlochs hindeuten.

Abstract

The atmosphere is subject to changing climate which influences tracer distributions due to the changes in global circulation. As those tracers interact with radiation and chemistry, it is important to understand their present and future distributions in the stratosphere. This understanding relies on the interpretation of dynamical and chemical processes. While chemistry climate models (CCM) readily provide measures of those processes, observations rely on derived diagnostics which often require assumptions. Especially the long standing disagreement of observed and modeled circulation trends as measured by the mean transit time give rise to detailed investigation of said assumptions.

The present work focuses on diagnostics of stratospheric transport and chemistry that are based on transport time distributions of inert and chemical depleted tracers. Effectively, transport time distributions as Greens functions connect tracer mixing ratios between two locations. Therefore, transport time distributions of an inert tracer and ozone depleting substances (ODS), such as chlorofluorocarbons and nitrous oxide (N_2O), were implemented in a CCM. In the case of an inert tracer, the transit time distribution is the so-called age of air spectrum.

First, the derivation of the mean transit time, the mean age of air (AoA), and its trend from a non-linear increasing sulfur hexafluoride (SF_6) like tracer were investigated. It could be shown, that for both, model and observation based mean AoA, systematic errors were found in the trend depending on the assumptions about the transit time distribution as part of the age derivation. If the ratio of first and second moment of the transit time distribution is shifted to values of 1.25-2.0 years instead of 0.7 years as assumed previously, modeled and observed mid-latitude mean AoA trends can agree within their margins of error. Those values of the ratio of moments are confirmed by the simulated age spectra, the modeled SF_6 tracer and literature.

Secondly, the transit time distributions for chemically active tracers, namely ODS, were investigated in a present day scenario. Obtained by that, the relation between mean AoA and path integrated lifetime could be investigated. In doing so, it could be shown, that the path integrated lifetime assumption by [Schoeberl et al., 2005] for the projection of tracer distribution is a good approximation in the stratosphere, except for the extratropical stratosphere right above 100 hPa. The mean fractional release as explicitly calculated for the first time from a CCM simulation is found to be larger compared to previous estimates based on simple assumptions.

In the last step, the transit time distributions were compared in year 2000 and 2050 climate conditions. By means of mean AoA, mean fractional release and path integrated lifetime, connections between transport changes and tracer mixing ratio changes could be explained. This is unique, as this allows to isolate the effective change of the mixing ratio of a chemically depleted tracer due to transport changes. For most of the stratosphere, an decrease in mean fractional release was found. Most noticeably among the results is the increase in mean AoA in the southern summer due to the delayed break-down of the polar vortex leading to an increase in fractional release of ODS. This might impact the recovery of the ozone hole.

Chapter 1

Introduction

1.1 Motivation

The climate of the earth is subject to change. One the one hand, due to continuous emission of greenhouse gases (GHG) such as carbon dioxide (CO_2), methane (CH_4) and nitrous oxide (N_2O) that lead to warming of the troposphere due to absorption and re-emission of long wavelength radiation. One the other hand due to the recovery of ozone thanks to the restriction of the emission of halogenated organic compounds. Ozone is important to humanity as it absorbs ultraviolet (UV) radiation in the stratosphere which is harmful to humans. In addition to the ozone depleting potential of halogenated organic compounds, some of them are also very potent GHG, even though their abundance is not as high as CO_2, CH_4 or N_2O.

Now as the climate changes, it is of scientific interest to know, how the distribution of trace gas species will evolve, considering e.g. the aforementioned impact of the halogenated organic compounds on radiative heating and ozone chemistry. To understand trace gas distributions both are required knowledge about transport and chemical reactions of the trace gases. Transport in the stratosphere is strongly determined by the Brewer-Dobson circulation (BDC), which is the slow meridional overturning mass circulation. The thermodynamically driven temperature changes lead to changes in the BDC. Those circulation changes are far more uncertain than the directly thermodynamically driven temperature changes [Shepherd, 2014].

In case of the present work, the primary focus is on the trace gases sulfur hexafluoride SF_6, organic halogenated compounds and N_2O. Concerning SF_6 it is most interesting to study it as a tracer of stratospheric transport. The strength of the BDC is deduced from trace gases mixing ratios since the transport velocities cannot be measured directly. The other chemical species pose scientific interest due to their aforementioned radiative impact and their ozone depleting potential. Usually, time series of those tracer emissions are well studied on the surface. However, in a balloon or airborne measurement scenario, a volume mixing ratio or concentration of a tracer at a certain time and location might be available. Often enough, this information is fairly sparse.

Therefore, various evaluation methods are in place, to deduce as much information as possible about the transport and the chemical interaction that the tracer has been subject to between both locations and times. The main focus of the present work are methods that are derived from Green's functions. That means that the mathematical propagator of the differential equation is considered which describes how the mixing ratio at reference location and time and observation location and time are connected due to the respective transport and chemical depletion. Thus, a transport time distribution for the tracer under investigation is determined. This theoretical framework allows formulating diagnostics of stratospheric transport, like the mean transport time, called mean Age of Air (AoA), and diagnostics of the chemical depletion along an air parcel's path, such as the path integrated lifetime. Those diagnostics have the advantage that they can be derived from trace gas measurements. However, to apply those concepts to trace gas measurements requires sound assumptions. Interestingly enough, models and observations struggle to agree about the trend in mean AoA inflicted by climate change in the mid-latitude mid-stratosphere.

In a global chemistry climate model, the full information about the climate system is available. In addition, various types of diagnostics, such as the respective Green's function, can be implemented and modeled directly. This means, that those transport time distributions can be modeled for inert tracers, chemical depleted tracers and their products. Thus, a model can be used to evaluate and optimize the assumptions and methods that are applied to derive further information about transport and depletion from observational data.

Investigating said assumptions is specifically interesting as there are open questions when bringing together models and observations. For instance, as the temporal trend of their transport measures disagrees, it is even more so difficult to understand how a tracer propagates that is affected by both, transport and chemistry. So eventually, the understanding of the connection of reference mixing ratio, transport and chemistry and observed mixing ratio of the considered trace gases shall be improved.

1.2 Aims

To paraphrase the concepts in the previous section into specific aims for this work, those shall be

- Are the currently used assumptions about the transport time distribution for an inert tracer valid? Are there systematic effects when deriving transport times (mean AoA) that result in uncertainties in trends?
- How do transport time distributions for chemically depleted tracers differ from those of inert tracers? How well do simple assumptions such as a path integrated lifetime hold?
- What can transport time distributions tell about distributions of tracers and their products in a changing climate and how are they affected themselves?

Chapter 2

Scientific Background

The structure of earth's atmosphere is determined by the interplay of radiation, chemical reactions and dynamical processes. According to the change in temperature gradient, the atmosphere can be split into different layers. The temperature in the first layer, the troposphere is determined by heating from earth's surface as it absorbs radiation, which results in decreasing temperatures with altitude. The temperature in the second layer, the stratosphere, is dominated by heating from ozone (O_3) that absorbs UV radiation. This heating leads to an increase of temperature with altitude. The continuous emission of gases that absorb long wavelength radiation, such as CO_2, N_2O and CH_4, leads to warming in the troposphere and cooling in the stratosphere.

When analyzing the resulting trends of meteorological variables due to those emissions, other modulations of inter-annual variability might be considered. Mentioned here is first the solar cycle which is the change of sun activity with a period of roughly ten years. Further, the quasi-biennial oscillation (QBO) should be mentioned. The QBO is present in the stratospheric equatorial zonal wind and caused by interactions of atmospheric waves with the mean flow.

The important chemical and dynamical processes in the stratosphere shall be discussed in the next sections.

2.1 The Brewer-Dobson circulation

The dynamics in the stratosphere are described by the Brewer-Dobson circulation which is given as a sketch in Fig.2.1). The concept of the circulation was first proposed by Brewer and Dobson [Brewer, 1949, Dobson et al., 1929]. By a meridional equator to pole mass circulation, the abundance of ozone in the extratropics could be explained as most ozone is produced in the tropics because of the higher insolation.

In Fig. 2.1, the upwelling of air in the tropics can be recognized where the tropopause is located higher. The poleward motion in the lower stratosphere is the shallow branch of the BDC. In the upper stratosphere, the deep branch can be identified. Further, orange arrows indicate mixing, while turquoise bars indicate mixing barriers. Mixing is large-scale quasi-horizontal stirring by breaking planetary waves and subsequent three-dimensional turbulent diffusion that leads to two-way irreversible mass exchange [McIntyre and Palmer, 1984]. The BDC is driven by waves that deposit momentum as they break and dissipate. The major part is contributed by planetary waves that deposit momentum in the middle and upper stratosphere. Those waves originate from the conservation of potential vorticity, which is equivalent to conservation of rotational momentum. High up in the stratosphere and above in the mesosphere, gravity waves contribute momentum to the meridional circulation. Gravity waves are called so as gravity is their restoring force.

In models, the advective part of the Brewer-Dobson circulation can be inferred from the transformed Eulerian mean (TEM) equations. In this case, the zonal mean meridional and

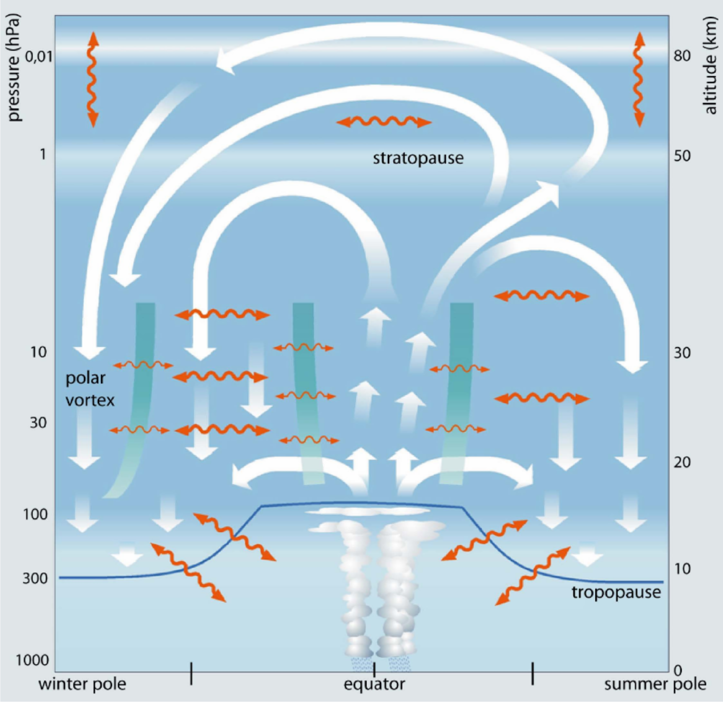

Figure 2.1: Schematic sketch of the Brewer-Dobson circulation taken from [Bönisch et al., 2011]. The white arrows indicate residual transport, orange arrows indicate mixing and turquoise bars indicate mixing barriers

vertical wind $\bar{v}$ and $\bar{w}$ are transformed to the residual circulation $\bar{v}^*$ and $\bar{w}^*$. This means, that the adiabatic part of the circulation is subtracted. This adiabatic part is compensated by eddy heat fluxes by steady propagating waves and thus leads to no net temperature change and no net transport. Hence, the residual circulation is equivalent to the mean net mass transport.

By means of integrating

$$p_0\bar{v}^* = -\frac{\partial\Psi^*}{\partial z} \quad \text{and} \quad p_0\bar{w}^* = \frac{\partial\Psi^*}{\partial y} \tag{2.1}$$

the mass-weighted residual streamfunction Ψ^* can be obtained which provides the contours of transport [Andrews et al., 1987], though the integration of w^* by y is often omitted.

As the required information about the atmospheric state cannot be measured continuously, rather the mean transit time between two locations, also called mean Age of Air, is used to diagnose the BDC. Different approaches to infer mean AoA from trace gas measurements will be explained in the later sections of this chapter. Species often considered as AoA tracers are SF_6 and CO_2 [Andrews et al., 2001, Engel et al., 2009]. So far, both satellite and balloon borne observations show positive trends in mean AoA with time in NH mid-stratosphere mid-latitudes [Engel et al., 2017, Stiller et al., 2012, Haenel et al., 2015, Bönisch et al., 2011]. In contrast, global chemistry-climate models very consistently show negative mean AoA trends [Oberländer et al., 2013, Shepherd and McLandress, 2011, Garcia and Randel, 2008]. Therefore better understanding of the uncertainties when deriving AoA is necessary. Previous work already provided great insight to the uncertainties of mean AoA itself, such as [Garcia et al., 2011, Ray et al., 2014, Leedham Elvidge et al., 2018], though the mean AoA trend has still remained subject to discussion. To understand future climate it is necessary to know how the

BDC will change as the distribution of tracers depends on the BDC and those impact radiation and chemical reactions. Therefore, the differences in mean AoA trend as a diagnostic need to be better explained.

2.2 Tracer Species

2.2.1 Sulfur hexafluoride - SF_6

Sulfur hexafluoride is a long lived trace gas of anthropocentric origin. It is utilized as a gaseous dielectric medium in the electrical industry. Fig. 2.2 gives the boundary condition time series as it is assumed with the simulations and the considered observations in this work. As the time series is monotonically increasing and SF_6 is long lived, it is well suited for studies of atmospheric transport from observations.

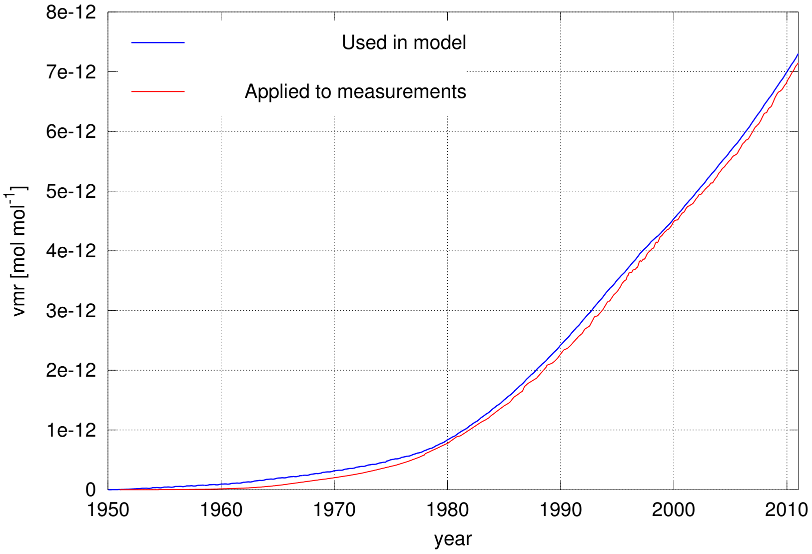

Figure 2.2: Globally averaged SF_6 time series on the ground as used in the simulations (blue) and as used with the observations mean AoA calculations (red).

The SF_6 time series prescribed in the simulation is based on smoothed ground measurements for the past and on the RCP 6.0 scenario [Eyring et al., 2013] for the future. The SF_6 time series assumed for analysis from measurements is based on [Levin et al., 2010, Maiss and Levin, 1994]. From 1978 on, the SF_6 time series is well constrained by NOAA measurements at Cape Grim. Before that, SF_6 is estimated from emissions. Prior to 1961, the data is linearly extrapolated. Both SF_6 time series differ slightly, as can be seen from Fig. 2.2. The differences will be considered accordingly when necessary in Chapter 4. Overall, for the measures considered in this work, the small differences in SF_6 time series pose no relevant impact.

SF_6 is long lived, as it primarily has mesospheric sinks. There, SF_6 is depleted by photolysis and electron attachment. The estimated range of the lifetime of SF_6 is fairly large. Until not too long ago, a typical estimate of the lifetime would be 3200 years, though more recent work suggests that it is lower. Both [Leedham Elvidge et al., 2018] and [Ray et al., 2017] find the lifetime of SF_6 to be rather lower, namely 850 years. A shorter lifetime of SF_6 also requires an reassessment of the bias in mean AoA which varies across the atmosphere. A shorter lifetime leads to a larger mean AoA bias if SF_6 is assumed to be inert for the mean AoA derivation. SF_6 is depleted in the mesosphere, the depleted air moves into the polar vortex and spreads throughout the stratosphere, as the vortex breaks down. In the mid-latitude region, which is most relevant region in the discussions of the upcoming chapters, the recent estimate of the mean AoA bias by [Ray et al., 2017] is around 0.75 years.

2.2.2 Ozone and ozone depleting substances

As mentioned before, ozone (O_3) is important due to its absorption of harmful UV radiation in the stratosphere. By the BDC, ozone is distributed across all latitudes.

Mainly, ozone is produced in the equatorial stratosphere by photolysis of molecular oxygen by UV photons of wavelength less than 240 nm. The amount of ozone O_3, relative to atomic oxygen O_2 is controlled by chemical equilibrium. However, the amount of O_3 in the stratosphere would be higher, if this was the only reaction to consider. In addition, there are several catalytic cycles, that reduce the amount of O_3. This means, that a molecule X can reduce several molecules of O_3 as it is not removed due to the reaction.

$$\begin{aligned} X + O_3 &\longrightarrow XO + O_2, \\ XO + O &\longrightarrow X + O_2, \\ \text{Net:} \quad O + O_3 &\longrightarrow 2O_2 \end{aligned}$$

The catalyst might even have a low atmospheric abundance. Well know catalytic cycles of ozone are hydrogen oxide radicals HO_X ($H + OH + HO_2$) and nitrogen oxides NO_X ($NO + NO_2$). Of particular interest here are the halogen cycles, in particular of chlorine (Cl) and bromine (Br). Stratospheric active bromine and chlorine originates from long-lived halogen containing organic species that have historically been emitted. As the chlorine and bromine catalytic cycles are relatively fast and especially bromine is very effective in depleting ozone, the emission of halogenated organic compounds lead to a reduction of the ozone layer throughout the stratosphere.

Though, the most pronounced reduction in ozone is in the SH polar spring, which is primarily because of polar stratospheric ice clouds (PSC). In the very cold polar vortex in SH winter, PSC can form. In comparison, the NH polar vortex is not as stable due to the differences in orography in NH and SH, which means that in the NH the temperatures usually are not low enough to meet the conditions for PSC. PSC provide the surface for heterogeneous chemistry, which leads to more rapid ozone destruction. Further, PSC allow for the sedimentation of nitrogen from the polar regions so that less nitrogen is available to form more stable reservoir gases from Cl and Br. Those different aspects lead to the observed ozone hole in the SH spring. The ozone hole leads to cooling in the polar regions and thereby to a delayed breakup of the polar vortex in spring [WMO, 2018].

After the discovery of the ozone hole [Molina and Rowland, 1974] the political action of the Montreal Protocol in 1987 and the consecutive agreements led to the reduction of the emission of these ozone depleting substances (ODS). Since then, research into the recovery of the ozone layer has been of scientific interest which includes model studies and projections from observations [Newman et al., 2007, Engel et al., 2018, WMO, 2018, Ball et al., 2019].

As a secondary effect to the ozone recovery, the reduction of ODS is also known to impact the BDC due to the opening and closing of the ozone hole [Polvani et al., 2019]. Half of the global, stratospheric mean AoA trend seen in models so far, might be caused by high ODS levels and reduces as ODS levels decrease. Further, [Abalos et al., 2019] could attribute a speeding up of the SH circulation to high ODS levels. Though, this effect is unclear in EMAC, the model used in this work, as [Eichinger et al., 2019] did not see a change in mean AoA trend with declining ODS. In addition to the impact of ODS on the BDC trend, recent findings indicate that the radiative forcing of ODS is particular strong in the arctic regions which contributes to the particular strong warming due to climate change in those regions [Polvani et al., 2020]. Also the connection the other way around, namely the impact of BDC trends on the ODS distribution and removal has already been subject to research [Butchart and Scaife, 2001]. In a simplified set-up, they investigated chlorofluorocarbons (CFCs) as one subgroup of ODS. They concluded that by enhanced mass exchange, CFCs would be removed quicker. Now it can be understood that, as ODS impact ozone and the BDC and the BDC impacts the distribution of ODS, it is highly interesting to closer study model diagnostics of transport and depletion of ODS.

2.3 Transport time distributions and diagnostics

Expressed very conceptually, considering the previous two sections, the dynamical and chemical regime in the atmosphere and specifically in the stratosphere leads to one tracer being emitted at a reference location referenced by the mixing ratio $\chi_0(t-\tau)$, being propagated in some way that leads to a certain tracer mixing $\chi(\boldsymbol{x},t)$ at a observation location $\boldsymbol{x}$, with τ being their time lag. Very generalized, this would be:

$$\chi_0(t-\tau) \rightarrow \text{some transport and depletion} \rightarrow \chi(\boldsymbol{x},t). \tag{2.2}$$

After a short introduction to this viewpoint, useful special cases will be considered later. Expressed more mathematical, in the case of an inert tracer both concentrations are connected via the Green's function of the transport G which is the age spectrum [Hall and Plumb, 1994].

$$\chi(\boldsymbol{x},t) = \int_0^\infty \chi_0(t-t')G(\boldsymbol{x},t')\mathrm{d}t'. \tag{2.3}$$

Now, in the case of a tracer, that predominantly is affected by chemical depletion and no production, this equation can be split up in the source and the product part as introduced and explained by [Ostermöller et al., 2017, Engel et al., 2018]. To do so, it is required, that the age spectrum can be split up into the source and product part, that are the arrival time distribution G^* and the release time distribution $G^\#$. That is simply the relation

$$G = G^* + G^\#. \tag{2.4}$$

Consequently, for the source part, the initial tracer, the mixing ratio equation can be written by means of the arrival time distribution as

$$\chi_{\text{source}}(\boldsymbol{x},t) = \int_0^\infty \chi_0(t-t')G^*(\boldsymbol{x},t')\mathrm{d}t' \tag{2.5}$$

and in the product case by applying the release time distribution

$$\chi_{\text{product}}(\boldsymbol{x},t) = \int_0^\infty \chi_0(t-t')G^\#(\boldsymbol{x},t')\mathrm{d}t'. \tag{2.6}$$

Furthermore, the age spectrum and the release time distribution are connected via the transit time dependent fractional release $f(t)$ or the transit time dependent lifetime $\tau(t)$:

$$G^{\#}(\boldsymbol{x},t) = f(\boldsymbol{x},t) \cdot G(\boldsymbol{x},t) = \left(1 - \exp\left(-{}^{t}/_{\tau(\boldsymbol{x},t)}\right)\right) \cdot G(\boldsymbol{x},t). \tag{2.7}$$

An simplified example sketch of the transport time distributions is provided in Fig. 2.3.

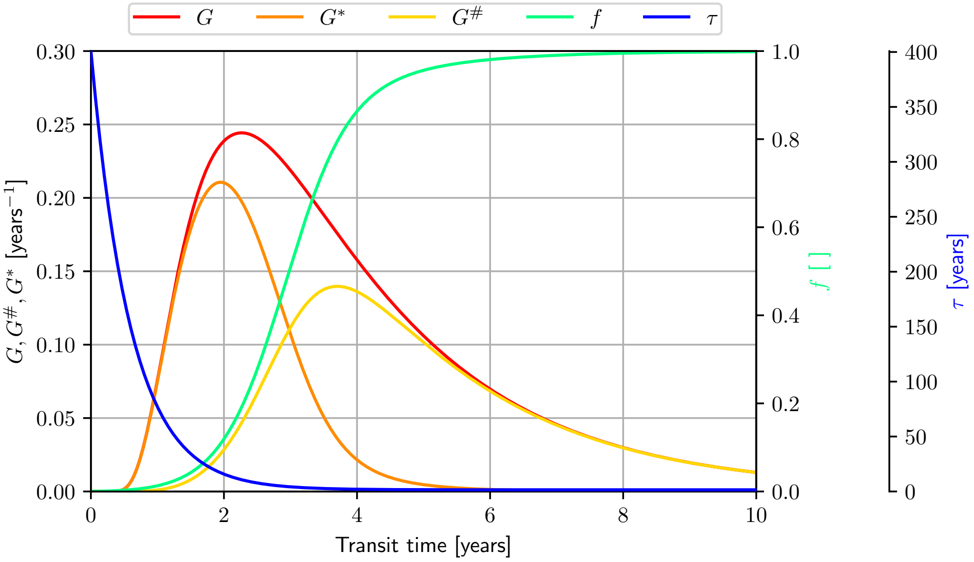

Figure 2.3: Conceptual sketch of theoretical transport time distributions $G, G^{\#}$ and G^*. In addition, matching transit time dependent fractional release $f(t)$ and lifetime $\tau(t)$ are given.

Most pioneering work about transit time distributions of chemically depleted tracers was focused on useful simplification of this framework that are required, as the Green's function cannot be measured directly. They rather originated from diagnostics with physical meaning, such as fractional release and mean Age of Air, and can now be sorted into this common framework. Those special cases will now be explained closer.

2.3.1 Inert case - Age of Air

The simplest special case is the case of an inert tracer. Assuming that the tracer is subject to no depletion, the age spectrum gives direct information about the transport of the tracer. It represents the distribution of transport times to the observation location. The first moment of this distribution is then called the mean Age of Air with the symbol Γ. This is written as

$$\Gamma = \int_0^\infty t' G(\boldsymbol{x},t')\mathrm{d}t'. \tag{2.8}$$

Mean AoA is a useful measure as it can be diagnosed from trace gas measurements. Different approaches to do so will be explained in the next subsections. Consequently, the second moment Δ of $G(t)$ is defined by

$$\Delta^2 = 0.5 \cdot \int_0^\infty (t' - \Gamma)^2 G(\boldsymbol{x},t')\mathrm{d}t'. \tag{2.9}$$

Pioneering work about AoA was done by [Hall and Plumb, 1994]. Based on a one dimensional diffusion analog they formulated the approximation for the age spectrum by an inverse Gaussian:

$$G(t) = \sqrt{\frac{\Gamma^3}{4\pi\Delta^2 t^3}} \cdot \exp\left(-\frac{\Gamma(t-\Gamma)^2}{4\Delta^2 t}\right). \tag{2.10}$$

Where Δ is the width of the age spectrum as defined before and t is the transit time. A sketch of an age spectrum for $\Gamma = 4$ years for this approximation is given in Fig. 2.4.

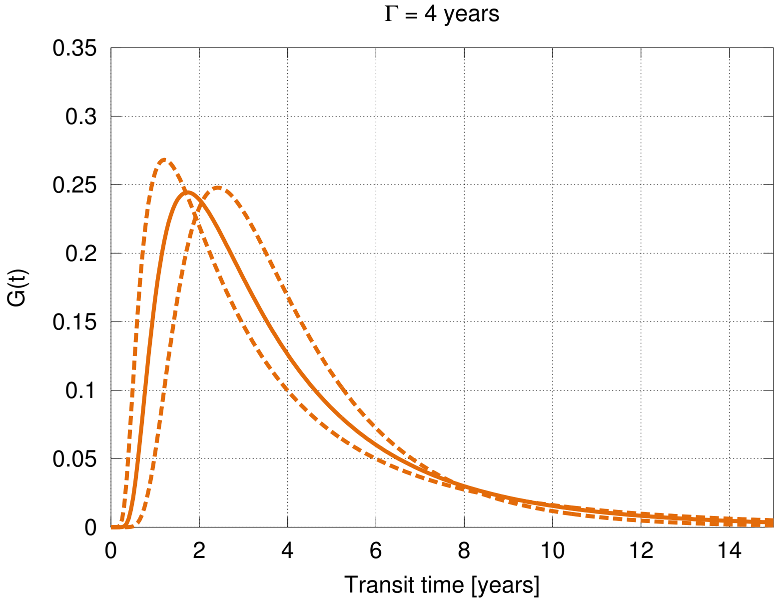

Figure 2.4: Example of a Age of Air spectra. Specifically, the spectra represent the inverse Gaussian for $\Gamma = 4$ years and $\Delta^2/\Gamma = 0.7, 1.25$ and 2.0 years (See Eq. 2.10)

Age of Air in models

In models a well-established way to derive mean AoA is from a linearly increasing inert tracer. In this case, the mean AoA at a point $\boldsymbol{x}$ is equal to the time lag τ of the tracer mixing ratio χ relative to the mixing ratio χ_0 at a selected reference area, which can be written as

$$\chi(\boldsymbol{x}, t) = \chi_0(t - \Gamma(\boldsymbol{x})). \tag{2.11}$$

An example of mean AoA from EMAC (See. Sec. 3.1) is given in Fig. 2.5.

As both, mixing and the residual transport impact the tracer distribution, their respective contributions to mean AoA can be studied. Further, the respective contributions to trends of mean AoA were investigated [Garny et al., 2014, Dietmüller et al., 2017].

Age Spectra in models

Considering Eq. 2.3 again, the Green’s function G of an inert tracer can be obtained from a delta peak in tracer concentration. In the case of a non-stationary atmosphere, i.e. one with seasons, a set of inert tracer pulses at a reference surface is required. This method was

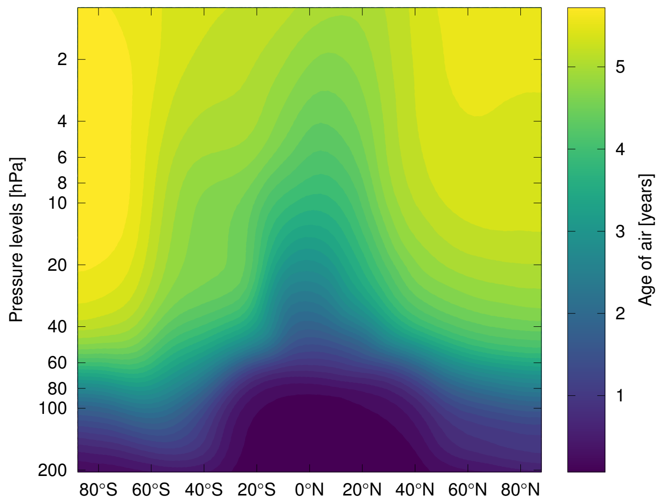

Figure 2.5: Example of mean Age of Air from a linear model tracer. Shown here is the July mean of year 2001-2010 from a transient, dynamics only EMAC simulation.

already described and implemented for different models in e.g. [Li et al., 2012] and [Ploeger and Birner, 2016]. [Li et al., 2012] implemented a fixed time scenario, with just one tracer pulse for every month for one year, leaving those pulses running for ten years. In contrast, [Ploeger and Birner, 2016] continuously released tracer pulses and thereby obtained time evolving age spectra. For this work, the latter concept was also introduced to EMAC.

Quadratic fit to the reference time series

In the observational scenario in the real world, no perfectly linear increasing inert tracer is available. Often, SF_6 is used as a proxy for such a tracer. As the SF_6 emissions increase non-linearly, a common approach to derive mean AoA is a second order approximation that considers the slope of the reference time series. The general concept of the derivation is described in [Volk et al., 1997]. [Engel et al., 2009] and [Engel et al., 2017] apply it as an iterative procedure to optimize the length of the fit interval to the reference time series. First, the second order fit is performed on the reference time series for a set fit interval, e.g. 15 years. This yields the polynomial coefficients a, b and c. The fit performed can be expressed either relative to the nominal time axis $\tilde{t}$ ranging from 1960 to 2011 and the reference time t_0 or by the transit time t (note the change in sign):

$$\chi_0(\tilde{t}) = a + b(\tilde{t} - t_0) + c(\tilde{t} - t_0)^2 = a - bt + t^2. \tag{2.12}$$

Secondly, a first guess for the mean age is calculated using the coefficients applying the equation

$$\Gamma = \frac{b}{2c} - 2 \cdot C_1 \pm \sqrt{\left(\frac{b}{2c} - 2 \cdot C_1\right)^2 + \tau^2 - \frac{b}{2c} \cdot \tau}. \tag{2.13}$$

Again, Δ is the width of the age spectrum and C_1 is the ratio of first and second moment of the age spectrum, i.e. $C_1 = {}^{\Delta^2}/_{\Gamma}$. C_1 parameterizes the width of the spectrum relative to its mean as the longer that air has been traveling, the more spread out the age spectrum will be. τ is the lag time between the mixing ratios χ and χ_0. To be consistent with [Engel et al., 2017], the lag time is determined by approximating the reference time series by a second order polynomial. In the third step, a fit interval t_{fit} is determined, which considers a given fraction of the age spectrum F, e.g. 98%. This can be written as:

$$\int_0^{t_{\mathrm{fit}}} G(t')\mathrm{d}t' \overset{!}{=} F. \tag{2.14}$$

To make the fraction of input better understandable, Fig. 2.6 sketches Eq. 2.14. Considering a given fraction F of the area enclosed by $G(t)$ gives a transit time that corresponds to this fraction, and this transit time is then used as backward fit interval to perform the fit on the reference time series. Thus the larger the fraction of input F the longer the fit interval. The age spectrum assumed in this step is the inverse Gaussian from Eq. 2.10. This equation uses the previous mean age value and the parameterization for the width. In the last step the value for the fit interval is used to determine once more the polynomial coefficients and recalculate the mean age value according to Eq. 2.13.

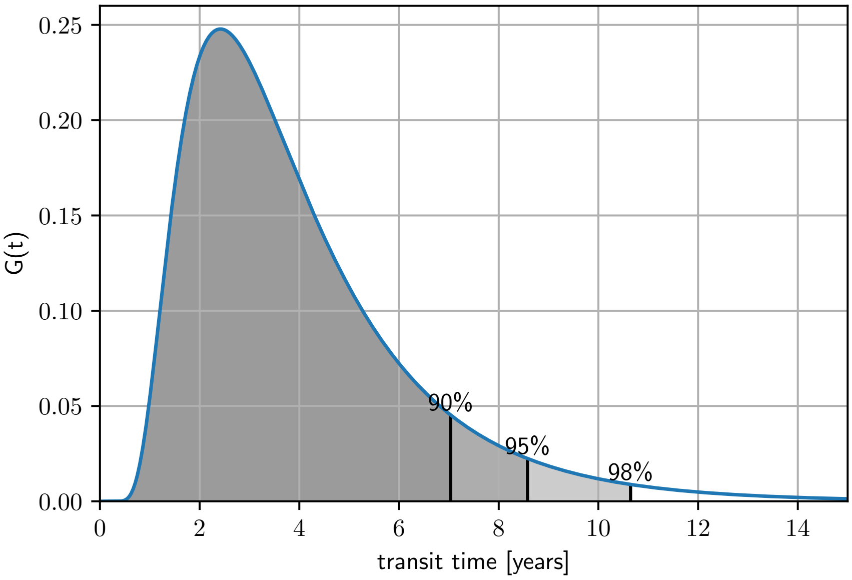

Figure 2.6: Sketch to explain the fraction of input. The resulting fit intervals for the fraction of input $F = 90\%$, 95% and 98% are sketched. Here, $G(t)$ is estimated from an inverse Gaussian, the example here is given for $\Gamma = 4\,\mathrm{years}$ and $\Delta^2 = 0.7 \cdot \Gamma$ (See Eq. 2.10).

To perform this procedure one needs to choose the reference point, the fraction of the considered input and the ratio of the moments. The aim will be to systematically test the sensitivity of the derived mean AoA and AoA trends on those parameters.

Convolution Method

Another method to infer mean AoA from a non-linear increasing tracer is using a numerical convolution. Considering Eq. 2.3, the reference time series χ_0 is convoluted with an assumed age spectrum G, i.e. Eq. 2.10 which gives an observed mixing ratio χ. Inserting different mean age values Γ into Eq. 2.10, creates a lookup table of mixing ratios $\chi(\Gamma)$ that can be compared to the actual observed mixing ratio to pick the appropriate mean age value. This approach requires one less assumption than the fit method as an assumption about the considered amount of reference input is not needed as the age spectrum weights the reference input according to the relative influence it has at the observed location. Therefore, the reference input can simply be considered for a long time interval, e.g. 25 years. Thus, this approach is expected to be quite physical and robust. [Ray et al., 2017] and [Leedham Elvidge et al., 2018] apply this approach to derive mean AoA from SF_6 and other non-linear increasing tracers, respectively. The AoA calculations in [Stiller et al., 2012] are also based on this concept, though they determine Γ by an iterative process rather than by a lookup table.

2.3.2 Integrated path assumption

The next specific case is that of a chemical depleted tracer which itself is supposed to be studied. That tracer is subject to different loss, depending on the path it takes. To make this more clear, Fig.2.7 shows a sketch of a mixing ratio χ_0 propagating to a different location $\boldsymbol{x}$ with a mixing ratio $\chi(\boldsymbol{x}, t)$. In the sketch, the air moves through different loss regions, symbolized here by the loss of Halon-1211 (CF_2ClBr) in July.

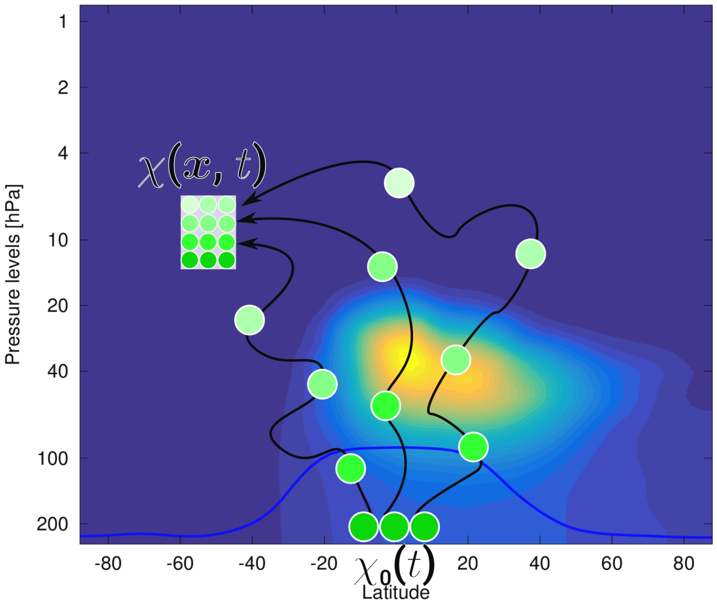

Figure 2.7: Conceptual illustration of the chemical loss air might be subjected to depending on the path taken. The background shows the depletion of Halon-1211 in July.

Based on this picture, [Schoeberl et al., 2005] proposed an integrated path assumption which assumes an average path integrated lifetime $\bar{\tau}$ for every location that represents the average depletion across the different paths. This concept was primarily assumed for photolysis as the cause of depletion which has a well-known spatial distribution.

Bearing in mind Eq. 2.4 and 2.7, G^* is exchanged by G as

$$G^*(\boldsymbol{x}, t) = \exp(-{}^{t}/_{\tau(\boldsymbol{x},t)}) \cdot G(\boldsymbol{x}, t). \tag{2.15}$$

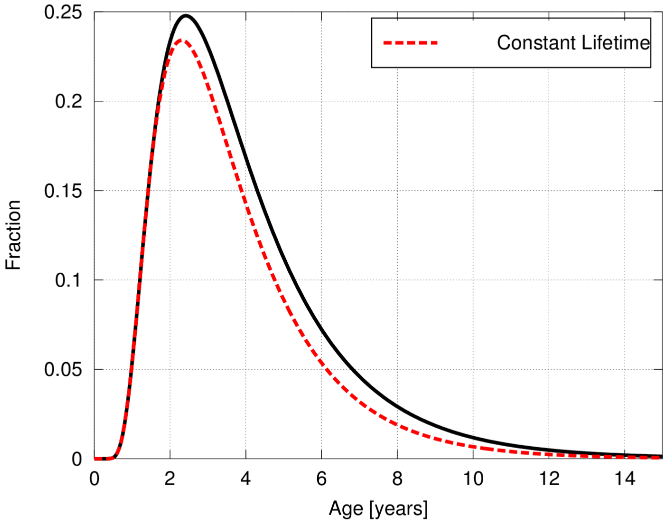

Figure 2.8: Illustration of the transport time distribution of a tracer with constant lifetime (red) and an inert age spectrum (black).

Then the transit time dependent lifetime $\tau(\boldsymbol{x}, t)$ is approximated by the path integrated lifetime $\bar{\tau}(\boldsymbol{x})$, where $\bar{\tau}$ is calculated as

$$\bar{\tau}(\boldsymbol{x}) = \int_0^\infty \tau(\boldsymbol{x}, t') \cdot G(\boldsymbol{x}, t')\mathrm{d}t'. \tag{2.16}$$

In that case, age spectrum G and arrival time distribution G^* are linked by a simple exponential decay as is illustrated in Fig 2.8. As $\bar{\tau}$ gives a lifetime at a location, it might be confused with the local lifetime. Though, this is just the inverse loss frequency at a location which is a different measure and can be obtained from models without further ado [Ko et al., 2013].

2.3.3 EESC calculation

Another relevant special case of tracer propagation is to study the chemical products of the tracers. In the case of ODS, the sum over several source species is of interest as they all lead to active stratospheric chlorine and bromine as products. Therefore, the concept of Equivalent Effective Stratospheric Chlorine (EESC) was developed. EESC considers the equivalent effect of both species, chlorine and bromine, for a sum of ODS. Further, EESC aims at representing the projected abundance of the amount of the species that is effectively acting on ozone. Therefore, EESC is common proxy for ozone depletion and recovery. The return of EESC values to (typically) 1980 values can then be referenced as a recovery date.

In the course of time, the calculation of EESC has been revised. Initially, [Daniel et al., 1995] determined EESC by the source gas mixing ratio ρ_i and the efficiency of stratospheric halogen release of the source gas f_i (in other discussions of the present work, f refers to a representation of fractional release). This results in the equation

$$\mathrm{EESC}(t) = a\left(\sum_{\mathrm{Cl}} n_i f_i \rho_i + \alpha \sum_{\mathrm{Br}} n_i f_i \rho_i\right). \tag{2.17}$$

Here, a can either be an arbitrary value or the fractional release of CFC-11 at a certain stratospheric region and in that case represent the amount of inorganic chlorine. In this formulation, ρ_i was assumed using a time lag from the surface observations. α considers the effectiveness of bromine in oxidizing ozone compared to chlorine. α is usually estimated to in the range 60-65 [WMO, 2018]. In the upcoming chapters, 60 is used. n_i simply refers to the number of halogen molecules contained in the molecule.

[Newman et al., 2006] and [Newman et al., 2007] aimed at making the EESC calculation more accurate. First, they estimated ρ applying an age spectrum. Second, instead of assuming the efficiency of stratospheric halogen release of the source gas, they determined a mean AoA dependent fractional release $f(\Gamma)$. In this case, the fractional release is estimated by deriving the mean AoA from an approximately inert tracer at an observation location. Using this mean AoA value, the boundary condition mixing ratio of the halogen containing species is propagated as $\chi_{\text{ref}}(\Gamma)$. The propagated value is then compared to the observed mixing ratio at the observation location $\chi_{\text{strat}}(\Gamma)$ to determine the fractional release dependent on mean AoA. This can be expressed as

$$f(\Gamma) = \frac{\chi_{\text{ref}}(\Gamma) - \chi_{\text{strat}}(\Gamma)}{\chi_{\text{ref}}(\Gamma)}. \tag{2.18}$$

Using this fractional release and the age spectrum, EESC is defined as

$$\begin{aligned} \text{EESC}(\Gamma, t) = &\sum_{\text{Cl}} \left(n_i f_i(\Gamma) \int_0^\infty \chi_{0,i}(t - t') G(\Gamma, t') \mathrm{d}t' \right) + \\ &\alpha \sum_{\text{Br}} \left(n_i f_i(\Gamma) \int_0^\infty \chi_{0,i}(t - t') G(\Gamma, t') \mathrm{d}t' \right). \end{aligned} \tag{2.19}$$

The transfer to this EESC formulation makes the calculation more appropriately applicable throughout the atmosphere.

In [Engel et al., 2018], the most recent revision of EESC was published. This formulation is primarily considered in the present work. Based on [Ostermöller et al., 2017], they aimed at using a formulation of the fractional release which is independent of the tropospheric trends of the source gases, which is described by integrating the transit time dependent fractional release $f(t)$ weighted by $G(t)$, which is equivalent to the norm of the release time distribution as

$$\bar{f}(\Gamma) = \int_0^\infty G^{\#}(\Gamma, t') \mathrm{d}t'. \tag{2.20}$$

Furthermore, instead of using the age spectrum, the propagation of the inorganic fraction released from the tracer through the stratosphere was considered, thus applying the normalized release time distribution $G_{\text{N}}^{\#}$. This approach determines EESC as follows

$$\begin{aligned} \text{EESC}(\Gamma, t) = &\sum_{\text{Cl}} \left(n_i \bar{f}_i(\Gamma) \int_0^\infty \chi_{0,i}(t - t') G_{\text{N},i}^{\#}(\Gamma, t') \mathrm{d}t' \right) + \\ &\alpha \sum_{\text{Br}} \left(n_i \bar{f}_i(\Gamma) \int_0^\infty \chi_{0,i}(t - t') G_{\text{N},i}^{\#}(\Gamma, t') \mathrm{d}t' \right). \end{aligned} \tag{2.21}$$

In the model application, $G^{\#}$ is implemented, while using $G_{\text{N}}^{\#}$ and mean fractional release $\bar{f}$ is rather redundant as $G_{\text{N}}^{\#} \cdot \bar{f} = G^{\#}$. Therefore, the preferred formulation of Eq. 2.21 in the model case is

$$\begin{aligned}\mathrm{EESC}(\Gamma, t) = \sum_{\mathrm{Cl}} \left(n_i \int_0^\infty \chi_{0,i}(t-t') G_i^{\#}(\Gamma, t') \mathrm{d}t' \right) + \\ \alpha \sum_{\mathrm{Br}} \left(n_i \int_0^\infty \chi_{0,i}(t-t') G_i^{\#}(\Gamma, t') \mathrm{d}t' \right) .\end{aligned} \tag{2.22}$$

Which can be recognized as the formulation for products of tracers as is was introduced in the beginning of this chapter.

Chapter 3
Model Description and Set-ups

3.1 EMAC

In the present study the chemistry climate model EMAC (ECHAM/MESSY Atmospheric Chemistry, [Jöckel et al., 2006]) was employed. Specifically, the second version of the Modular Earth Submodel System (MESSy2) was used [Jöckel et al., 2010]. The core atmospheric model is the European Centre Hamburg general circulation model (ECHAM, [Roeckner et al., 2006]). MESSy provides an infrastructure with generalized interfaces for standardized coupling of earth system model (ESM) components (dynamical cores, physical parameterizations, chemistry packages, diagnostics etc.).

All simulations were run with a spherical truncation of T42 corresponding to a quadratic Gaussian grid of approximately 2.8 x 2.8 degrees with 90 vertical hybrid pressure layers and explicitly resolved middle atmosphere dynamics (T42L90MA). In this setup, the uppermost model layer is centered at around 0.01 hPa and the vertical resolution in the upper troposphere lower stratosphere region (UTLS) is 500-600 m.

In general, the following possible operation modes of EMAC will be relevant in the present work.

- Free running
- Transient and time-slice simulations
- With and without interactive chemistry

Generally, EMAC solves the primitive equations, describing dynamics and all relevant physical processed in the atmosphere. If the model is allowed to simply do this, this is referred to as free running mode. In contrast, for certain investigations the prognostic variables can additionally be relaxed by Newtonian relaxation towards a given data set (nudged mode).

In transient simulations, the boundary conditions greenhouse gas concentrations, emissions, sea surface temperature and sea ice content change continuously following certain scenarios. If trends of atmospheric measures should be investigated, this mode is required. Alternatively, time-slice simulations repeat the boundary conditions of e.g. a single year to produce a time-slice for that year.

If a simulation is run with interactive chemistry, the chemical reactions directly impact radiation and dynamics. If a simulation is run without interactive chemistry, this can be referred to as a dynamics only simulation. In the case of EMAC, this means that only the modules for dynamics, physics and diagnostics are used, e.g. AEROPT, CLOUD, CLOUDOPT, CONVECT, CVTRANS, E5VDIFF, ORBIT, OROGW, PTRAC, RAD, SURFACE, TNUDGE, TROPOP, VAXTRA, depending on the specific requirements on the simulation. For details on these submodels refer to [Jöckel et al., 2005, Jöckel et al., 2010, Jöckel et al., 2016]. In that case, the species relevant for radiation need to be prescribed.

3.2 Model implementation of chemically depleted spectra

In the following chapters arrival time distributions and derived measures of chemically depleted substances will be investigated as described in Sec. 2.3. To do so, tracer pulses are required, in a similar fashion as to diagnose age spectra as explained in Sec. 2.3.1. For this application, the tracer pulses need to be affected by the same loss as the species whose arrival time distribution will be described. The implementation of the pulses has to be such that the loss of the full species is not affected and the computational costs and the amount of data remain reasonable.

3.2.1 Time varying, non-transient transport time distributions

Regarding Age of Air spectra, two approaches are common. One is as described in [Li et al., 2012]. Only one pulse of a tracer is released for every month of the year and left running for ten years. From this data, an age spectrum is derived that cannot represent any temporal variability. The other approach is given in [Ploeger and Birner, 2016] and already explained in Sec. 2.3.1. Tracer pulses are released continuously every other month (or any other desired time interval) and reset after a specified time running. From this data, time evolving age spectra are derived.

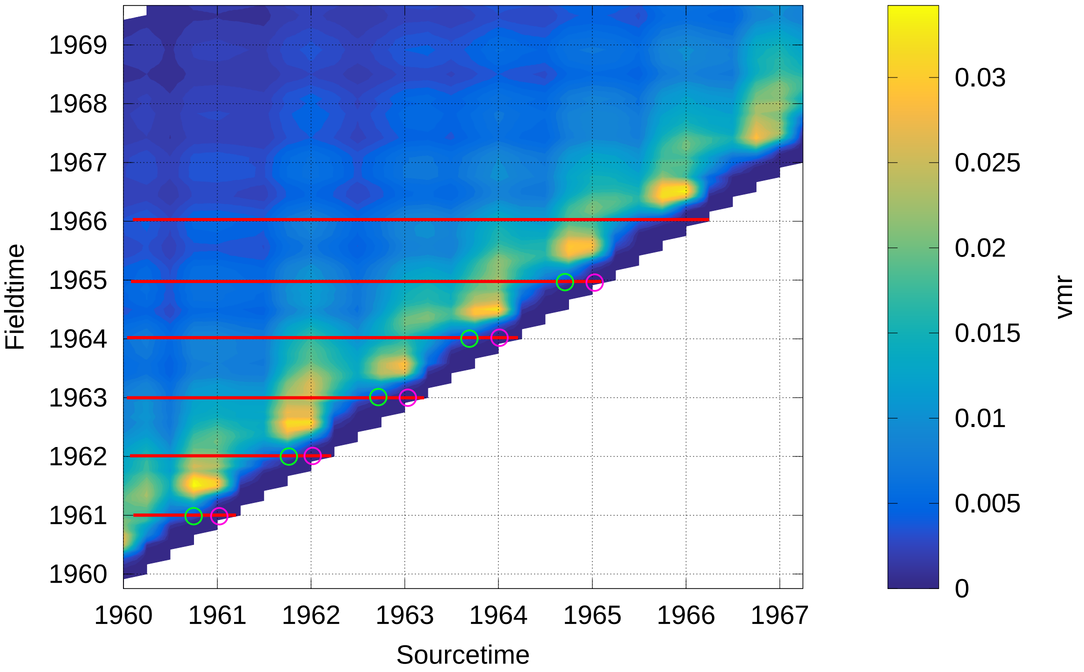

Figure 3.1: Illustration to explain how transport distributions can be derived from the mixing ratios of tracer pulses released at certain source time and evolving with field time. The horizontal red lines indicate resulting age of air spectra.

Conceptually, the latter procedure is illustrated in Fig. 3.1. The tracer pulses evolve with field time along the vertical axis. According to their source time, the pulses are sorted along the horizontal axis. Thus, the different age spectra are obtained from horizontal cuts across the tracer pulses.

However, to investigate nine different chemical species with a monthly resolution and the spectrum extending up to ten years, this approach would require more than one thousand tracer pulses simultaneously, which would result in considerable amounts of data. But still, it is favorable to consider the temporal variability of the transport time distributions, as the inter-annual variability in particular at shorter transit times is quite noticeable. Consequently, only one pulse as in [Li et al., 2012] does not represent this variability. Neither is the desired solution to reduce the resolution along the transit time axis or the extent of the spectra.

The solution picked here could be named a time-varying [Li et al., 2012] approach. This means, one set of pulses is run for a certain amount of years and then reset and rerun. As the transport time distributions are investigated in time-slice simulations, meaningful climatological mean transport time distributions along the source time axis can be obtained using this realization. To make the according averaging of the tracer pulses more understandable, colored circles were added to Fig. 3.1. To e.g. calculate the first value of the January transport distribution in monthly resolution, one averages the values in January of all tracers released in January (pink circles). The second value of the January distribution is obtained by averaging the January values of all pulses released in December (green circles). This realization even allows to consider more pulses in the beginning of the arrival time distributions. The beginning of the distributions is subject to more variability and therefore better represented by more pulses. Whereas the tail of the transport time distribution represents integrated transport of several years and hence less variable and requires less pulses to be well represented.

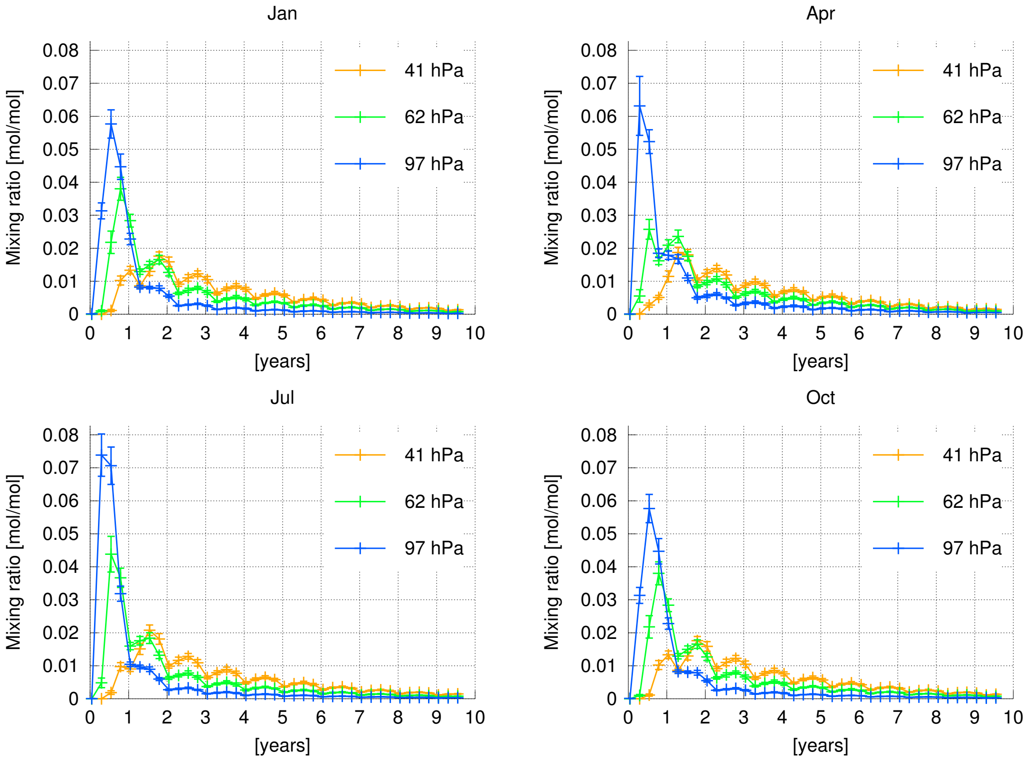

Figure 3.2: Shown are mean age spectra calculated from the available ten spectra in the respective months (title) at the respective pressure levels (legend) at 60° N. The error is calculated as the 95% standard deviation of the mean calculated using all possible combinations of four spectra out of ten.

Following the previous explanation, in the simulations considered in the following chapters, four sets of pulses were implemented, two of which were running for seven years and two were running for ten years (See also Table 3.1). Consequently, the question arises, whether four tracer pulses represent the temporal variability well enough. To give an answer, the sclicePul simulation was considered (Details Sec. 3.3.2). That is a time-slice, dynamics only simulation using year 2000 conditions. Most interestingly, it contains ten years of transient age spectra extending to almost ten years. Out of the ten sets of pulses available, average spectra are calculated using all possible combinations of four pulses out of them. From those average values standard deviations are calculated (95% confidence interval). The results are given for a selection of altitudes at 60° N in Fig. 3.2. The results are given in mixing ratio, i.e. non-normalized. The boundary condition for the pulses was set to 1 mol mol^{-1}. This example shows a variability of up to 0.008 mol mol^{-1} for values ranging from 0.04 mol mol^{-1} to 0.075 mol mol^{-1} for the first year of the arrival time distribution. At larger transit times, the variability in the arrival time distribution becomes unnoticeable.

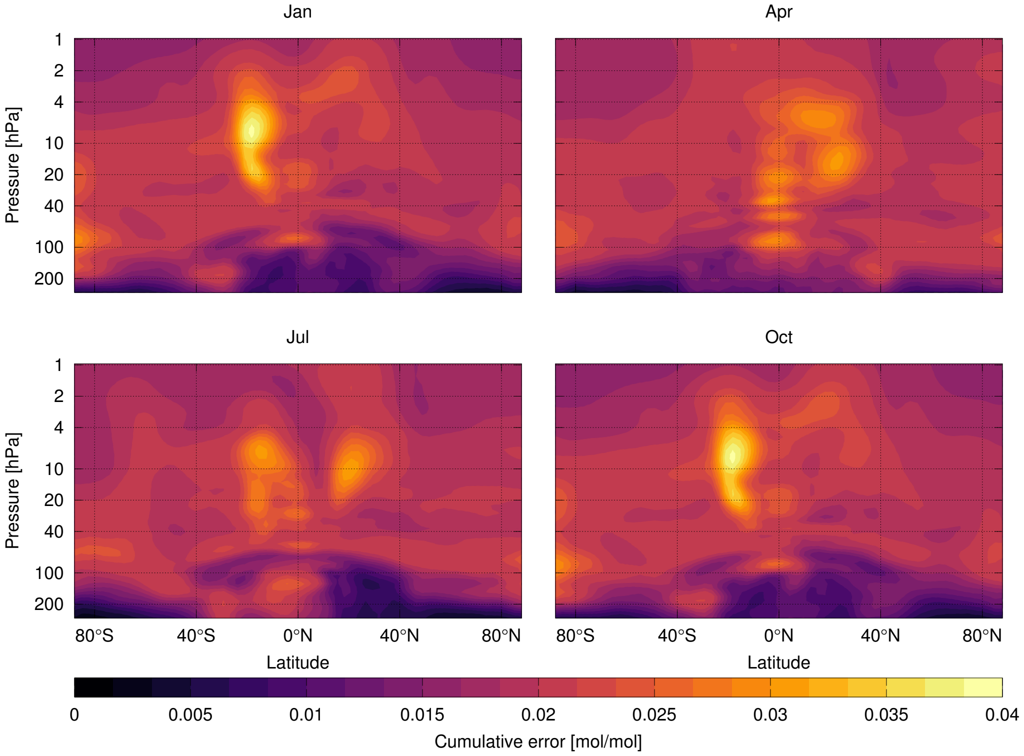

Figure 3.3: Based on Fig. 3.2, cumulative standard deviation summed along the spectrum.

Further, Fig. 3.3 shows the cumulative standard deviation for the full spectra. Most regions show similar variability as already anticipated from Fig. 3.2. Exceptions to this are the regions around the tropical pipe which are noticeable as regions of stronger variation.

3.2.2 Cheap, easy loss for Pulses

MESSy provides an abundance of modular infrastructure which can be used to implement diagnostics, such as tracer pulses that are chemically depleted in the same manner as the full species they represent. First of all, the boundary condition mixing ratio of the pulses can be prescribed via the submodule TNUDGE, as for other pulse applications. The accumulated loss of the full species can be made available from the solver for chemical kinetics MECCA via a diagnostic entry in diagtrac. The relative loss of a tracer is the quotient of the tendencies of the loss and the mixing ratio χ of the tracer:

$$\text{Relative Loss} = \frac{1}{\chi}\frac{\mathrm{d}}{\mathrm{d}t}\text{Loss}_\chi = \frac{\text{Loss}_\chi(\boldsymbol{r}, t+\Delta t) - \text{Loss}_\chi(\boldsymbol{r}, t+\Delta t)}{\chi(\boldsymbol{r}, t)}. \tag{3.1}$$

The MESSy submodule SCALC can do simple calculations online. However, the option to divide fields had to be implemented first. A lower limit of 1e-24 for the denominator was prescribed below which the result would be set to zero to avoid errors of dividing by zero or numerically non meaningful results.

Having the relative loss made available, an differential equation of the type

$$\frac{\mathrm{d}x}{\mathrm{d}t} = -x \cdot A \tag{3.2}$$

needs to be applied to the tracer pulse using the relative loss as a decay constant A. The sub module TREXP can be used to just do this, while being considerate of units.

This procedure is appealing, as it is simple, mostly uses available model infrastructure, is not too computationally expensive and does not disturb the chemical loss rates of the full species. Still, the procedure is first tested in a short two month model run. The respective regular, full tracer and a tracer with the same boundary conditions and prescribed calculated loss are compared. Fig. 3.4 shows the results for CF_2Cl_2.

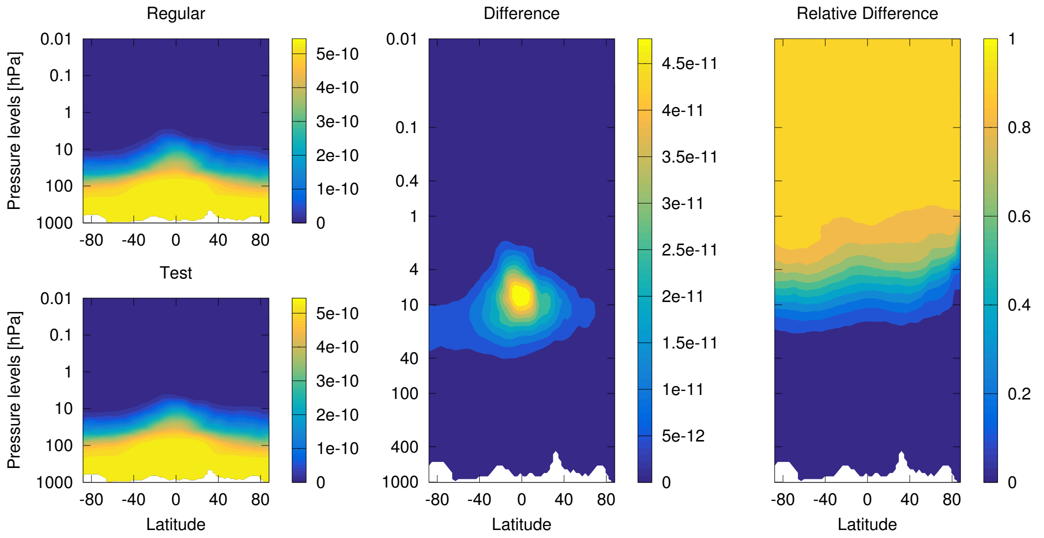

Figure 3.4: Comparison of mixing ratios of a tracer which is subject to regular chemical loss and a tracer that is subject to calculated prescribed loss (panel "Regular" and "Test"). Shown here is CF_2Cl_2 after 55 days of simulation. The mixing ratio is given in $\mathrm{mol\,mol^{-1}}$. The other panels show the difference in mixing ratio and the relative difference in mixing ratio as fraction.

For all tested chemical species, the absolute difference is about one order of magnitude smaller than the mixing ratios themselves in the region of strongest depletion where the largest absolute deviation is found. The relative differences in regions where considerable amounts of the tracer are present is very low. In regions where little of the specific full tracer is present, the deviations become noticeable. The deviations are anticipated, as the limit in the calculation of the relative loss leads to neglecting the loss in those regions of little mixing ratios. In particular, this becomes noticeable for tracers with shorter lifetimes. Therefore, it seems reasonable to implement the chemically depleted tracer pulses as described and mark regions with low mixing ratios of the full tracer in the following chapters where necessary.

3.3 Set-ups

3.3.1 RC1-base-07

The RC1-base-07 simulation is a simulation, which was conducted as part of the ESCiMo project. It is a transient full chemistry hindcast simulation stretching from 1950 to 2011 using EMACv2.50.4. It follows the REF-C1 scenario as defined by the CCMI (Chemistry-Climate Model Initiative, [Eyring et al., 2013]). Details on the setup and an evaluation of this chemistry-climate simulation can be found in [Jöckel et al., 2016] and [Morgenstern et al., 2017]. The data is relevant to analyze trends from 1950 to 2010 in AoA derived from SF_6 in a setup close to reality.

3.3.2 slicePul

The second simulation, referred to as slicePul is a dynamics only, time-slice experiment employing EMAC version 2.53.0. Its main focus was implementing and testing transient age spectra in EMAC as described in Sec. 2.3.1. Therefore all other aspects were kept as simple as possible. Year 2000 climatological mean SSTs and SICs have been prescribed following the global data set HadISST provided by the UK Met Office Hadley Centre (available via http://www.metoffice.gov.uk/hadobs/hadisst/, [Rayner et al., 2003]). The GHG mixing ratios for the radiation calculations were prescribed with the EMAC E5 setup default values.

Periodical pulses of an inert tracer were released at the surface between 20° S and 20° N. This means that every three months, the lower boundary conditions of that tracer are set to 1 for one month at the tropical surface. After 9.5 years, the tracers are set to zero and started again to avoid large computational expenses. This operation is performed with the specifically designed MESSy submodule TPULSE. This EMAC setup contributed to [Hauck et al., 2019]. The pulses allow to derive time evolving age spectra in EMAC as described for CLaMS (Chemical Lagrangian Model of the Stratosphere) in [Ploeger and Birner, 2016]. In the slicePul simulation, ten years of age spectra are available.

3.3.3 tranPul

The third simulation, termed tranPul, is an EMACv2.53.0 run which is designed to resemble the RC1-base-07 simulation as closely as possible, however for cost efficiency reasons, without using interactive chemistry. In that simulation, the monthly mean fields of the main greenhouse gases CO_2, CH_4, N_2O and O_3 were transiently prescribed from the RC1-base-07 simulation as zonal mean, monthly mean fields. As both simulations do not include a coupled ocean, SSTs and SICs have been prescribed following the global data set HadISST. Although in the L90 setup of EMAC, the QBO is internally generated [Giorgetta et al., 2002], the zonal winds near the equator were slightly nudged in the simulations to get the correct phasing of the observed QBO. Moreover, atmospheric aerosol (including volcanic aerosol) has been prescribed to take into account the interactions with radiation.

3.3.4 chemPul-2000 and chemPul-2050

The last two simulations, chemPul-2000 and chemPul-2050 are EMACv2.54.0 time-slice simulations with full chemistry. They follow the conditions of the year 2000 and of a projection for 2050, respectively. The year 2050 is described according to the RCP 6.0 scenario [Eyring et al., 2013]. The year 2000 was picked as an example of "present day conditions" and high concentrations in ODS. 2050 was selected as a year that represents "future conditions", already has noticeable climate change due to increased GHG concentrations relative to 2000, but still has ODS left. The decrease of ODS and ozone recovery impact the climate in addition to the increasing GHG. Thus, the selection of scenarios allows to investigate the effects of changing transport due to changing climate by looking at ODS (including N_2O). The respective scenarios follow the respective climatologies of the ESCiMo simulations RC1-base-07 and RC2-base-04[1], as described in [Jöckel et al., 2016]. As described in further detail Sec. 3.2.1, time varying, non-transient arrival time distributions of certain ODS and N_2O are implemented in both simulations.

An overview of the considered number of years of pulses is given in Table 3.1. The start and end years in the table are symbolic, as the simulations are time-slices of 2000 and 2050 respectively. The nominal start of both simulations is 1950.

Table 3.1: Years of pulses run in chemPul simulations.

Start and end year	Years run
1955-64	10
1965-71	7
1972-81	10
1982-88	7

Table 3.2 provides a full list of the considered species for the arrival time distributions, their estimated stratospheric lifetimes and the depletion processes they are subject to. The combination of even and odd years was picked to make sure, that the QBO phases are considered without a bias towards one phase. Even though the resolution is high enough that the model could develop a QBO, the QBO was nudged towards the same transient QBO to avoid artifacts due to different QBO phases when comparing both simulations. If the simulations were left to develop their own QBO, they might even become stuck in one phase for some time. Similarly, the solar cycle was nudged towards the same transient solar cycle to avoid artifacts due to offsets in the cycles.

---

[1] Free-running future projection

Table 3.2: Species considered in the chemPul simulations. Lifetimes partly adapted from [Engel et al., 2018]

Species	Stratospheric lifetime [years]	Reaction
N_2O	125.2[b]	O^1D, OH, hν
CF_2Cl_2 (CFC-12)	102[a]	O^1D, hν
CH_3Cl	63.7[a]	O^1D, OH, hν
CF_3Br (Halon-1301)	70.8[b]	hν
$CFCl_3$ (CFC-11)	55.7[a]	O^1D, hν
CCl_4	48.4[a]	O^1D, hν
CH_3Br	40.2[a]	O^1D, hν
CF_2ClBr (Halon-1211)	39.5[a]	hν
CH_3CCl_3[c]	48.8[a]	O^1D, OH, hν

[a] Stratospheric lifetime from the 2-D model used by [Plumb et al., 1999]. [b] Stratospheric lifetime taken from modeling work for SPARC lifetime assessment [Ko et al., 2013]. [c] Mixing ratio is zero for the 2050 scenario.

CHAPTER 4
Mean Age of Air trend evaluation

The main objective of this chapter is the discrepancy between modeled and observed mean AoA trends in the NH mid-latitudes mid-stratosphere. Thus using the model for method evaluation, two methods to infer mean AoA from non-liner tracers will be evaluated. This means that the influence on the mean AoA trend of the assumed age spectrum for the description of the transport of inert tracers will be investigated in detail.

As stated in the beginning of this work, this chapter has already been published in the following preprint and is reprinted here. The paper is already accepted.

- Fritsch, F., Garny, H., Engel, A., Bönisch, H., and Eichinger, R. (2019). **Sensitivity of age of air trends on the derivation method for non-linear increasing tracers.** Atmospheric Chemistry and Physics Discussions, [Fritsch et al., 2019]

Further, results of the SlicePul simulation also used in this chapter already contributed to the results published in

- Hauck, M., Fritsch, F., Garny, H., and Engel, A. (2019). **Deriving stratospheric age of air spectra using an idealized set of chemically active trace gases.** Atmospheric Chemistry and Physics, [Hauck et al., 2019]

4.1 Age spectra

It is straightforward to derive mean AoA from linearly increasing tracers in models, as described in Sec. 2.3.1. An example for mean AoA in EMAC was already given in Fig. 2.5, which shows mean AoA derived from the idealized linear increasing tracer for July 2001-2010 from the RC1-base-07 simulation.

Since the derivation of mean AoA from measurements requires an assumption about the AoA spectrum, spectra were derived for EMAC in the transient, dynamics only tranPul simulation. The implementation was such that tracer pulses were released every three months and kept running for 9.5 years, which is due to the technical realization. Fig. 4.1 shows the seasonal evolution of the modeled spectra at 59° N and 106 hPa. This is close to 400 K and 60° N potential temperature, as in Figure 5 in the study by [Ploeger and Birner, 2016]. The MAM, JJA and SON spectra show a similar propagation to [Ploeger and Birner, 2016]. DJF rather shows one major peak instead of two as in [Ploeger and Birner, 2016]. The coarse resolution of the spectra along the transit time axis of 3 months could be the reason for this, since the actual maxima of the age spectrum may fall in between a three month period such that they are not visible. For comparison, the spectrum calculated from the Hall and Plumb parameterization (see Eq. 2.10) is shown, using the values from the annual mean spectrum, that is a mean age value of 1.6 years (vertical line) and a ratio of moments of 1.8 years. For the chosen parameters, the modal age of the theoretical Hall and Plumb spectrum is lower than for the

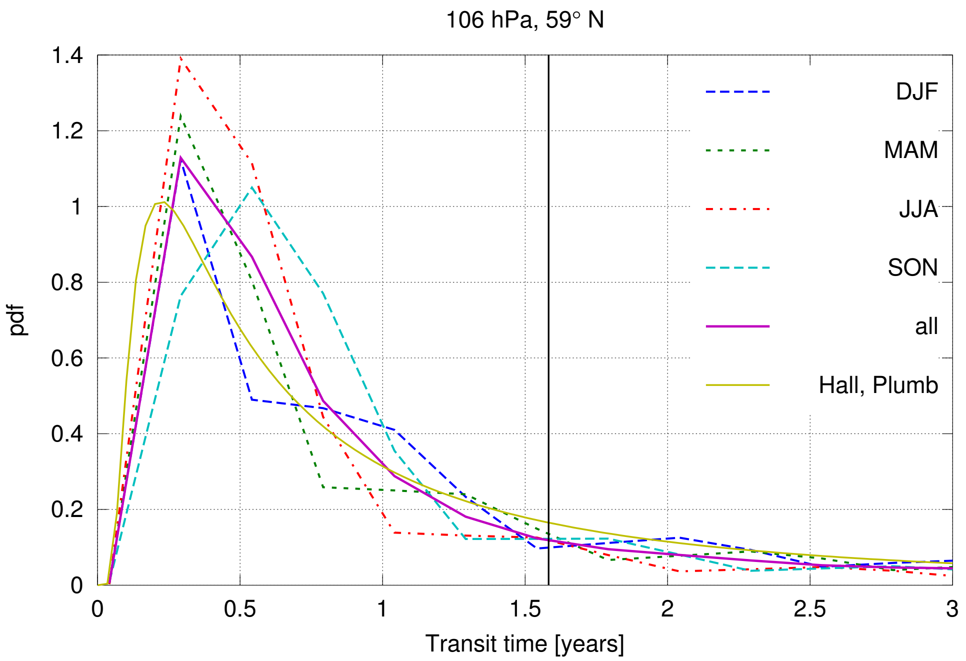

Figure 4.1: Age spectra at 59° N and 106 hPa from the tranPul simulation. The dashed lines are the seasonal mean spectra. The pink solid line is the annual mean age spectrum. The solid yellow line is the spectrum calculated from the Hall and Plumb parameterization using the values from the integration of the annual mean spectrum, that is a mean age value of 1.6 years (vertical line) and a ratio of moments of 1.8 years (Eq. 2.8 and 2.9)

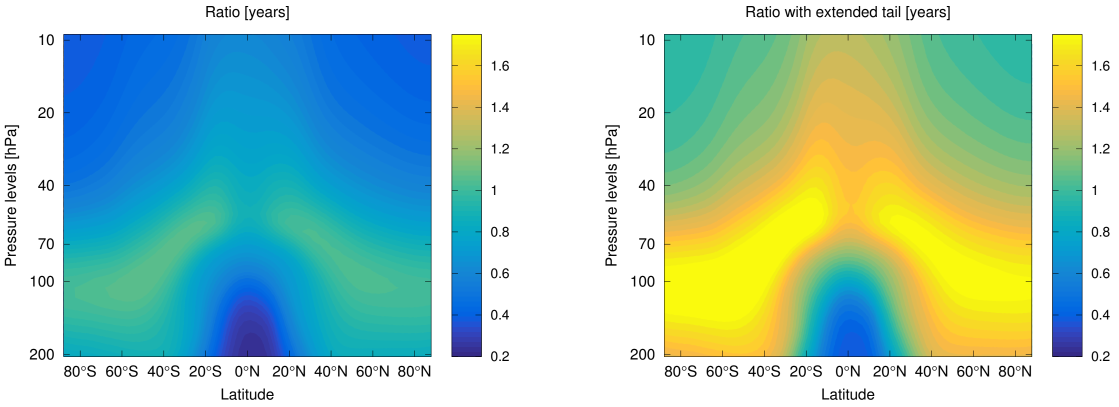

Figure 4.2: Mean ratio Δ^2/Γ derived from age spectra in the tranPul simulation. On the left for the regular 9.5 year long spectra, on the right with exponentially extended tail as in [Ploeger and Birner, 2016].

actual spectrum and the tail is broader. However, how well the modal age compares depends strongly on the applied ratio of moments.

The ratio of moments calculated directly from the spectra, i.e. using the length of the spectra of 9.5 years are small, as shown in Fig. 4.2 (left). To provide context, values of 0.7 to 1.25 years are proposed for age calculations in [Hall and Plumb, 1994]. Following [Ploeger and Birner, 2016], the spectra were extended to 50 years using an exponential fit on the second half of the spectrum, i.e. transit times above 5 years. The ratio of moments in that case (Fig. 4.2

right) shift to larger values of up to 1.7 years in the annual mean covering the full simulation. This is consistent with the dynamics only SlicePul simulation, that was shown in [Hauck et al., 2019], that also showed ratio of moments larger than the upper limit of 1.25 years derived from the one dimensional diffusion analog by [Hall and Plumb, 1994]. Though, it should be considered that [Hall and Plumb, 1994] assumed 10 years of age spectrum in their approximation, while the other approaches also considered longer transit times, which tends to give larger ratio of moments. More details on the inter-annual variability of the ratio of moments will be discussed in Sec. 4.1.1. Also in that section, the ratio of moments from the modeled spectra will be used in the age calculations. Both the extended and non-extended spectra show a noticeable spatial dependency. For example in the extratropical LS the ratio of moments is largest due to the strong mixing influence that leads to broad age spectra.

4.1.1 Sensitivity of mean AoA and AoA trends on parameter choice in the fit method

As described in Sec. 2.3.1, mean AoA and its trend were calculated from SF_6 and an ideal linear tracer for the RC1-base-07 simulation for a range of parameters, namely the ratio of moments and the fraction of input, and reference locations for the fit method (explained in Sec. 2.3.1). Since a self-consistent model world is considered and an idealized SF_6 without sinks is implemented, perfect agreement between the trends derived from the two tracers is expected.

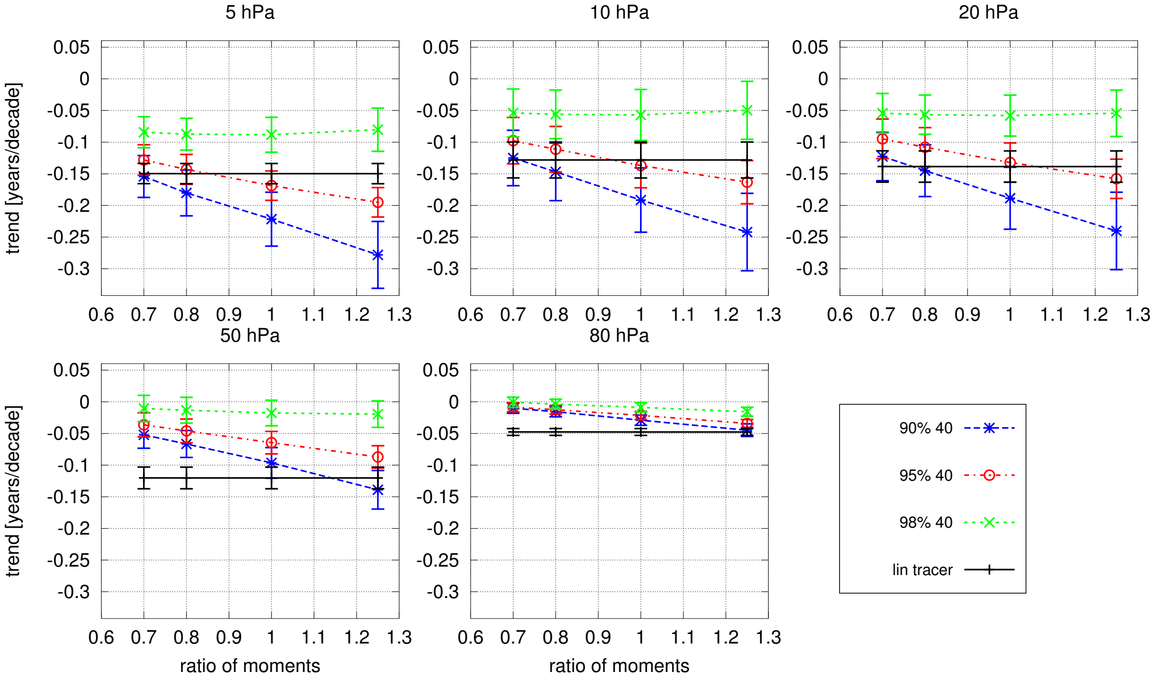

Figure 4.3: Overview of the trend in mean AoA derived from SF_6 (dotted lines) and a linear tracer (solid line) for different ratio of moments (x-Axis) and fractions of input (colors) at 40° N. The panels show different pressure levels. The trend calculation considered the time series from 1975 to 2011. The error bars show 1σ which is the 68% confidence levels.

The fraction of input was varied between 90%, 95% and 98% and the ratio of moments between 0.7, 0.8, 1.0 and 1.25 years. This covers the range for the ratio of moments proposed in [Hall and Plumb, 1994]. Also, the pair of values 98% and 0.7 years, as applied to the measurements in [Engel et al., 2009] and [Engel et al., 2017], is considered in this selection.

The resulting trends for 40° N and a selection of pressure levels are shown in Fig. 4.3. Other latitudes show similar behavior and are therefore not shown. The trend calculation was performed on deseasonalized values and considered autocorrelation [Thompson et al., 2015]. The trend of the linear tracer is included in the plots for each parameter choice to make comparison easier, though it does not have any sensitivity to them. Overall, the trends derived from SF_6 are more negative the larger the ratio of moments and closer to zero the larger the fraction of input that is considered. Furthermore, the sensitivity of the trends to the ratio of moments increases when using a lower fraction of input. Intuitively, one might think that the results would be better the more of the reference input is considered (larger fraction of input). However, the fit performed on the reference time series is not weighted by, e.g. the spectrum. Therefore taking very long fit intervals takes into account more old air, which only has a small contribution to the actual mean AoA.

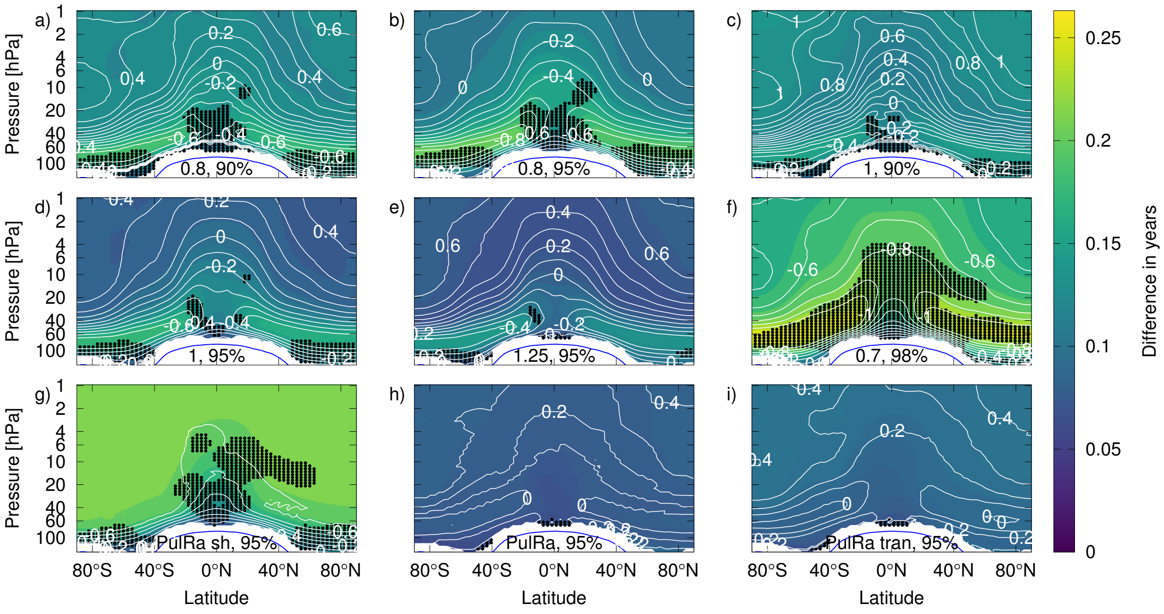

Figure 4.4: Mean absolute deviation of mean AoA calculated from SF_6 from AoA derived from an ideal tracer for different ratio of moments and fraction of input (colors). The overlaid white contours are the difference in trends in 10^{-1} years decade^{-1}. At the bottom of each panel, the fraction of input and ratio of moments considered in the derivation are stated. PulRa denotes the ratio of moments derived from the tranPul simulation annual mean extended age spectra, PulRa sh is from the 9.5 year spectra. PulRa trans uses the transient extended spectra from that simulation. White areas indicate where the derivation is not applicable. Black stippling show insignificance of the SF_6 trend from zero on the 95% confidence level. The trend calculation considered the time series from 1975 to 2011. The tropopause and the range 30 K above are excluded, as the AoA calculation is not defined in this region due to the different entry regions into the stratosphere that have to be considered.

Fig. 4.3 also shows that depending on the pressure level, different selections of ratio of moment and reference input lead to agreement between the trends of the idealized and the

SF_6 tracer. The influence of transport and mixing on the age distribution can explain that the best choice for the ratio of moments varies by location.

To build onto what was already seen from Fig. 4.3, Fig. 4.4 shows the mean absolute deviation of mean AoA derived from SF_6 and the linear tracer in the latitude-height domain for different selections of parameters in the derivation (colors). The white contours show the difference in trends in 10^{-1} years decade^{-1}. Further, in Fig. 4.4 a spatial distribution of ratio of moments is also considered. Even though age spectra are not available for the RC1-base-07 simulation, those from the tranPul simulation are a suitable first estimate for EMAC as a model. The ratio of moments for the 9.5 year long spectra (PulRa sh) and the extended spectra (PulRa) were considered (see Fig. 4.2).

It is evident from Fig. 4.4 that using a fixed ratio of moments for the whole latitude-height domain always leads to deviations in mean AoA and its trends in some region (Panels a-f). Using the ratio of moments derived from the 9.5 year spectra reduces the spatial pattern of deviations (panel g). However, an offset to the actual mean AoA values and trends remains as overall the ratios of moments are underestimated when neglecting the tail. In the range of the balloon borne observations (5 hPa-30 hPa and 32° N-51° N) this means an average deviation of 4% in AoA values and 56% in AoA trend. The ratio of moments derived from the extended age spectra leads to the best agreement across the widest spatial range for both mean AoA and its trend (Panel h). Both annual mean ratio of moments and transient ratio of moments, were used, though the transient ratio of moments do not show strong further improvement over the annual means (Panel i). Using PulRa and 95% fraction of input provides 1% average deviation in age values and 12% deviation in trends in the region of the observations. The spatial dependency of an appropriate ratio of moments might play a role for the measurement application considering that the measurements in [Engel et al., 2009] were analyzed between 5 hPa-30 hPa and 32° N-51° N.

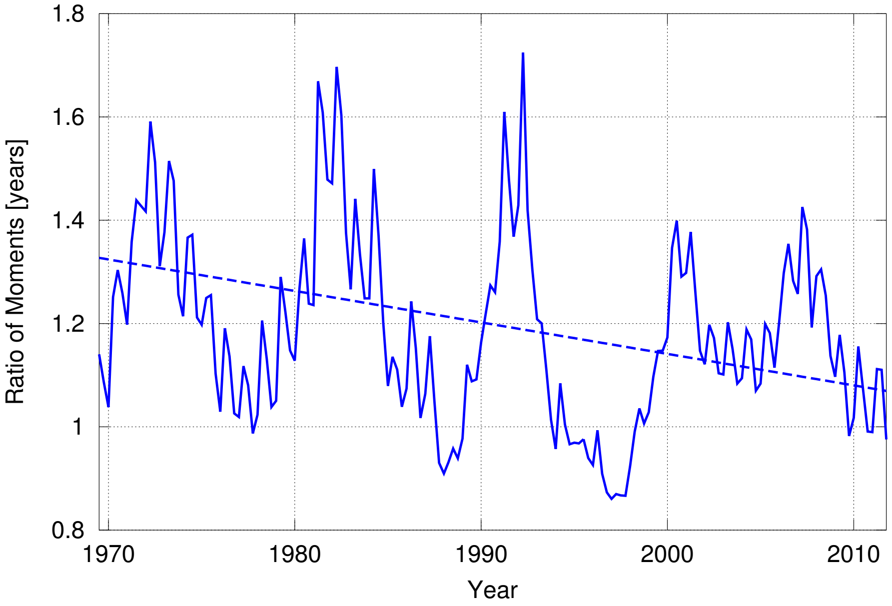

Figure 4.5: Ratio of moments derived from extended age spectra from the tranPul simulation at 20 hPa and 40° N

Fig. 4.5 shows an example of the transient ratio of moments at 20 hPa and 40° N from the tranPul simulation. Its trend is drawn, even though it is not significant as the trend is small compared to the variability. The trend of the ratio of moments is negative at all locations, but mostly not significant. The cycles visible in the ratio of moments presumably origin from the prescribed QBO and the solar cycle inherent in the prescribed ozone, assumed by their period length. It is beyond the scope of the current study to examine the large variability in the ratio of moments, but in particular the strong variation with periodicity of about 10 years calls for future investigations. Considering for example [Labitzke, 2007], it is anticipated that the solar cycle influences the BDC and thereby the shape of the age spectrum. The AoA calculation typically considers about 10 years of reference input. That equates roughly to one cycle in strong variation in ratio of moments which are integrated. That might explain that most improvement in the AoA derivation comes from applying an appropriate spatial distribution of ratio of moments and not from using a transient one.

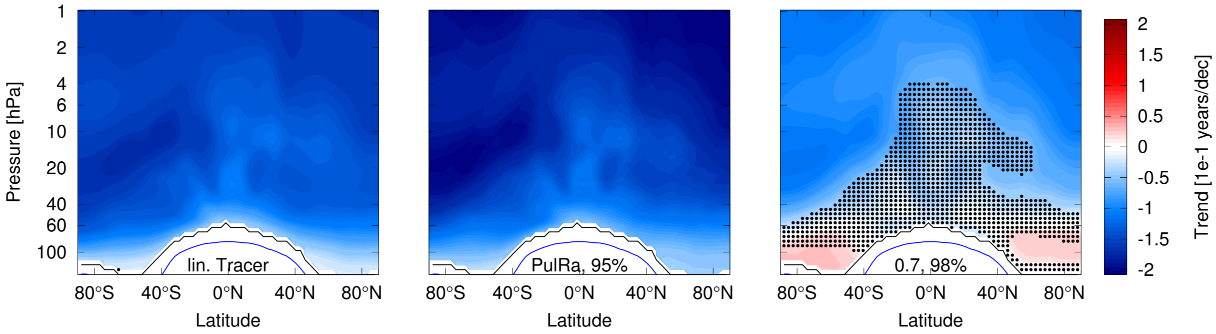

Figure 4.6: Based on the RC1-base-07 run, trends of mean AoA from 1975 to 2011 derived from a linear tracer (left panel) and from SF_6 for the ratio of moments from the extended pulse spectra and 95% fraction of input (middle) and 0.7 years ratio of moments and 98% fraction of input (right). White areas are the areas that cannot be analyzed for a trend and black stippling shows insignificance of the trend from zero on the 95% confidence level.

As shown in Fig. 4.4, Panel f, the combination of $F = 98\%$ and $^{\Delta^2}/_{\Gamma} = 0.7$ years applied to derive AoA from observations leads to systematic offsets in both mean AoA and the AoA trends between the linear and SF_6 tracer in EMAC. In Fig. 4.6 the mean AoA trends for the RC1-base-07 run are shown, which further illustrates the offset in trends. The AoA trends derived from SF_6 with this parameter choice are slightly negative or even positive and insignificant across a wide domain. Calculating the average AoA trend for 98% and 0.7 years across the spatial range of the observations, i.e. 5 hPa-30 hPa and 32° N-51° N, yields

- -0.13 years decade^{-1} $\pm$ 0.025 years decade^{-1} for the linear tracer
- -0.057 years decade^{-1} $\pm$ 0.033 years decade^{-1} for the SF_6 tracer.

Hence, averaged across that range, the mean AoA trend derived using those parameters stretches to positive on the 2σ range (95% confidence). Expressed relatively, these represent average deviations of 4% in AoA values and 58% in AoA trend.

Since the reference location for the AoA calculation can also be varied in model calculations, the effect on the resulting AoA and its trends were checked. However, the different reference locations that have been tested do not show a strong influence on the resulting mean AoA or its trends. For example, an average of the concentration in the area between 20° S and

20° N on the ground and the same range at 100 hPa were used. In that case, the differences in mean AoA are less than half a year and represent the offset time that the air traveled between the different reference locations (not shown). The differences in the trends are below 0.01 years decade^{-1} for the RC1-base-07 run. Both statements refer to the results that were obtained for different selections of fraction of input and ratio of moments, i.e. also considering selections that do not perform well overall. However, the reference location is important for quite specific tracer initialization on the ground, as for example if the linear AoA tracer is initialized from the poles. In such cases a reference location closer to the tropopause should be used to avoid artifacts of this tracer initialization in the AoA calculation. Since this is not the case for any of the simulations included in this work, the ground is used as reference in all calculations shown here as it is more applicable to measurements.

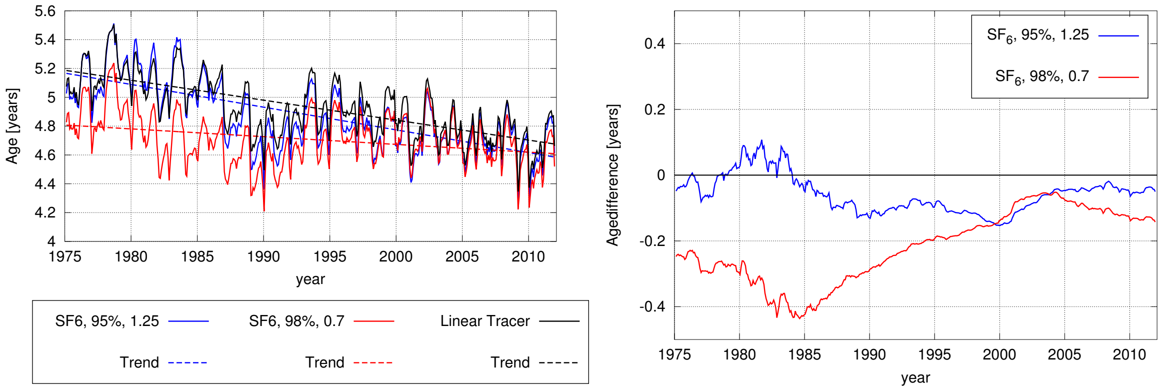

Figure 4.7: On the left mean AoA and its trend derived from SF$_6$ for two sets of parameters (red and blue) and from the linear tracer (black) at 20 hPa and 40° N from 1975 to 2011 from the RC1-base-07 Simulation. On the right accordingly mean AoA from the SF$_6$ tracer minus mean AoA from the linear tracer.

It is found that the sensitivity of the AoA trends derived from SF$_6$ to the parameter choice arises predominantly from deviations in mean AoA in earlier years (1970s and 80s). As an example for this, the left of Fig. 4.7 shows the mean AoA time series and the derived trend at 20 hPa and 40° N for the combinations 98% and 0.7 years (red) and 95% and 1.25 years (blue) for the RC1-base-07 run. The linear tracer is given in black. 95% and 1.25 years represents a combination with relatively good agreement with the linear tracer in AoA whereas 98% and 0.7 years shows a strong deviation. For the mean AoA values at this location the length of the fit to the reference time series is around 11 years. The right panel of Fig. 4.7 shows the differences of the SF$_6$ derived mean AoA and the linear tracer derived mean AoA.

Considering Eq. 2.13, one explanation for the deviations might be that at the beginning of the reference time series the specific fit coefficients c and b of the second order polynomial are very sensitive to the fit interval length. Therefore Fig. 4.8 shows the coefficients dependent on the start date of the fit and the number of years fitted back. The parameters vary slightly stronger for fits early in the time series. As can be seen from Fig. 4.8 and already from the SF$_6$ time series in Fig. 2.2, the first part of the SF$_6$ time series is rather linear. In the eighties the second order contribution is strongest. Afterwards, the slope is rather linear again. Still, the times which show more variation in the coefficients with changing fit interval length do not clearly correspond to the times that the mean AoA derived from SF$_6$ deviates more from AoA

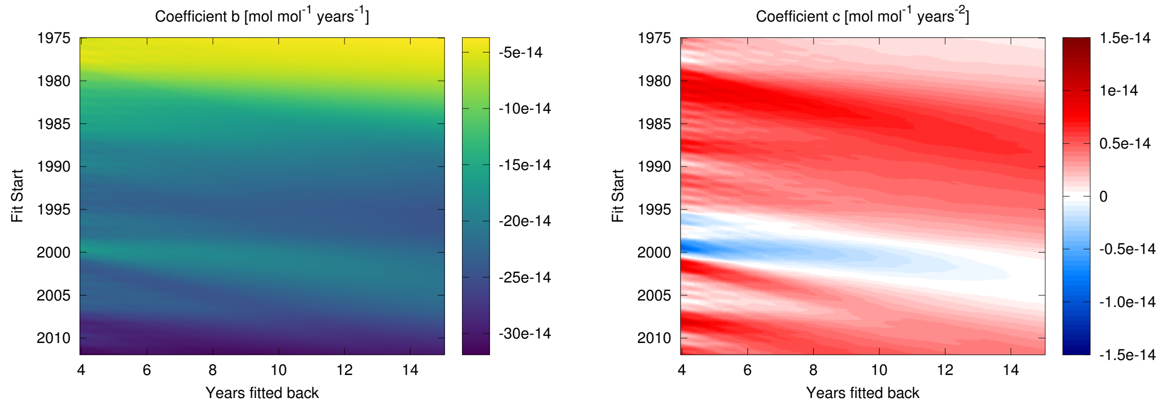

Figure 4.8: Coefficients b and c of the second order polynomial fit to the SF_6 reference time series dependent on the chosen length of fit interval.

derived from the linear tracer.

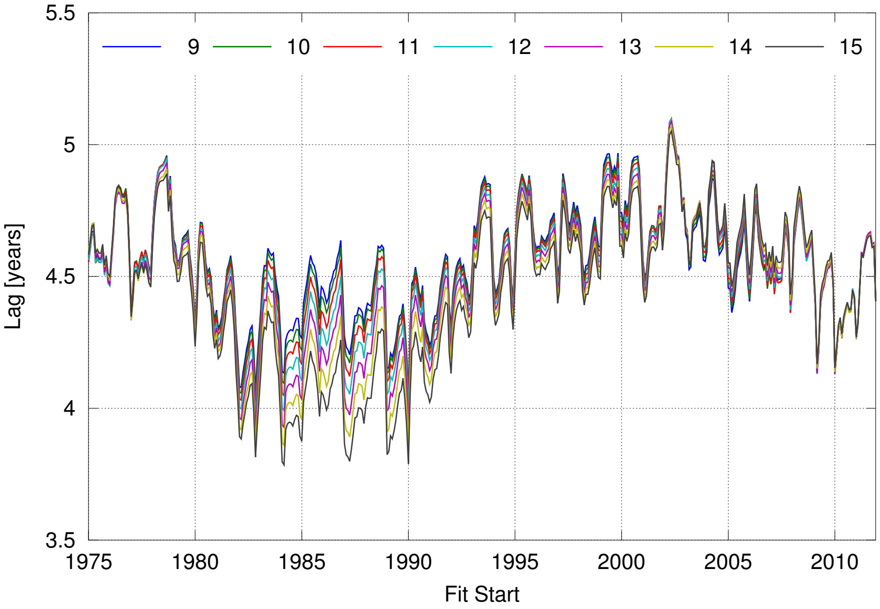

Figure 4.9: Lag time τ for fit interval length 9 to 15 years calculated for the SF_6 time series at 20 hPa and 40° N

Another explanation for the variation in mean AoA might be the sensitivity of the lag time τ to the fit interval length. To be consistent with [Engel et al., 2009] and [Engel et al., 2017], the lag time is determined by approximating the reference time series as a second order polynomial function of the concentration. Thus depending on the number of years considered, the obtained lag time might vary. This is counterintuitive to what one would expect if the lag time was directly looked up from the concentrations. Fig. 4.9 shows the lag times found for the SF_6 time series for fit interval lengths from 9 to 15 years at the same location as the example in Fig. 4.7. From roughly 1983 to 1990, τ depends stronger on the length of the fit interval and varies up to 12% for the shown range of fit intervals.

As described when discussing the polynomial coefficients, the SF_6 reference time series slightly bends in the 1980s which makes the lag time calculation around the late 1980s more sensitive to the fit interval length. The specific years of stronger variation in lag time shift slightly for different locations, dependent on the transport times to that location. As seen from Fig. 4.7 (right), 1983 to 1990 is also the time of strongest deviation for the non-suitable parameter selection in Fig. 4.7. The variation in lag time contributes to the variation in mean age in the beginning of the time series dependent on the selection of parameters in the derivation.

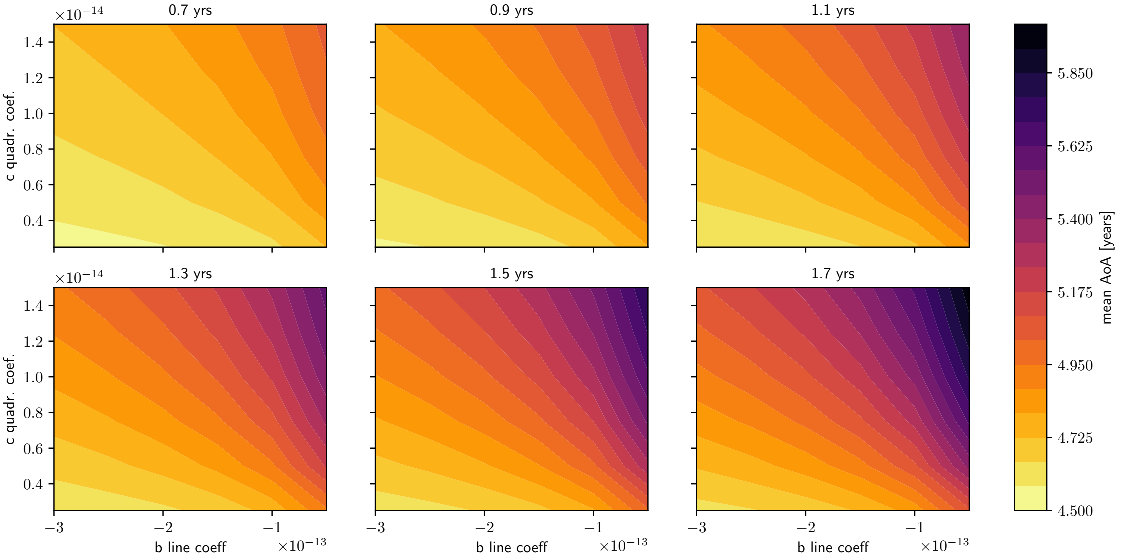

Figure 4.10: Mean AoA Γ for the range of magnitude of the coefficients a and b based on Eq.2.13 using the fixed $\tau = 4.5$ years. The different panels show the respective ratio of moments (Headings).

Now that the range for the polynomial coefficients b and c from the fit to the SF_6 time series is specifically known from Fig 4.8, the sensitivity to Γ for the different b and c can additionally be considered. Based on Eq.2.13, for a fixed lagtime τ, the mean AoA Γ can be calculated for the range of b, c and different ratio of moments. The results are shown in Fig. 4.10. Here, τ was chosen to be 4.5 years which is a reasonable value to apply considering the values for τ in Fig.4.9.

It can be seen, that for b close to zero, Γ becomes more sensitive to the selection of the ratio of moments, as this range shows differences of up to one year in mean AoA, for the selected range of ratio of moments from 0.7 to 1.7 years. Most sensitivity of Γ to the ratio of moment is given when in addition c is on the larger end. If the coefficients b and c in Fig. 4.8 are considered, around the year 1980, b tends to be closer to zero and c tends to be on the larger end. This means that around 1980, the sensitivity of mean AoA to the coefficients is very pronounced. Further, the sensitivity is the way around, that smaller ratio of moments give smaller mean AoA values. Smaller mean AoA values in the beginning of the time series lead to a less negative AoA trend.

To conclude the considerations why the AoA trend is sensitive to the parameter selection, it can be said, that due the shape of the SF_6 boundary condition the beginning of the AoA time series is particularly sensitive to the parameter selection. The bend in boundary condition around the year 1980 leads to sensitivity of the lag-time τ. Further, the rather flat slope in the beginning of the SF_6 time series implies more sensitivity of mean AoA to the parameter selection then. Therefore, the results about the sensitivity of mean AoA trends to the parameter selection are not dependent on EMAC as a model or the applied model resolution.

The latter analyses were done for both SF_6 time series, the one prescribed in the simulation and the one used for calculations from observations. Only the results obtained from the SF_6 time series prescribed in the model are shown here as the results were similar.

4.2 AoA calculations via the Convolution Method

As described in Sec. 2.3.1, applying the convolution method weights the reference input according to the strength of its influence at a certain observation location. This avoids the influence of an assumption of the fraction of input, so one would expect to see more reliable agreement between AoA and its trends than when applying the fit method. Thus, the convolution method primarily requires an assumption about the ratio of moments of the assumed spectrum. The amount of years of reference can just be considered relatively high, e.g. 25 years. As a first example, Fig. 4.11 shows mean AoA and its trend calculated for ratio of moments 0.7 years and 1.25 years from the SF_6 tracer and from the linear tracer for the RC1-base-07 run. One can see that for 1.25 years of ratio of moment, the agreement between AoA calculated from the linear tracer and from SF_6 becomes very good. However, for a ratio of moments of 0.7 years the disagreement prevails. Similar to the fit method, deviations in mean AoA are found in the beginning of the AoA time series maximizing in the 1980s, resulting in an AoA trend that is less negative.

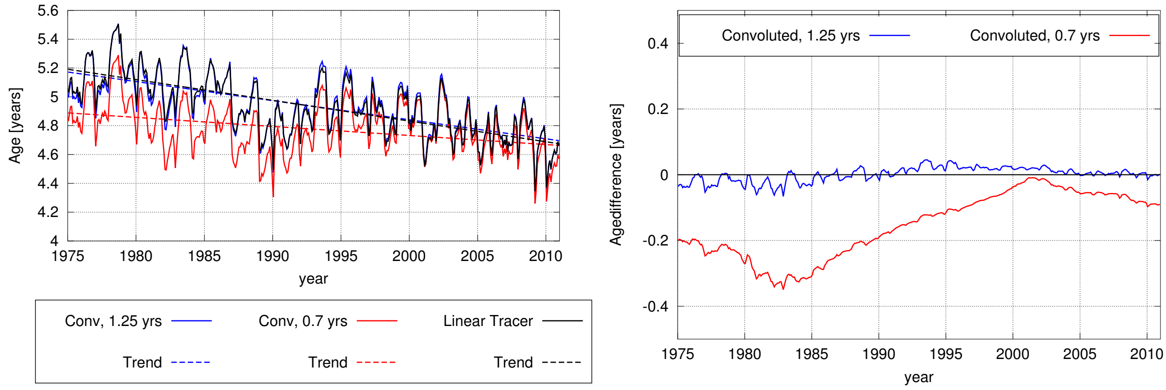

Figure 4.11: Left, mean AoA and its trend derived from SF_6 using the convolution method for 0.7 and 1.25 years ratio of moments (red and blue) and from the linear tracer (black) at 20 hPa and 40° N from 1975 to 2011 from the RC1-base-07 simulation. Right, the difference in mean AoA derived from SF_6 and the linear tracer.

Similar to Fig. 4.4, Fig. 4.12 shows, height-latitude plots of the mean absolute deviation between mean AoA calculated using the linear increasing tracer and the SF_6 tracer in color and the difference in their trends in 10^{-1} years decade^{-1} in white contours. The location of the balloon borne observations by [Engel et al., 2017] is indicated by the red boxes. Here one can see that overall, a ratio of moments of 0.7 years, which was applied to the balloon borne observations so far, leads to too small negative or even positive trends, which are insignificant.

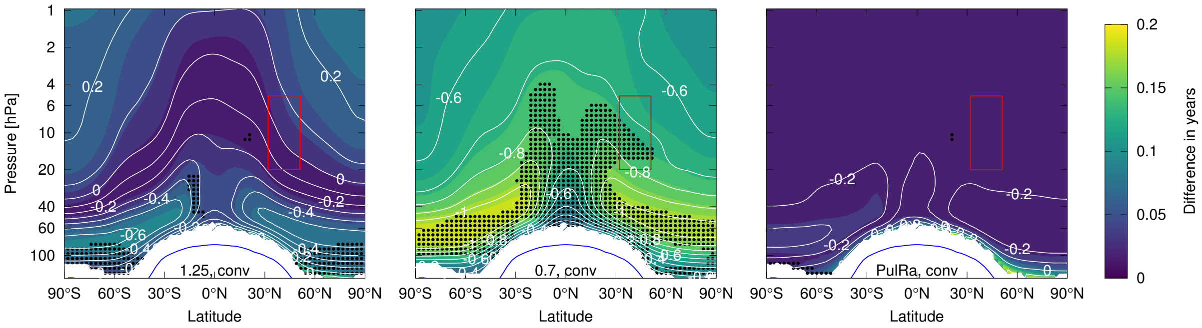

Figure 4.12: As Fig. 4.4, in color are the mean absolute deviation of mean AoA calculated from SF_6 from AoA derived from an ideal tracer for every month from 1975 to 2011 for different ratio of moments using the convolution method. The left panel is 1.25 years of ratio of moments and the middle is 0.7 years. PulRa denotes the ratio of moments derived from the tranPul simulation annual mean extended age spectra (right) The white contours are the difference in trends in 10^{-1} years decade^{-1}. White areas indicate where the derivation is not applicable. Black stippling shows insignificance of the SF_6 trend from zero on the 95% confidence level. The trend calculation considered the time series from 1975 to 2011. The red box shows the range of the balloon observations.

Specifically, in the range of the observation this is a deviation in mean AoA of 2.8% and in trend of 54%. This remains similar to applying this ratio of moments in the fit method. On the other hand, using the ratio of 1.25 years yields very good agreement in the range of the balloon borne observations (0.3% in mean AoA, 6% in trend). Again, using the spatial distribution of ratio of moments derived from the extended model spectra, finds good agreement, too (0.4% in mean AoA, 14% in AoA trend in the range of the observations).

4.3 Discussion

4.3.1 Model Results

It has been shown here, that the variation of the mean AoA trend due to the selection of parameters is larger than the internal variability (e.g. Fig. 4.3). One might suggest that models still have spin-up effects as the deviations in mean AoA are often in the beginning of the time series. Both simulations, tranPul and RC1-base-07, were started in 1950, but the first ten years were considered as spin-up. So the data is used starting in 1960, such that the first mean AoA values are calculated for 1975, as the mean AoA calculation fits the reference time series backwards. Previous tests on the effects of spin-up time on AoA in EMAC support that the mean AoA values shown here should not be considerably influenced by spin-up effects for this amount of spin-up. Hence, the differences between models and the observations are not due to spin-up effects in models. It is found that the major source of variation in SF_6-derived mean AoA especially using the fit method is the selection of parameters.

Another question to consider is whether a second order fit is appropriate to describe the SF_6 reference time series. Testing higher order fits shows, that the 3rd order coefficients would be two orders of magnitude smaller than the second order coefficients and the higher ones even smaller. Therefore, the second order assumption will be kept here. Especially since higher order calculations would require even more assumptions about the transport time distribution which would be even more difficult to constrain in measurement applications.

The convolution method enables to avoid uncertainties about the amount of time considered and the function that is fitted to the time series. Still, there is a high sensitivity to the ratio of moments and it remains open which ratio of moments is describing the atmosphere best. Still, it is rather certain, that larger ratios of moments are more realistic.

4.3.2 Recalculation of AoA from balloon borne observations

It is most valuable to put the results derived from the model data concerning parameters and methods of AoA calculations into context by testing whether the same tendencies are seen in calculations of observed AoA. The mean age values are recalculated from the observations by [Engel et al., 2017] with the fit method with different parameters and the convolution method with different ratio of moments. The results for the trends are given in Fig. 4.13 and Table 4.1.

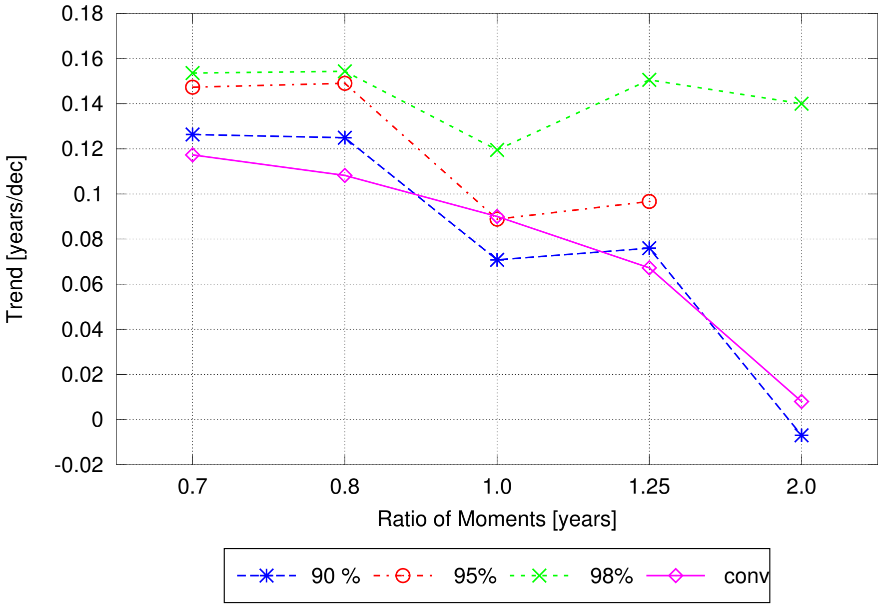

Figure 4.13: Trend in mean AoA derived from the observations for the fit and the convolution method for the respective fraction of input and ratio of moments.

Table 4.1: AoA trends recalculated from observations using fit method and convolution method for different parameters. Within the presented decimals, the errors are equal.

Method	Trend [years decade^{-1}] calculated from ratio		
	0.7 years	1.25 years	2.0 years
Fit, 98%	0.15 (±0.16)	0.15 (±0.16)	0.14 (±0.16)
Fit, 90%	0.12 (±0.16)	0.07 (±0.16)	−0.007 (±0.16)
Convolution	0.11 (±0.16)	0.07 (±0.16)	0.008 (±0.16)

In agreement to what was presented for the model data, there is little influence of the ratio of moments on the trend using the fit method for 98% fraction of input, as was used in the calculations so far. For 90% fraction of input, the trend becomes less positive and eventually even slightly negative for larger ratio of moments. Thus, the same tendencies towards smaller, respectively more negative trends for larger ratio of moments and smaller fraction of input are seen.

Applying the convolution method for larger ratio of moments gives smaller positive trends, too. This confirms what was seen from the model data. For both methods for the larger ratio of moments negative trends as seen in the models lay within the margins of error.

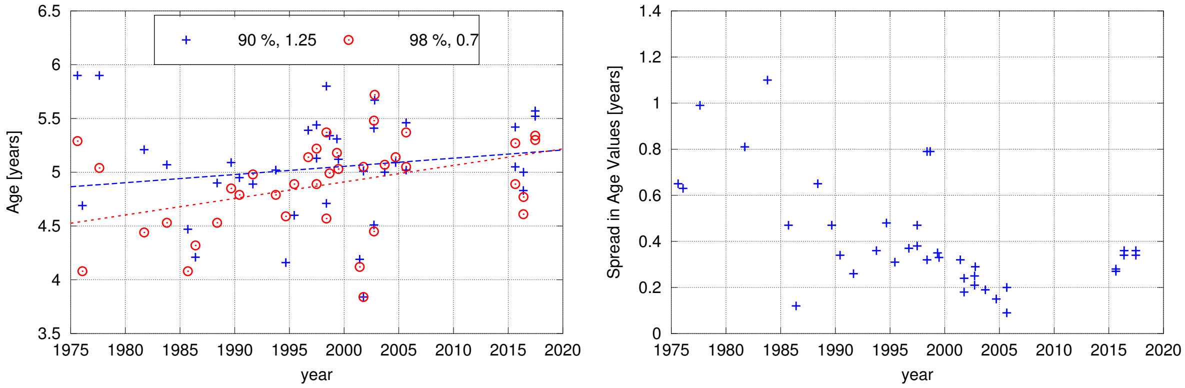

Figure 4.14: Left, example AoA time series derived from the observations using the stated parameters. Right, the difference between maximum and minimum mean AoA found from the observations for the considered parameters (0.7, 0.8, 1. 0 and 1.25 years for the convolution method and 90% 95% and 98% fit method).

Fig. 4.14 presents the AoA time series recalculated from the observations. On the left, the former parameter selection of 98% and 0.7 years for the fit method is displayed together with the recalculated version for 90% and 1.25 years. The right shows the spread in mean AoA for the different parameters and methods, that is 0.7, 0.8, 1.0 and 1.25 years for convolution method and 90% 95% and 98% for the fit method. The difference between the largest and smallest AoA value is shown. It becomes clear from the two plots, that the beginning of the SF_6 time series is more sensitive in the calculation, as seen for the model data.

Overall the results of this chapter show that the selection of parameters helps resolve the difference between model and observation AoA trends. Furthermore, it should be mentioned that [Volk et al., 1997] found good agreement with [Waugh et al., 1997] using a ratio of moments of 1.25 years for airborne in-situ measurements of SF_6. Applying this ratio of moments to the balloon borne observations results in mean AoA trends that agree to those of the model within the margins of error.

However, one should consider that the trend in [Engel et al., 2017] was derived from both SF_6 and CO_2 measurements. For calculations using CO_2 measurements methane oxidation is considered as a minor source. Here, the discussion was focused on the specific derivation methods themselves, such that CO_2 was not considered. Consequently, it was favorable to use a SF_6 tracer without mesospheric sinks. In particular, since the balloon borne observations under investigation are located between 5 hPa-30 hPa and 32° N-51° N where the influence of the mesospheric SF_6 sinks has so far been considered as small. In addition, the combination of

CO_2 and SF_6 balloon borne observations would make an influence of SF_6 sinks on the mean AoA trend less clear. However, the SF_6 sinks are important to consider when discussing the specific differences between mean AoA derived from the global MIPAS satellite SF_6 observations and models as [Linz et al., 2017] did, especially in the light of recent studies that report shorter lifetimes for SF_6 than assumed so far [Leedham Elvidge et al., 2018, Ray et al., 2017].

4.4 Conclusions

In this chapter, the sensitivity of the derivation of mean AoA to parameter choices that are necessary in the fit and convolution methods were investigated using EMAC as a model testbed. References available in a model such as a linearly growing AoA tracer and age spectra allow specific testing of the methods.

In the analysis of this chapter, a systematic variation of the mean AoA trend derived from SF_6 dependent on the ratio of moments and the fraction of input used in the AoA calculation when applying the fit method were found. The mean AoA values in the beginning of the time series are particularly sensitive to the ratio of moments and become larger with larger ratio of moments leading to more negative trends. In addition, the larger the fraction of input is, the more towards positive the trend. While the sensitivity to the ratio of moments was included in the error range by [Engel et al., 2009], the usage of a fixed fraction of input of 98% reduced the sensitivity to the ratio of moments in their study.

Investigating another method to derive mean AoA, namely the convolution method, showed the same relation of smaller negative AoA trends for larger ratio of moments. The convolution method only assumes the ratio of moments. It provides very good agreement between AoA from SF_6 and the linear tracer for the correct ratio of moments.

Applied to the balloon borne observations was the fit method with a small ratio of moments (0.7 years) and a large fraction of input (98%), which both tend to shift the trend towards more positive values. Based on model results, better agreement with a linear AoA tracer is found for ratio of moments of about 1.25 and fraction of input of 95%. Therefore, the parameter selection helps to resolve why the mean AoA trends found in [Engel et al., 2009] and [Engel et al., 2017] are positive, while models show negative trends.

The model results suggest using ratio of moments larger than 0.7 years. Using ratio of moments within the range 1.25-2 years is in line with what other 3d-model studies suggest [Waugh et al., 1997, Hauck et al., 2019]. Specifically, using a spatial distribution is favorable as it considers aspects such as the broadening of the spectra due to mixing lower in the stratosphere.

Testing the impact of the parameter choice on AoA derived from the balloon borne observations shows the same sensitivities for fit and convolution method as seen in the model. Within the margins of error the trend in AoA from observations and EMAC agree when assuming large ratio of moments (2 years). However, as the ratio of moments in the real atmosphere is currently unknown, it cannot be concluded whether such a large ratio of moments is realistic. Overall, understanding the systematic influence of the parameter selection on the trend of mean AoA provides further insight in addition to the existing work on the uncertainties of mean AoA and its trends. The results of this chapter clearly highlight the benefits of the consistent model evaluation of methods that are applied to observations.

Chapter 5

Transit time distributions of chemically depleted species

This chapter addresses the question, how tracer time series of a depleted substance can be propagated in a given climate scenario. With a focus on transport time distributions, in addition to the age spectra of inert tracers, now those transport time distributions of depleted substances and their products shall be considered. Those transport time distributions are available in the chemPul-2000 simulation by the implementation of chemically depleted pulses. Consequently, also derived measures such as mean AoA and path integrated lifetime will be investigated with regards to their interdependence and possible approximations.

5.1 Age of Air measures in the year 2000

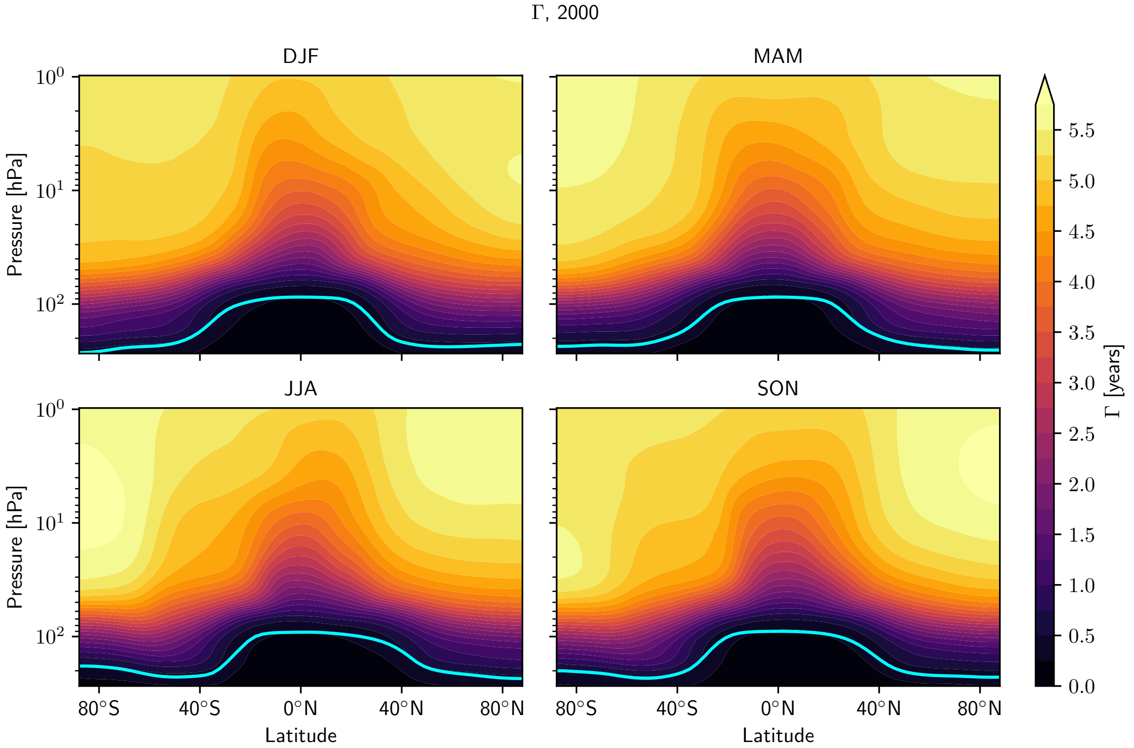

Figure 5.1: Seasonal mean AoA Γ obtained directly as the first moment of the age spectra from the chemPul-2000 simulation. The cyan line indicates the tropopause.

To begin with, this chapter will transition from mean AoA derived from a tracer time series as discussed in the previous chapter to mean AoA calculated from the first moment of the age spectrum. First, Fig. 5.1 shows the seasonal mean AoA from the chemPul-2000 simulation. The age spectra are monthly sampled and run for ten years. As previously, after ten years of transit time, the tail of the spectrum is extended with an exponential fit to the last five years of the spectrum to provide more accurate mean AoA values.

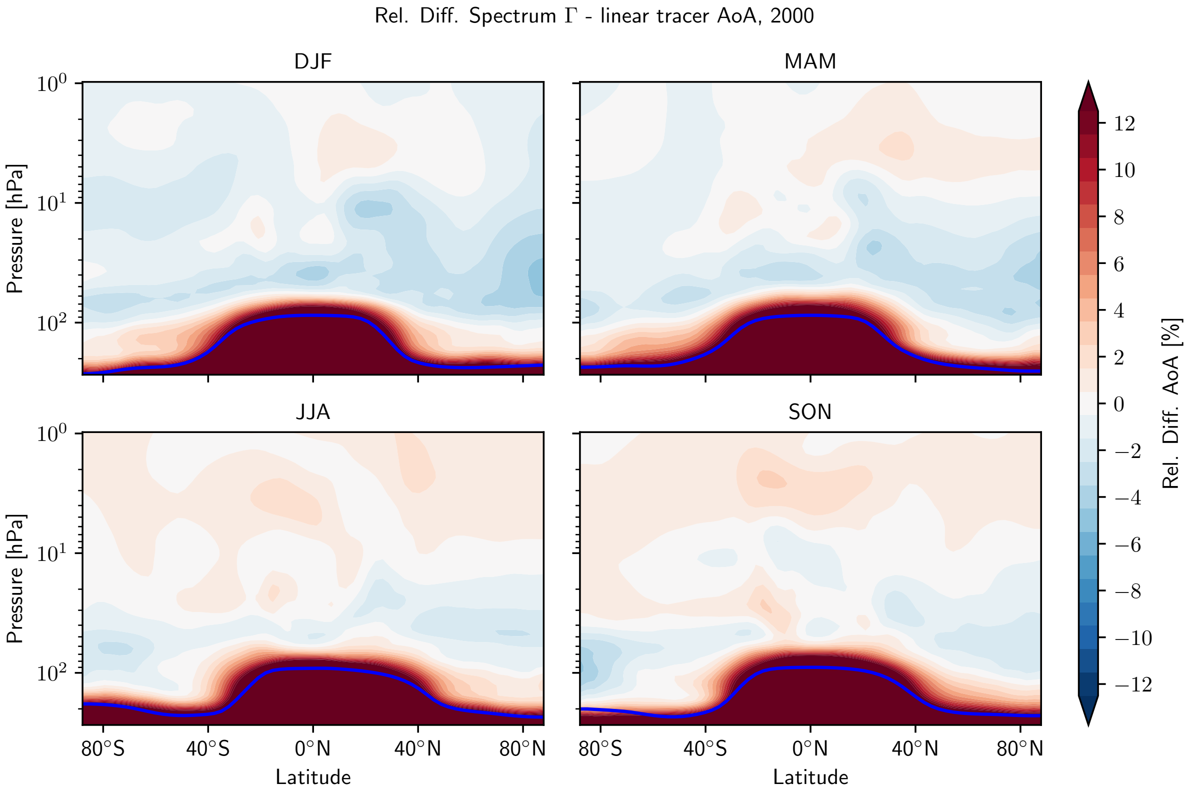

Figure 5.2: Seasonal relative difference of Γ calculated from age spectra and from a linear tracer

A linear AoA tracer or time evolving age spectra are continuously sampled. In contrast, the spectra in the chemPul simulations have a certain sampling bias, as explained in Sec. 3.2.1. Therefore, Fig. 5.2 shows the relative difference of mean AoA derived from the linear tracer and the age spectrum in the chemPul-2000 simulation. It is very clear from this figure, that the troposphere is not suitable for investigation as the different implementation of the diagnostic tracers leads to very noticeable biases. However, throughout the stratosphere the relative differences in mean AoA remain below 3% with a small area of 4% in the SON SH lower polar stratosphere. If the agreement had not been satisfactory more pulses or a transient spectra implementation would have been necessary.

To further reach a better understanding how well mean age of air from a continuously sampled AoA tracer and a sporadically sampled age spectrum can agree, Fig. 5.3 shows the standard deviation of the mean AoA values of the linear tracer. The standard deviation of the linear tracer AoA shows, which regions are subject to high inter-annual variability, and how large the inter-annual variability is anticipated to be. This information helps to judge, if the sporadic sampling of the age spectra is too sparse. As anticipated, similarities in the standard deviation are noticeable to Fig. 3.3 in Sec. 3.2.1 which considered the cumulative error of age of air Spectra. Both, the standard deviation of mean AoA from a linear tracer

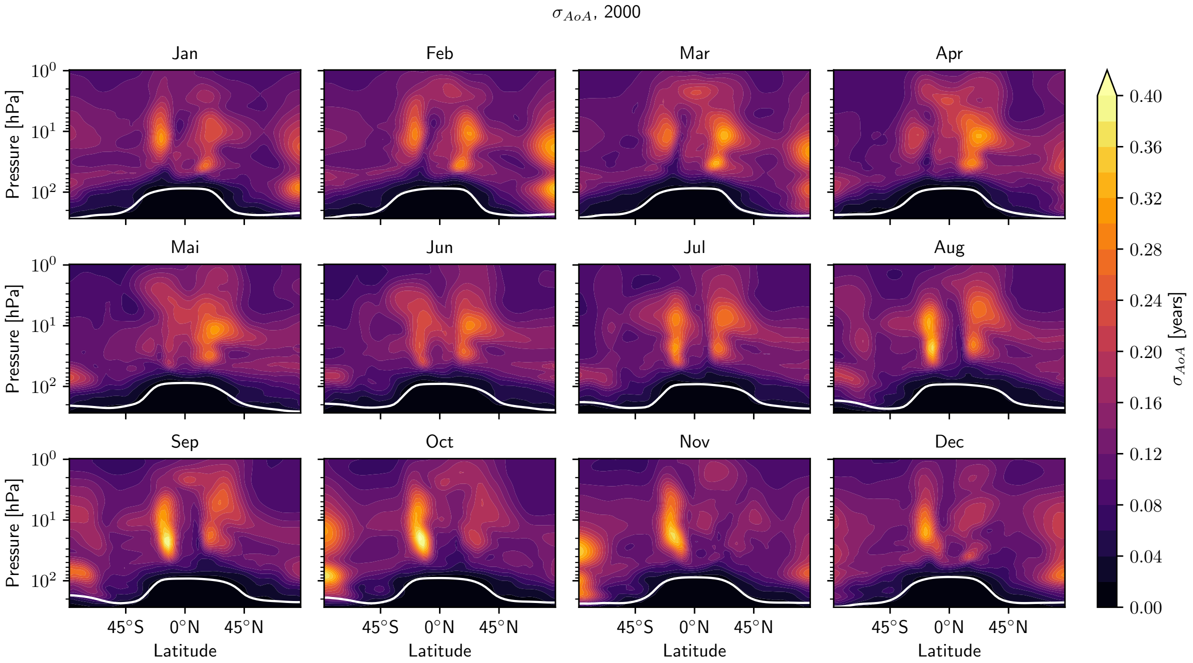

Figure 5.3: Standard divination σ of Γ from linear tracer across the simulated years for every month.

and the cumulative error of the age spectra show the strongest variability where atmospheric variability is strongest. Again, the region around the tropical pipe shows the highest variability of up to 0.4 years. Here, the southern polar region shows more noticeable variability in late autumn.

5.2 Discussion of the local path integrated lifetime

As already conceptually introduced in Fig. 2.7 in Sec. 2.3, depending on the specific pathway a tracer takes to a certain location it is subject to different loss. Now, Fig. 5.4 makes this statement more specific. The colors show the local, path integrated lifetime $\bar{\tau}$ of N_2O as seasonal means, calculated as explained in Sec. 2.3.2. The overlaid contours show the corresponding mean AoA. As a measure of transport only, the mean AoA isolines show the familiar patterns dominated by the tropical upwelling and the polar down-welling of older air. As a measure of both, transport and depletion, the $\bar{\tau}$ isolines are latitudinally more flat than the Γ isolines that are more bend upwards in the tropics. In the lower stratosphere, $\bar{\tau}$ is rather large, as the example of N_2O does not have considerable sinks in the troposphere. Overall, the lifetime decreases with altitude, as the air is transported to the major depletion regions higher up where photolysis occurs as less photons were absorbed. Though, N_2O is picked as an example here, the qualitative picture is the same for all considered species.

From Fig. 5.4, one might suggest that it is possible to distinguish two regions, the tropics and the extratropics, such that the isolines of Γ and $\bar{\tau}$ follow each other. To consider this idea, Fig. 5.5 shows $\bar{\tau}$ vs. Γ for N_2O for all stratospheric locations. The regions outside of 38° are colored rust and the tropical regions teal. Two main lines could be identified, though there remains a considerable spread across several orders of magnitude of $\bar{\tau}$ considering the

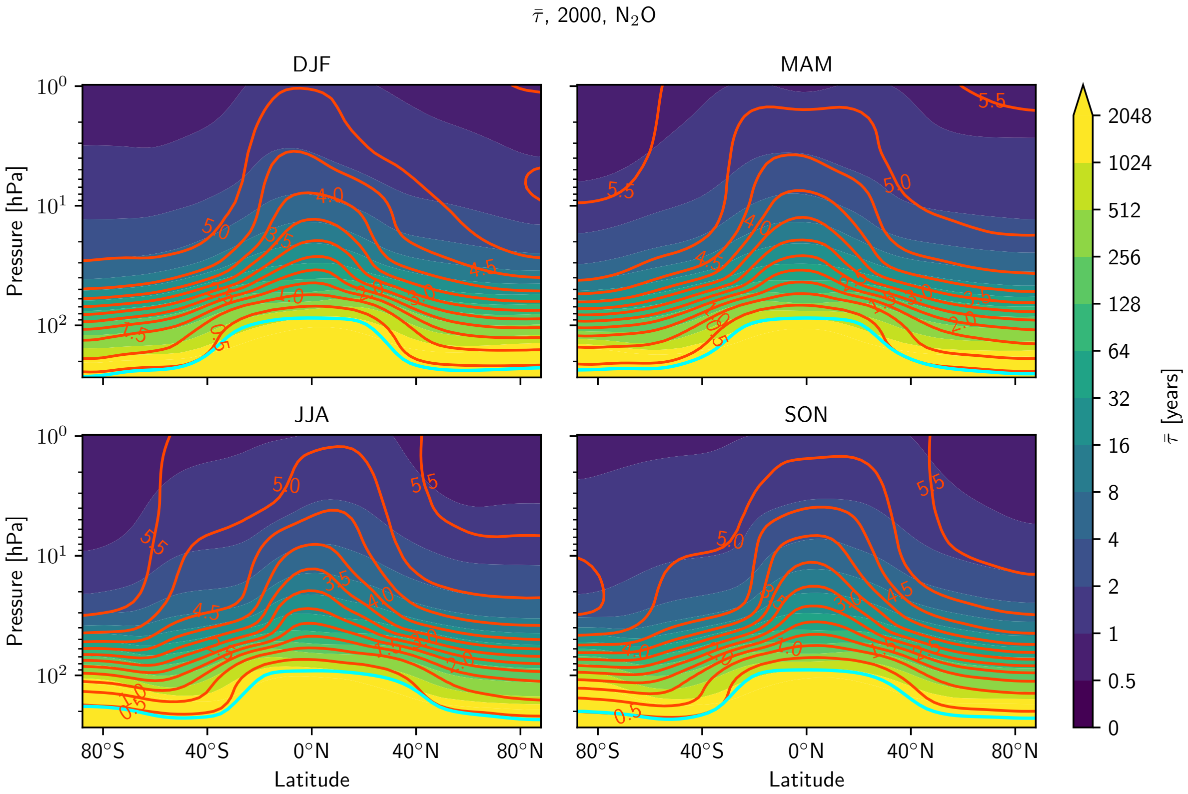

Figure 5.4: The colors show the local path integrated lifetime $\bar{\tau}$ for N_2O for every season, the overlaid contours show mean AoA Γ derived from spectra as Fig. 5.1.

logarithmic scale of the $\bar{\tau}$ axis. The other species with predominantly stratospheric loss show a similar $\bar{\tau}$ vs. Γ pattern scaled according to their lifetimes.

In the case of species with considerable tropospheric loss, i.e. CH_3Cl, CH_3Br and CH_3CCl_3, the $\bar{\tau}$-Γ distributions keeps a right curvature. As an example of this, $\bar{\tau}$ vs. Γ of CH_3Br is given in Fig. 5.6. The loss in the troposphere means, that for shorter transit times, chemical depletion is possible, so that the lifetime $\bar{\tau}$ for small Γ decreases compared to tracers with no considerable tropospheric loss. This means that even though, e.g. CH_3Br and CF_2ClBr have quite similar stratospheric lifetimes (40.2 years and 39.5 years) their $\bar{\tau}$-Γ distributions look quite different. This consideration illustrates clearly that in order to derive a way to approximate $\bar{\tau}$ from Γ, the predominant loss regions need to be considered.

To provide even more detail on the distributions of $\bar{\tau}$ and Γ, Fig. 5.7 shows age spectrum $G(t)$ and transit time dependent lifetime $\tau(t)$ for mean AoA $\Gamma = 3$ years for different NH latitudes for CF_2Cl_2. This helps in understanding which distributions of G and τ lead to certain integrated values of mean age Γ and path integrated lifetime $\bar{\tau}$. The example picked here is CF_2Cl_2 in DJF though the relative statements remain valid for the other species and seasons, too. From Fig. 5.7 it can be seen, that $G(t)$ in the tropics has an rather isolated peak at later transit times compared to the extratropics as the transport in the tropics is dominated by the residual transport. In comparison in the extra tropics, because of e.g. fast mixing, contributions to the age spectrum are already found at shorter transit times. Due to the representation relative to $\Gamma = 3$ years, $\tau(t)$ closer to the equator is smaller at shorter transit times. This

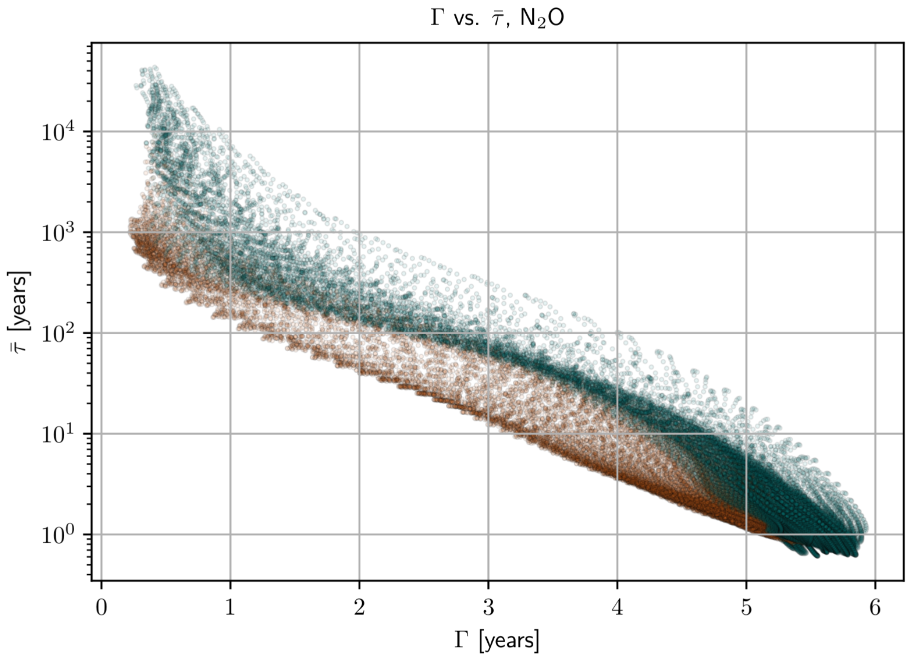

Figure 5.5: Stratospheric mean AoA Γ vs. local path integrated lifetime $\bar{\tau}$ for every grid and time point for N_2O from the chemPul-2000 simulation. Teal shows the region from 38° S to 38° N, rust shows the regions poleward from 38° S and 38° N

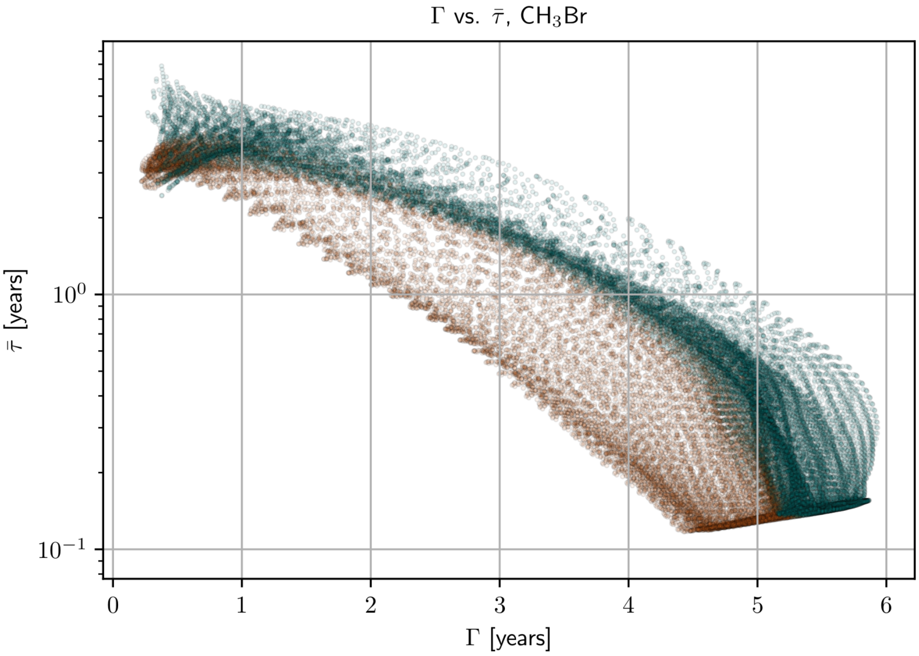

Figure 5.6: Similar to Fig. 5.5, stratospheric mean AoA Γ vs. local path integrated lifetime $\bar{\tau}$ for CH_3Br from the chemPul-2000 simulation. Teal shows the region from 38° S to 38° N, rust shows the regions poleward from 38° S and 38° N

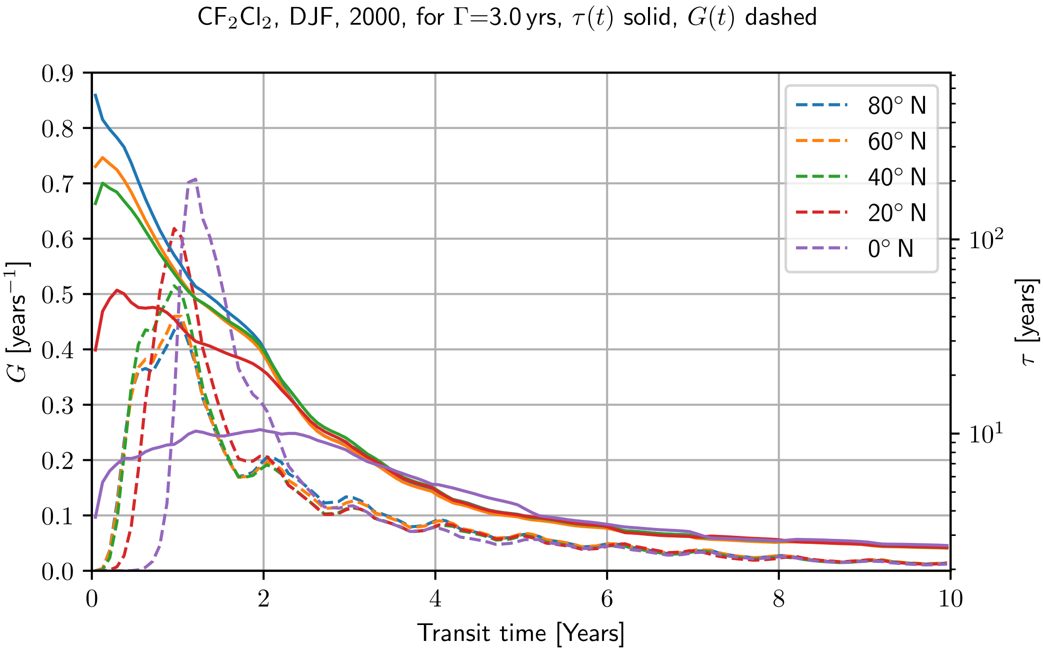

Figure 5.7: Age spectrum $G(t)$ (dashed) and transit time dependent lifetime $\tau(t)$ (solid) for $\Gamma = 3$ years for CF_2Cl_2 for DJF for the stated latitudes (legend).

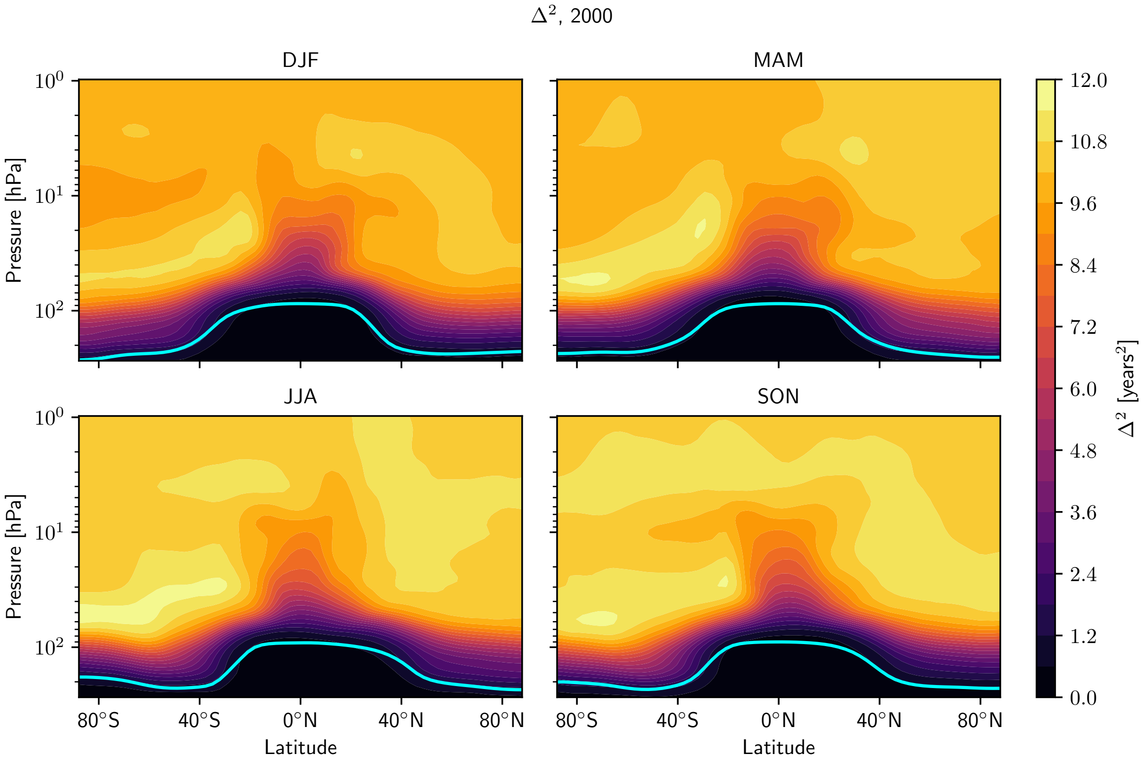

Figure 5.8: Seasonal mean width Δ^2 of the age spectrum for the chemPul-2000 simulation.

can be understood as the isolines of Γ are located higher closer to the equator. Therefor the impact of photolysis is stronger and the transit time dependent lifetime is smaller. For transit times above ca. 3.5 years the age spectrum $G(t)$ and the transit time dependent lifetime $\tau(t)$ for different latitudes become indistinguishable as recirculation effects become more relevant.

When discussing the shape of $\bar{\tau}$ relative to the mean AoA Γ, it makes sense to consider the distribution of the width of the age spectrum and its ratio of moments, too. Therefore, Fig. 5.8 shows the seasonal mean width and Fig. 5.9 the ratio of moments of the age spectra. A suggested assumption would be, that as longer transit times contribute to the age spectrum either width or ratio of moments are shifted and at the same time more of the tracer is depleted.

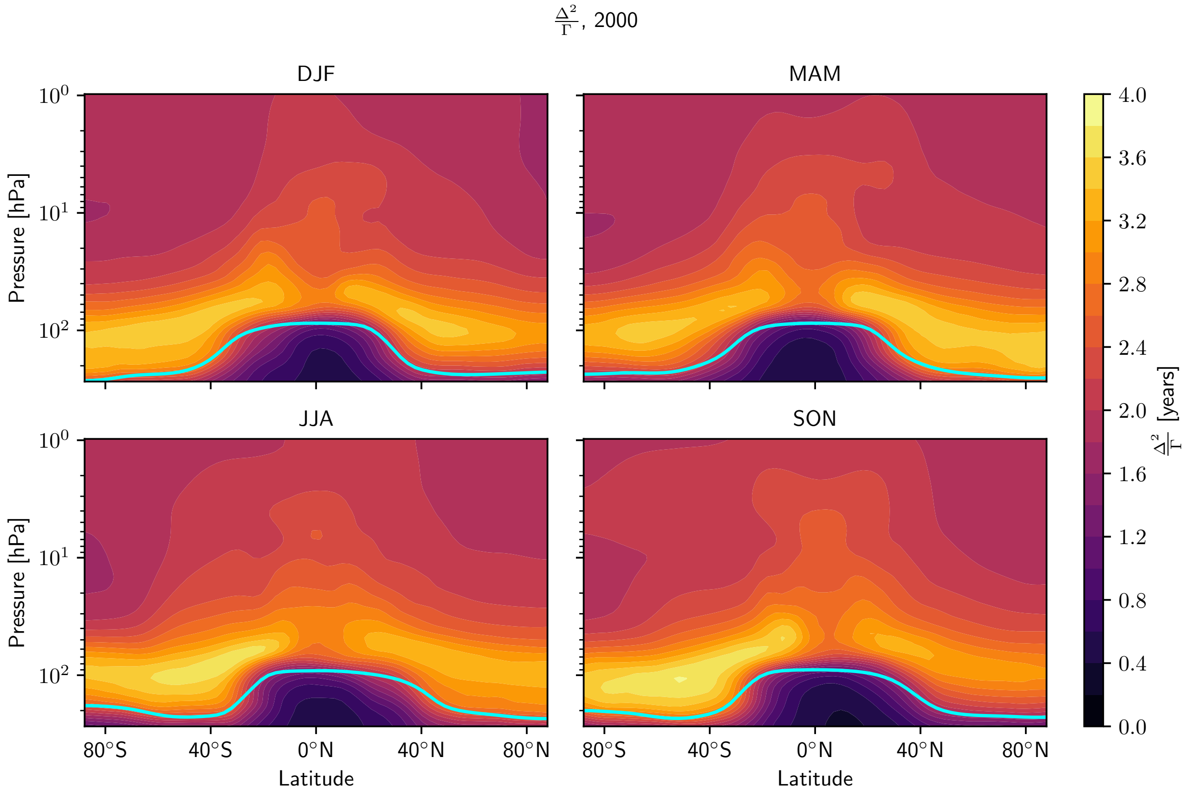

Figure 5.9: Seasonal mean ratio of moments Δ^2/Γ of the age spectrum from the chemPul-2000 simulation.

However, in the tropics the width of the age spectrum shows the relatively strong minimum in the tropics which the path integrated lifetime $\bar{\tau}$ as a measure of transport and depletion does not have. Also the ratio of moments shows the already familiar regions of largest ratio of moments above the tropopause predominantly in the extratropics, which implies a relative minimum in the tropics above the tropopause. Therefore, the $\bar{\tau}$ isolines do not align to those of the ratio of moments either. Hence it can be concluded that $\bar{\tau}$ does not have a simple direct dependency to the width or ratio of moments of the age spectrum either.

The different considerations about the shape of the age spectrum relative to $\bar{\tau}$ highlight, that the local path integrated lifetime $\bar{\tau}$ is a measure that considers both transport and spatial and temporal depletion of a tracer. Therefore, $\bar{\tau}$ cannot be approximated straightforward by transport measures alone, but considerations about the predominant loss region and the strength of the loss are also required. This statement applies to all species and seasons.

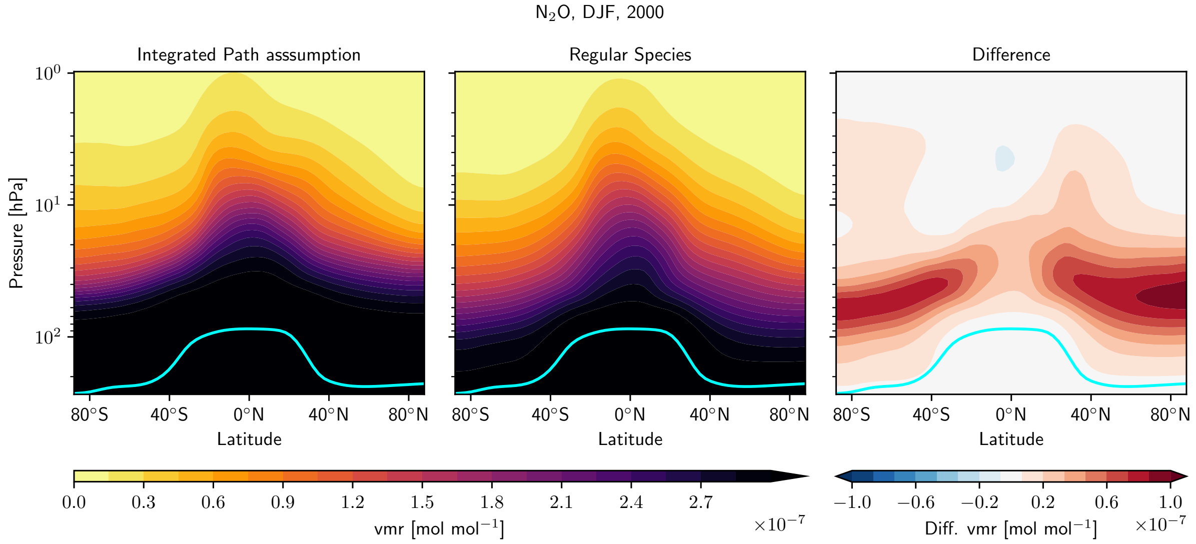

Figure 5.10: Calculation of the mixing ratio using $\bar{\tau}$ (left), regular tracer mixing ratio (middle) and their difference (right) for N_2O DJF

Knowledge about the path integrated lifetime $\bar{\tau}$ is useful, when the integrated path assumption by [Schoeberl et al., 2005] is considered, which was explained in more detail in Sec. 2.3.2. An exponential decay function with $^1/_{\bar{\tau}}$ as decay constant, the age spectrum and the reference time series allow to project the mixing ratio of a chemically depleted tracer. In [Schoeberl et al., 2005], they investigated this projection in a CTM. CCM applications of this method to date focused on tracers with predefined lifetimes, such as [Hauck et al., 2019]. Fig. 5.10 shows the test of this projection compared to the full tracer for the example of N_2O in DJF. For a wide range of the atmosphere, the projection shows to be accurate. Slightly above the tropopause in the extratropics the assumption deviates from the full tracer. Typically the deviation reaches about 50%. The region of deviation from the actual model tracer is similar (respectively, located slightly higher) to the region where the ratio of moments of the age spectrum has the largest values. Probably due to mixing, an time integrated average $\bar{\tau}$ does not hold valid there.

Fig. 5.11 presents the seasonal mean deviations of calculated N_2O mixing ratio for a transit time dependent lifetime $\tau(t)$ from the actual model mixing ratio. It is evident, that the regions of disagreement in Fig. 5.10 are noticeably reduced when applying $\tau(t)$ instead of the path integrated lifetime $\bar{\tau}$. Thus, the test further supports that an path integrated $\bar{\tau}$ is less suitable for those regions. Already from Fig. 5.7 it could be seen for CF_2Cl_2, that in the regions that are poorly approximated by an average lifetime, $\tau(t)$ stretches across several orders of magnitude. Even though not shown here, this is applicable for N_2O, too. Applying the transit time dependent lifetime $\tau(t)$ is equivalent to using the arrival time distribution G^*. Therefore, this test also shows that with the chemPul-2000 implementation the temporal variability and the chemical loss are well enough represented for this method to work. In addition, the example of N_2O is representative of the propagation of the other species.

Eventually, it can be concluded that it is highly beneficial to use models to specifically calculate $\bar{\tau}$, respectively $\tau(t)$ from a full 3D CCM. The comparison of projected mixing ratios

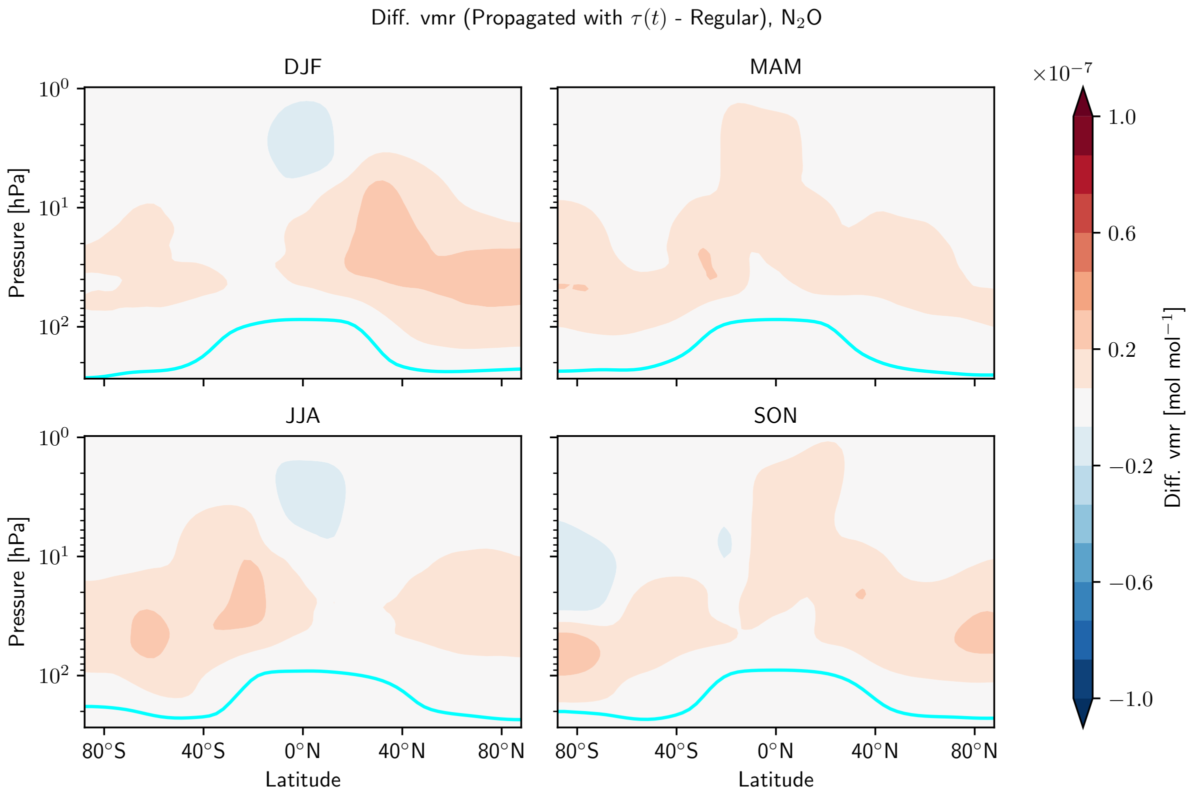

Figure 5.11: Seasonal difference between the calculated mixing ratio using $\tau(t)$ and the regular tracer mixing ratio for N_2O (See also Fig. 5.10).

and model mixing ratios shows that the integrated path assumption of [Schoeberl et al., 2005] holds true for a wide range of the stratosphere. Thereby it is possible to calculate the mixing ratio of chemically depleted species from ground measurements. The model results can aid to constrain $\bar{\tau}$ for those observational applications. Even though a time dependent τ provides even better results, it would require detailed assumptions for experiment applications.

5.3 Discussion

5.3.1 Mean AoA and Lifetime

Some examples on previous work on the connection between chemical lifetime and mean AoA were based on the initial question of treating chemical loss correctly when deriving AoA from measurements of semi-inert tracers [Ray et al., 2017, Leedham Elvidge et al., 2018, Laube et al., 2013]. It is well illustrated by [Ray et al., 2017, Leedham Elvidge et al., 2018], that the specific lifetimes of the respective tracers lead to noticeable spreads in derived apparent mean AoA if not considered correctly, especially in the upper stratosphere. Though, this previous work is based on lifetime of large scale regions, i.e. stratospheric lifetime, or relative lifetime (i.e. relative to another tracer) rather than path integrated lifetime. Thus, there is no direct comparability to the results shown here. Though, the path integrated lifetime is explored as a possibility to bridge the gap between local loss rates, that are limited with regards to understanding the full impact on tracer distributions, and the stratospheric lifetime, that does not describe smaller regions in detail. The application possibilities and the general concept of path integrated lifetimes is well introduced in [Holzer and Waugh, 2015]. However, their work is focused on the transport between different surface regions therefore no closer discussion is possible here. Based on the work by [Holzer and Waugh, 2015] is [Yang et al., 2018] which considered a box model including troposphere and stratosphere to obtain path integrated lifetimes of hydrochlorofluorocarbons (HCFC). Among their results they showed, that integrated across the whole domain, their path integrated lifetimes agreed with the global lifetime in their model. Another lifetime realization was shown in [Prather, 2007]. They released single pulses of chemical species in a CCM. In contrast to the simulations shown here, the pulses do perturb the chemistry of the regular tracer, thus this is treating an eigenvalue problem of characteristic time scales. Thus, their approach might seem similar at first glance but serves a different purpose. Further, rather the deriving transit time distributions from several pulses, they only consider single pulses.

5.3.2 EESC

One application of the projection of mixing ratio of chemically depleted species is given by EESC, which was already introduced in Sec.2.3.3. In the case of EESC it is the projection of the product of the depletion of a species, namely chlorine and bromine, that is of interest. By calculating EESC, the stratospheric halogen burden can be described and the expected effect on stratospheric ozone recovery can be quantified. Here, the methods to calculate EESC presented by [Newman et al., 2007] using the age spectrum and [Engel et al., 2018] using the release time distribution are considered which where explained in detail in Sec.2.3.3. In [Engel et al., 2018], before determining EESC, the first moments of the release time distribution $G^{\#}$ and arrival time distribution G^{*}, namely the mean release time $\Gamma^{\#}$ and mean arrival time Γ^{*} are approximated. The mean fractional release $\bar{f}$ is then calculated from the assumed $G^{\#}$, considering an inverse Gaussian assumption, as previously applied for the age spectrum (Eq. 2.10) Therefore, the results obtained from the chemPul-2000 simulations are compared to those of from simple assumptions in Table 5.1.

In [Engel et al., 2018], mean arrival time Γ^{*}, mean release time $\Gamma^{\#}$ and mean fractional release $\bar{f}$ were calculated for a reference value of mean AoA of 3 years. Taking mean AoA as the relative coordinate instead of location is convenient when using the inverse Gaussian assumption for the transport time distributions. The selection of $\Gamma = 3$ years was picked to represent NH lower stratosphere mid-latitudes. They also considered 60 hPa and 30-60° N as a location to represent $\Gamma = 3$ years when comparing to EMAC results. Though in the chemPul-2000 simulation, the region 60 hPa and 30-60° N does not average to $\Gamma = 3$ years. To pick a similar location and still consider a range that shows a mean age of three years, the region was slightly altered to 60 hPa and 40-60° N. As can be seen from Table 5.1, the mean release time $\Gamma^{\#}$ is smaller for five tracers in the chemPul-2000 simulation while the mean arrival time Γ^{*} is larger for all tracers. Thus, the simulation results for the first moments tend to be more affected by the chemical loss than assumed by the simple approximation. This is maybe counter intuitive, as the model implementation of the arrival time distribution neglects some of the loss in the chemPul simulations (See Sec.3.2.2). Further, $\bar{f}$ is larger for most species in the model simulation. Again, the mean fractional release is calculated from the integral over the release time distribution. The exponential extension which is already

Table 5.1: Mean arrival time Γ^*, mean release time $\Gamma^\#$ and mean fractional release $\bar{f}$ estimated from an inverse Gaussian assumption and from the model simulations for $\Gamma = 3$ years, respectively 60 hPa $40 - 60°$ N. Γ^* and $\Gamma^\#$ are given in years. The model fractional release $\bar{f}$ is given for extended and non-extended release time distribution $G^\#$.

Species	Est. Γ^*	Model Γ^*	Est. $\Gamma^\#$	Model $\Gamma^\#$	Est. $\bar{f}$	Model $\bar{f}$	$\bar{f}$ unextended
CF_2Cl_2	2.0	1.7	6.2	6.5	0.24	0.27	0.24
CH_3Cl	1.9	1.6	4.4	5.2	0.44	0.38	0.36
CF_3Br	1.7	1.4	6.0	5.6	0.32	0.38	0.35
$CFCl_3$	1.5	1.2	4.7	4.8	0.47	0.49	0.47
CCl_4	1.4	1.1	4.3	4.4	0.56	0.55	0.54
CH_3Br	1.3	1.0	4.1	4.0	0.60	0.63	0.62
CF_2ClBr	1.3	1.0	4.0	3.9	0.65	0.67	0.66
CH_3CCl_3	1.4	1.1	4.1	4.4	0.61	0.56	0.54

known from the age spectra was applied to the release time distribution obtained from the model results. The extended release time distribution considers more input than the non-extended release time distribution and leads to larger $\bar{f}$ values. To make this more specific, the last column of Table 5.1 gives the values for the mean fractional release obtained from the non-extended $G^\#$. Comparing the $\bar{f}$ from the non-extended release time distribution from the model results and the simple approximation $\bar{f}$, it can be seen, that if the approximated mean fractional release is smaller, the approximated mean release time is larger. This is clear, as [Engel et al., 2018] calculated the mean release time from the mean fractional release and the mean arrival time. Hence, the differences in mean release time stem from the differences in mean fractional release and mean arrival time between the model results and the assumptions for the simple approximations.

More precisely, in [Engel et al., 2018] mean arrival time Γ^* was obtained from the calculations in [Plumb et al., 1999]. [Plumb et al., 1999] approximated the mean arrival time relative to the mean AoA by an exponential decay using a constant lifetime τ. In addition, the assumptions from [Ostermöller et al., 2017] for the age spectrum and the arrival time distribution were considered when obtaining the mean fractional release. First, their formulation to transfer the fractional release given in [Newman et al., 2007] to mean fractional release by means of arrival and release time distribution (Sec. 2.3.3) was applied. In their work the mean fractional release was termed “time independent fractional release” as it does not depend on the ground time series of the tracer. Second, the age spectrum and arrival time distribution were assumed to be inverse Gaussians with ratios of moments of 0.7 years. We already know, that $^{\Delta^2}/_{\Gamma}$ is larger in EMAC. In addition, $^{\Delta^{*2}}/_{\Gamma^*}$ is species depended in the model results, though the value 0.7 years actually agrees for some species in some regions (not shown).

In the next step, the release time distribution $G^\#$ from the chemPul-2000 simulation results is used to calculate EESC. Fig. 5.12 shows EESC obtained from an assumed age spectrum G, an assumed release time distribution and an annular mean release time distribution from the chemPul-2000 simulation. To investigate the impact of the differences in shape of assumed and modeled release time distribution onto EESC, the mean fractional release and the mean release time from the modeled release time distribution are considered for the assumed inverse

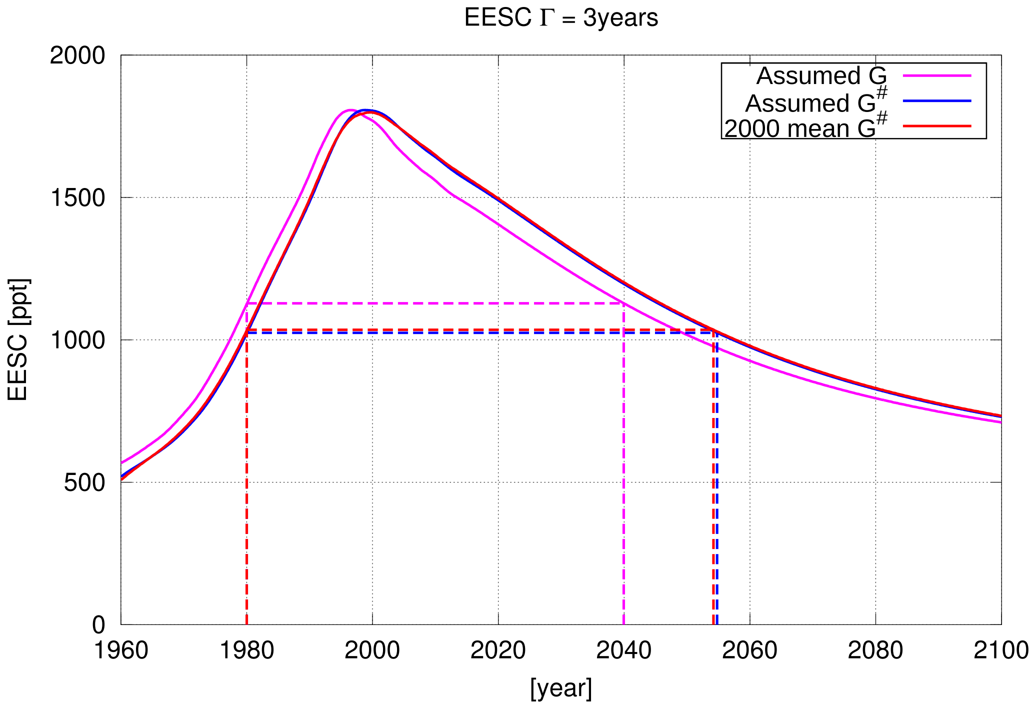

Figure 5.12: EESC for $\Gamma = 3$ years for assumed release time distribution $G^{\#}$ (blue) and age spectrum G (pink) and modeled $G^{\#}$ (red).

Gaussian shaped release time distribution. As in Table 5.1, respectively 60 hPa and 40-60° N were considered to represent 3 years mean age as the reference for the EESC calculation. In all three EESC calculations those ODS were considered that are available as modeled arrival time distributions. The missing ODS result in different recovery dates to 1980 values than anticipated by other sources such as [Engel et al., 2018] who found 2049 and 2060 as respective recovery dates. Nevertheless, for a relative comparison of the methods, considering the recovery date is still a meaningful measure. Using the assumed G, a recovery date of 2040 is obtained. As anticipated, the shift to an assumed $G^{\#}$ gives a later recovery date of 2055. Applying the $G^{\#}$ from the model results gives a similar recovery date of 2054, as the inverse Gaussian is a suitable approximation for the annular mean $G^{\#}$. Hence, it can be concluded, that to calculate EESC at $\Gamma = 3$ years it is foremost important to obtain the correct mean release time and mean fractional release while the differences in specific shape of the release time distribution are were found to be of smaller importance. The comparison was done for annular mean modeled release time distribution and assumed release time distribution, which are already similar in shape. The importance of correct values for the mean release time and the mean fractional release is also clear from the shift between EESC from assumed G compared to assumed $G^{\#}$ which is foremost a shift in first moment and fractional release applied to the same inverse Gaussian with the same ratio of moments.

Another publication that needs to be considered more closely is by [Leedham Elvidge et al., 2018]. The main focus of their work is to make more long lived tracers available as age tracers, predominantly ODS, based on aircraft measurements. In doing so, the fractional release and lifetime is considered according to the work of [Ostermöller et al., 2017, Plumb et al., 1999].

For the calculation of the fractional release they assume a width of 0.7 years for the release time distribution. As to my knowledge the first full CCM implementation of this formulation is presented here, Fig. 5 in [Leedham Elvidge et al., 2018] which presents mean AoA vs mean fractional release for CF_3Cl, HCFC-22 and CH_3CCl_3 can be compared directly for the first time. In addition to the results of [Leedham Elvidge et al., 2018], the work of [Newman et al., 2007, Laube et al., 2013] are considered in the mentioned figure. Though, HCFC-22 is not included in the chemPul simulations as an arrival time distribution. HCFC-22 is influenced even more by tropospheric sinks than any of the species included as arrival time distributions. Therefore, Fig. 5.13 shows the mean AoA vs. the fractional release of $CFCl_3$ and CH_3CCl_3.

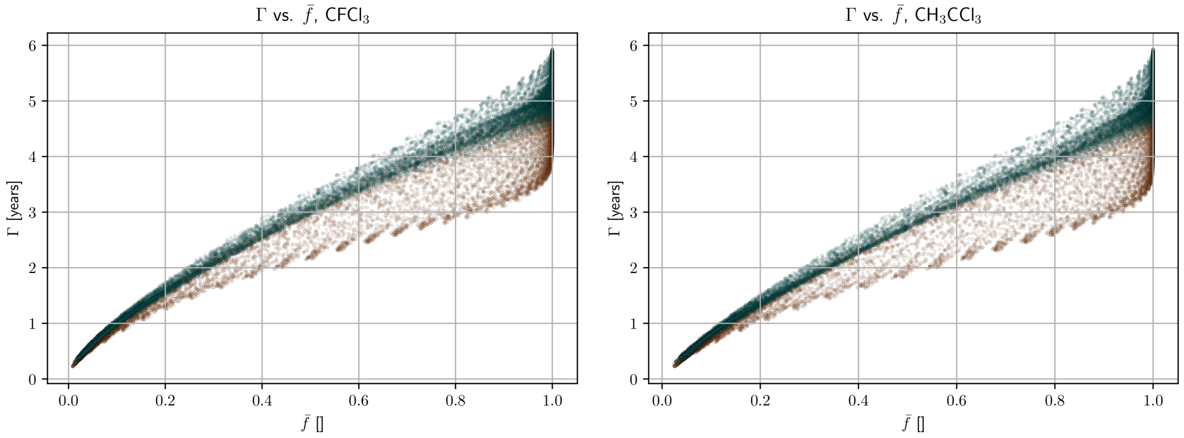

Figure 5.13: Stratospheric mean AoA vs. mean fractional release for $CFCl_3$ (left) and CH_3CCl_3 (right). Teal shows the region from 38° S to 38° N, rust shows the regions poleward from 38° S and 38° N

For both [Leedham Elvidge et al., 2018] and Fig. 5.13, $CFCl_3$ and CH_3CCl_3 have similar magnitude regarding their mean fractional release for given mean AoA, as they have similar stratospheric lifetimes. Compared to [Leedham Elvidge et al., 2018], the chemPul-2000 simulation finds larger fractional release values for a given mean AoA value of up to 0.1. This was already clear from the previous comparison to [Engel et al., 2018] that showed larger fractional release values for the chemPul-2000 simulation for mean AoA being 3 years. As anticipated from Fig. 5.5 and 5.6, a distinction of fractional release vs. mean AoA between high latitudes (poleward of 68°) and low and middle latitudes becomes apparent in Fig. 5.13. For the same mean AoA value, the fractional release is larger at high latitudes. This cannot be seen from [Leedham Elvidge et al., 2018] even though they include aircraft measurements from middle and high latitudes. Overall, the relation between fractional release and mean AoA is more compact in [Leedham Elvidge et al., 2018], though they include a noticeable spread of variability.

5.4 Conclusion

This chapter provided an investigation of the transport and depletion diagnostics in the chemPul-2000 simulation, that are the transit time distributions of inert and chemical depleted tracers and the transit time dependent lifetime and the fractional release. Along with this, the according technical implementation and the theoretical concepts could be tested.

First, the implementation of the transit time distributions for the considered ODS and N_2O was tested. The results proofed that the resolution and sampling are suitable to provide valuable results. Next, the path integrated lifetime was investigated. It could be seen, how the path integrated lifetime that quantifies the combined effect of transport and depletion relates to measures of transport alone such as the mean AoA and the width of the age spectrum. Further, it was shown, that the path integrated lifetime might be a suitable approximation to estimate mixing ratios across most of the stratosphere, but not in the extratropical LS, as the transit time dependent lifetime stretches several orders of magnitude, probably due to the importance of mixing in that area which leads to broad age spectra. Thus, the projection by [Schoeberl et al., 2005] could be implemented for tracers with variable depletion in a CCM for the first time.

In the future it would be of interest to approximate the transit time dependent lifetime $\tau(t)$. As photolysis is an important depletion process across all considered species, it could be approximated as a Poisson process. This might lead to fruitful approximations of $\tau(t)$ by the probability distribution that consider the local photolysis rates and the mean AoA.

Further, it could be seen, that the transport time distribution of chemical depleted substances is a valuable tool to analyze the propagation of those tracers. The methodical improvements to tracer projections for EESC by considering the release time distribution instead of the age spectrum in [Engel et al., 2018] could be confirmed in a full three dimensional model. Compared to both, [Engel et al., 2018, Leedham Elvidge et al., 2018] EMAC provides larger fractional release values than their estimates. Though, this cannot be attributed to a distinct cause. To do so, the influence of the approximations for lifetime and mean AoA for the measurements need to be investigated, but also the representation of transport and chemistry and the boundary conditions in EMAC.

Chapter 6

Impact of changing climate on transport time distributions

This chapter is focused on the effects of a changing climate on the projection of tracers and their products. First, the future changes in dynamics will be considered. Next, the changes of tracers and their diagnostics (release time distribution, mean fractional release,...) will be studied. As the transport changes, potential impacts on chemical depletion could be, that for example tracers might be transported faster to the predominant loss regions or have longer residence times in those regions. To facilitate the attribution of transport and depletion changes, the transport time distributions and the respective measures will be used. To conclude the chapter, the focus will come back to consider changes in tracer projections due to the aforementioned changes.

6.1 Changes in dynamics

Before discussing the effect of changing climate on the transport of the tracers and their resulting depletion along the path, the changes in the common dynamical features between the 2000 and 2050 simulation shall be presented.

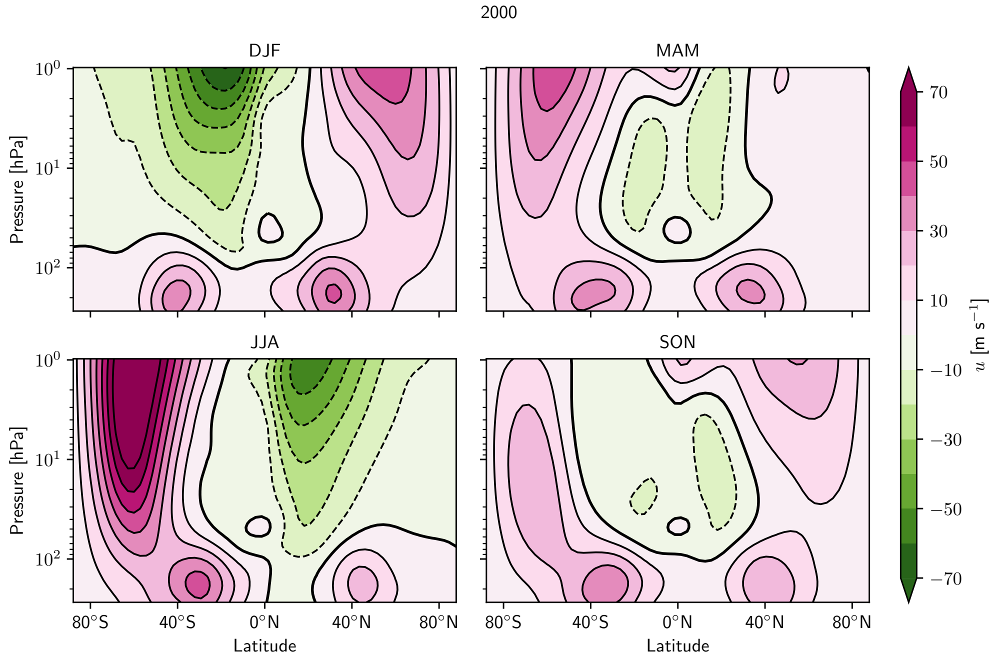

Figure 6.1: Seasonal mean zonal mean zonal wind u for the 2000 conditions simulation.

The results are in alignment to what is expected for EMAC from previous work, as for example [Oberländer-Hayn et al., 2015]. Still, they are shown here for the specific discussion of the chemPul simulations.

The polar vortices are considered as one major dynamical feature of the atmosphere. They are relevant as they pose a barrier against transport by horizontal mixing and isolate the polar air. Thus, Fig. 6.1 shows the seasonal mean zonal mean zonal wind u for the chemPul-2000 simulation. In DJF the NH polar vortex is at its peak, the SH polar vortex reaches its maximum in JJA.

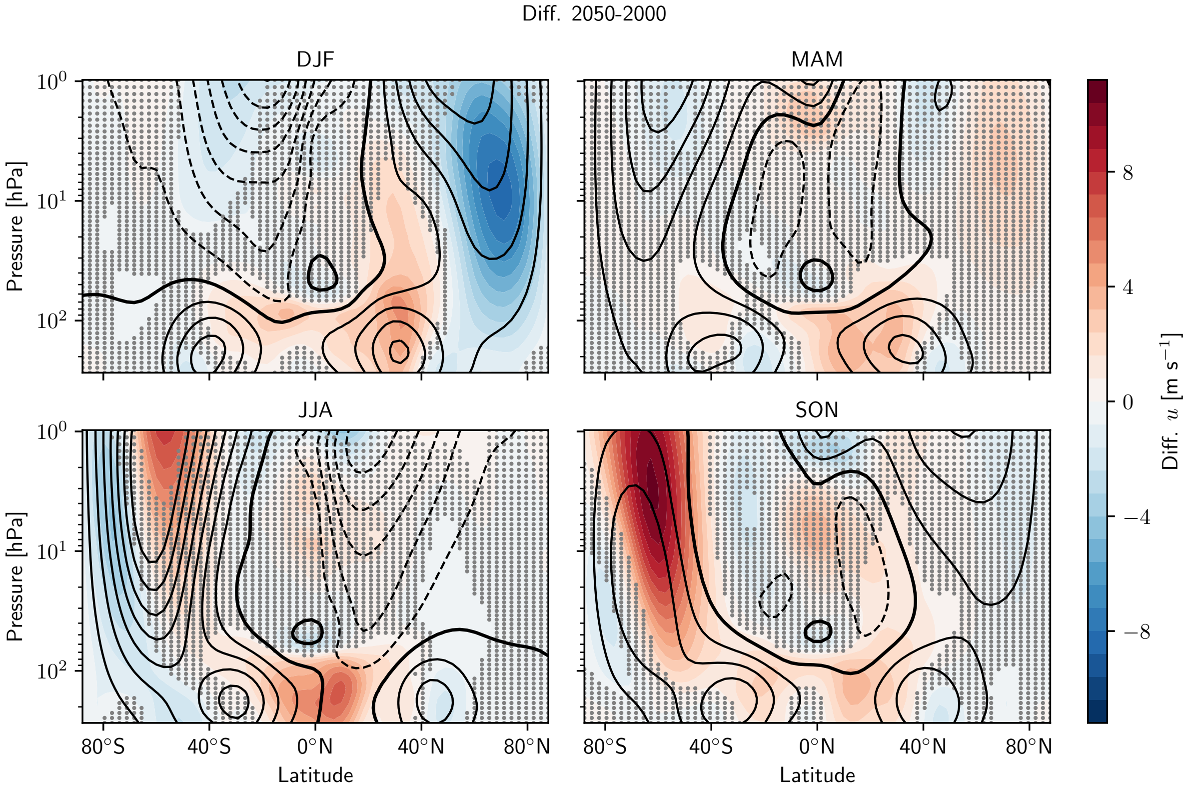

Figure 6.2: Zonal wind u seasonal mean difference of the 2000 and 2050 conditions simulation. The black contours indicate the 2000 conditions seasonal mean u. The gray stippling denotes insignificance of the change on the 95% probability level.

Fig. 6.2 presents the changes of u between the chemPul-2000 and chemPul-2050 simulation. Gray stippling was added to indicate where the change is significant and where not on the 95% probability level. It can be seen, that in the NH winter DJF, the polar vortex becomes weaker in the chemPul-2050 simulation. This is in accordance to what has been reported for several climate models [Manzini et al., 2014]. In contrast, the polar vortex in SH winter JJA becomes stronger. In addition in SON, u is still stronger in the SH. This suggests that the SH polar vortex takes longer to break down in 2050 than in 2000. Hence, the polar air masses are stronger isolated for an extended amount of time. This is in accordance to what [Ceppi and Shepherd, 2019] documented. Thus, considering the different development of the southern and northern polar vortex, opposing results in the measures such as AoA, $\bar{\tau}$ and arrival time in the NH and SH respective winter might be a consequence.

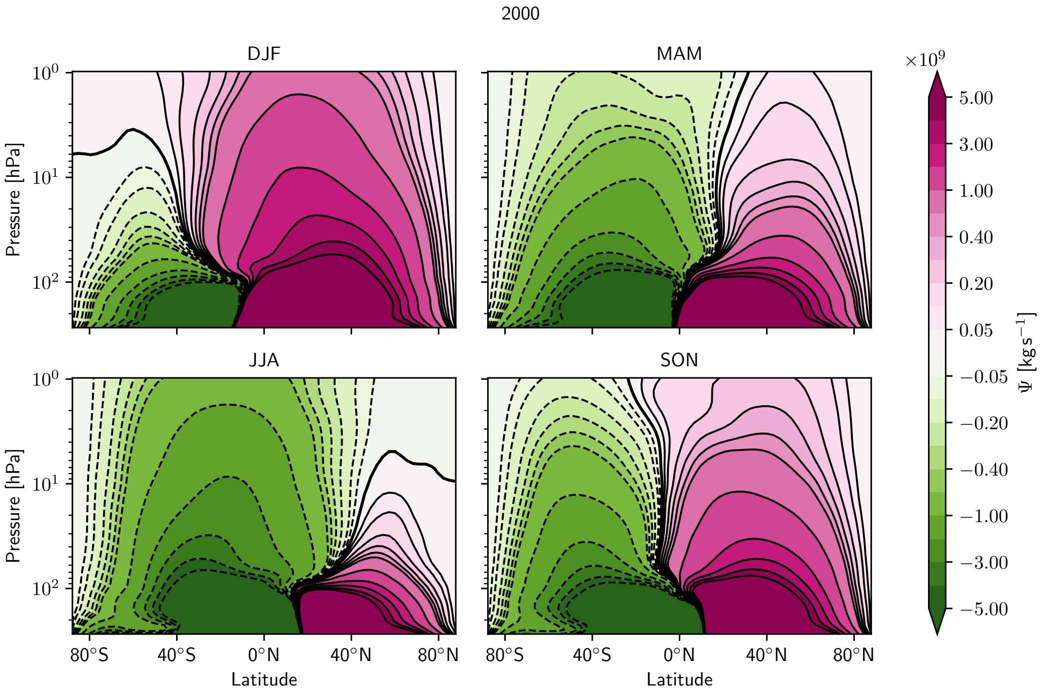

Figure 6.3: Seasonal mean streamfunction Ψ^* for the 2000 conditions simulation.

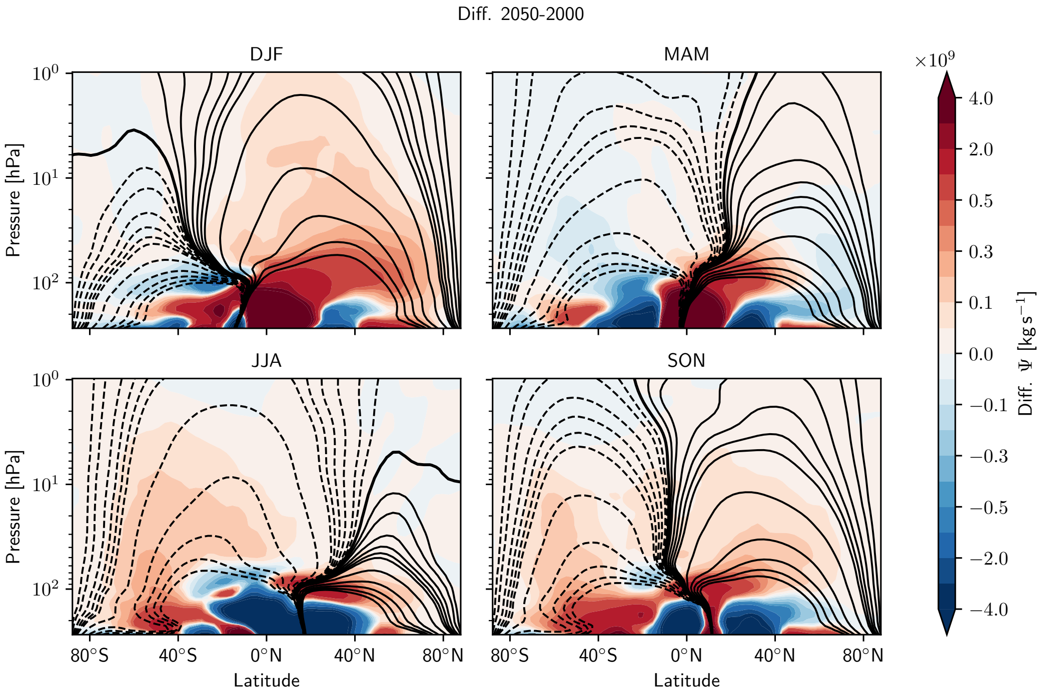

Figure 6.4: Seasonal mean difference 2050-2000 of the streamfunction Ψ^* for the chemPul simulations. The black contours indicate the 2000 conditions seasonal mean Ψ^*.

Aside from the zonal wind, the mass weighted streamfunction Ψ^* is considered here as a representation of the residual circulation which describes the dynamical situation of the atmosphere. Ψ^* is calculated as the integral of the latitudinal wind components v^* with regards to the pressure p (Eq. 2.1). Fig. 6.3 presents the seasonal mean streamfunction for the chemPul-2000 simulation. The slight seasonal shifting of the shallow branch of the BDC can be recognized. Further, the seasonal reversal of the deep branch of the BDC is very prominent.

Fig. 6.4 shows the seasonal mean difference in Ψ^* between both chemPul simulations. The shallow branch of the BDC shows a strengthening throughout the year. Though in SH SON (and JJA) the strengthening is rather weak. The deep branch strengthens in NH during SON to DJF, but weakens in the SH in JJA to SON. The changes of the deep branch are consistent with the polar vortex weakening in NH and strengthening in SH. Asides, if considering the SH deep branch weakening in the SH as comparing low and high ODS situations, this is consistent to [Abalos et al., 2019].

6.2 Comparison of representative N_2O and ODS of 2000 and 2050

The transient boundary condition mixing ratios of the trace gases are given in Fig. 6.5. For the chemPul simulations calculating the arrival time distributions, the respective year 2000 and 2050 values were prescribed. All tracer mixing ratios vary only slightly seasonally for the according years.

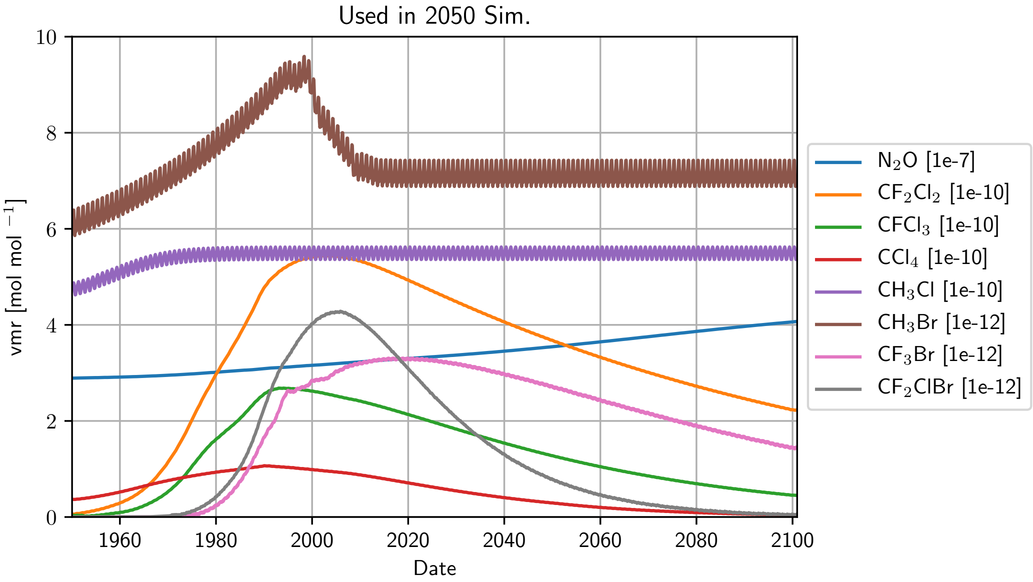

Figure 6.5: Transient time series of the boundary condition mixing ratios of the respective species (legend). The year 2000 and 2050 values are used in the according chemPul simulation. Respective scaling of the mixing ratios is given in the legend.

The exact 2000 and 2050 annual mean boundary condition mixing ratios for all considered species are given in Table 6.1.

Table 6.1: Boundary condition mixing ratios of the respective species prescribed in chemPul simulations. Given are the annual mean values.

Species	2000	2050	[mol mol^{-1}]
N_2O	3.16	3.55	10^{-7}
CF_2Cl_2	5.42	3.66	10^{-10}
$CFCl_3$	2.62	1.26	10^{-10}
CCl_4	9.83	2.88	10^{-11}
CH_3Cl	5.45	5.50	10^{-10}
CH_3Br	8.82	7.12	10^{-12}
CF_3Br	2.82	2.70	10^{-12}
CF_2ClBr	4.11	0.76	10^{-12}

Different assumptions contribute to the scenario for 2050 mixing ratios. For example, the amount of N_2O is higher in 2050 than in 2000 due to continuous emissions. Overall, ODS mixing ratios are decreasing due to political action. However, the mixing ratio of CH_3Cl remains roughly the same, as it has biogenic sources. In contrast, CH_3Br is assumed to decrease relative to its maximum, though it also has biogenic sources. CF_3Br has almost the same mixing ratio in 2000 as in 2050, as the maximum of the scenario is not around the year 2000, as for most ODS, but later around the year 2020, as can be understood from Fig. 6.5.

As can be seen from Fig. 6.6 and 6.7, the relative change of the abundance of a species is not the same throughout the atmosphere between the 2000 and 2050 scenario. Due to the simulated dynamics and depletion, regions can be determined that show a smaller or larger relative change than due to the prescribed boundary conditions alone. In the case of N_2O, given in Fig. 6.6, the relative change in boundary condition mixing ratio is positive, indicated by the black contour. Separated by season, the relative change in mixing ratio of the two simulations is predominantly positive (colors). For most of the stratosphere, the relative increase in N_2O is stronger than the increase in boundary conditions. Though some regions can be identified, which show a smaller increase or even a decrease in mixing ratios. Still, it should be kept in mind, that the upper stratosphere overall has a small abundance of the trace gas species and the prescribe depletion becomes less accurate, depending on the lifetime. Besides, relative change is not well suited as a description for those small mixing ratios. Therefore, it is more interesting what determines the deviations that are located lower in the stratosphere.

In the case of CF_2Cl_2, whose boundary condition mixing ratio has a relative decrease (Fig. 6.7), the patterns of smaller or larger decrease are very similar to those of N_2O. The only exception to this is a small feature of stronger decrease up in the ML stratosphere in SON. But as explained previously, features in the upper stratosphere might rather be artifacts than physical or chemical processes.

To make clear, which regions are specifically meant in the different seasons here and in the next sections, a simple overview plot is given in Fig. 6.8. LMS means the lowermost stratosphere, which is given by the difference in height of the troposphere in the tropics and the extratropics. To sum up the different regions of smaller relative mixing ratio change of Fig. 6.6 and 6.7 that will be considered in the next sections, those are DJF NH ML, DJF NH LMS, MAM

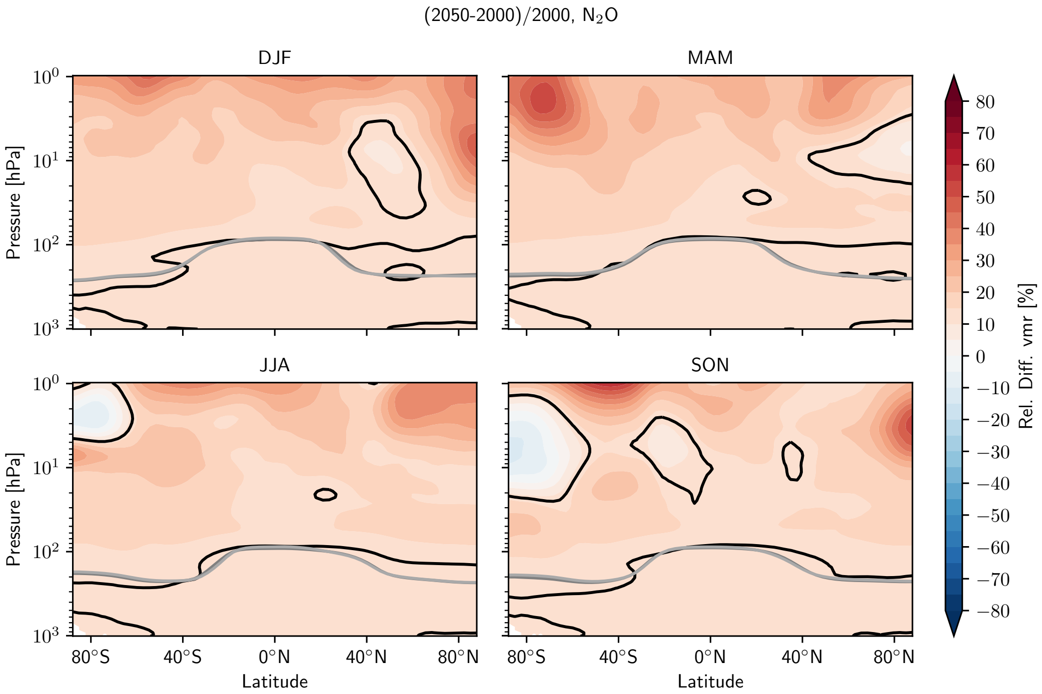

Figure 6.6: Relative change in mixing ratio for N_2O between 2000 and 2050. The black contours indicate the value of relative change in the boundary condition mixing ratio which is 12.5%.

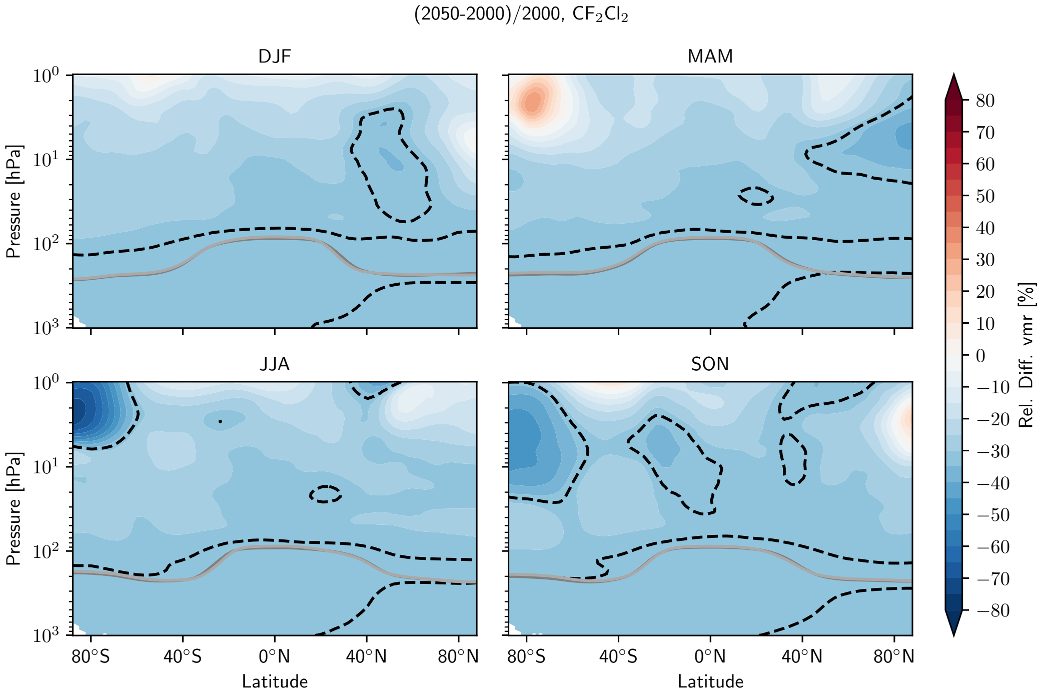

Figure 6.7: Relative change in mixing ratio for CF_2Cl_2 between 2000 and 2050. The black contours indicate the value of relative change in the boundary condition mixing ratio which is -32.5%.

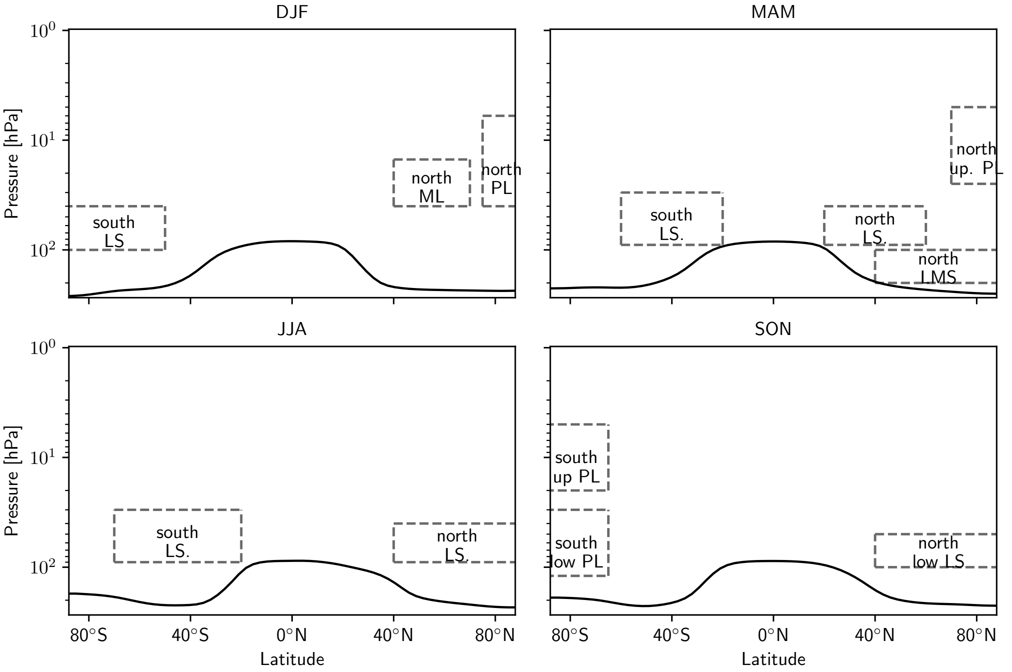

Figure 6.8: Overview plot to clarify regions for the upcoming discussions.

NH LMS, MAM NH polar region, SON SH polar region and SON tropical pipe edges. The mentioned regions can be found in slight variation for all considered ODS and N_2O, as high up as possible considering their lifetime. That means, shorter lived ODS cannot show patterns of change in the upper (and middle) stratosphere, as they do not reach as high up.

To make it more specific that the relative changes in tracer abundance high up are not as relevant, the seasonal average absolute change of N_2O mixing ratio between the two simulations is show in Fig. 6.9). The absolute differences high up in the stratosphere are very small as the mixing ratios are small in the first place. Most of the change in mixing ratio between 2000 and 2050 occurs in the lower stratosphere. The region in the MAM northern LMS also becomes apparent in Fig. 6.9 that could already be identified as a region of interest from Fig. 6.6, as it shows a smaller increase in mixing ratio, .

The interesting question to investigate now is how the changes in mixing ration are determined by changes in chemical processes and transport. In addition, as already expressed in Sec. 2.3.2 and 5.2, the chemical depletion is spatially dependent, such that changing transport of trace gases is also connected to changes in their chemical depletion.

To address this question, first, the chemical loss of the investigated species is presented as it is diagnosed during model runtime. Both the relative loss and the absolute loss are available. When considering whether to compare relative or absolute loss of the 2000 and 2050 simulation, it should be kept in mind, that the absolute loss should show a difference simply due to the different abundances, while the relative loss is not expected to show strong differences, as photolysis rates, which is the predominate or even only loss source of all considered species, are expected to simply scale with abundance.

Fig. 6.10 shows the monthly averaged relative loss of N_2O from the chemPul-2000 simulation. Overshooting loss can be seen at some grid points relative to the surrounding loss

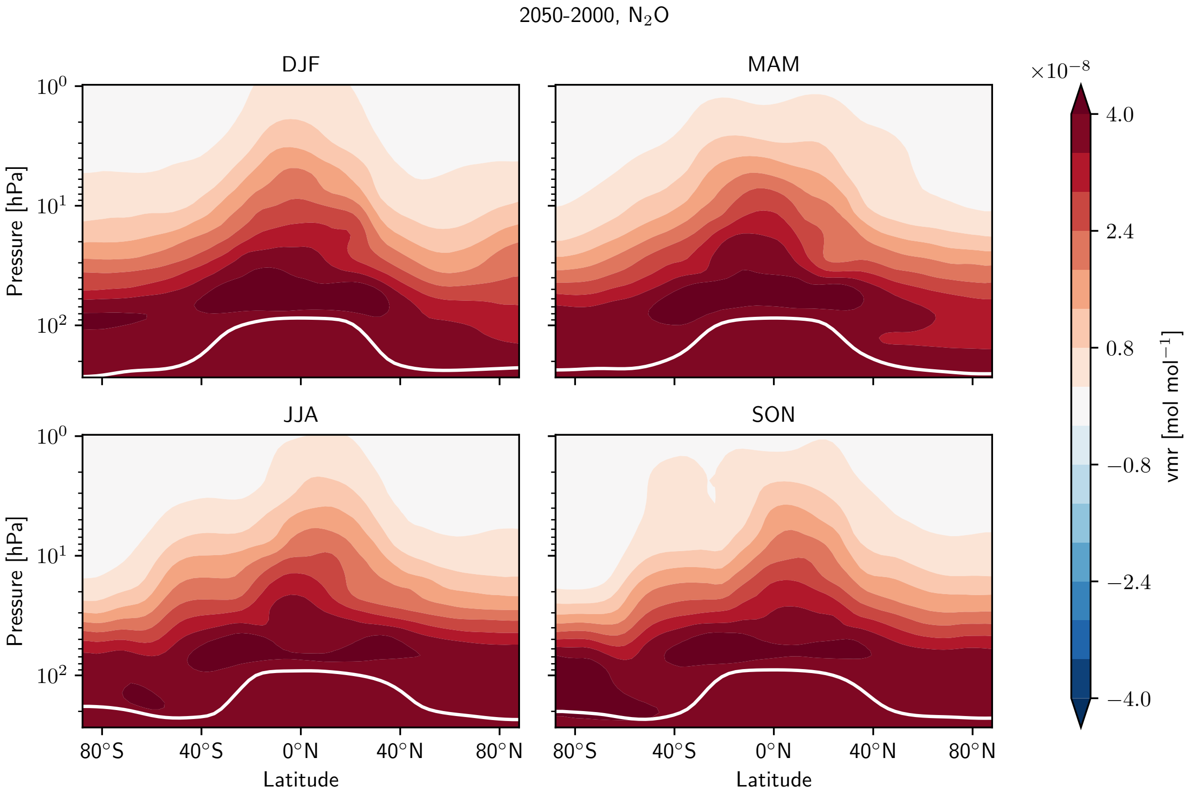

Figure 6.9: Absolute change in mixing ratio for N_2O between 2000 and 2050.

during the polar night in both vortices. In addition, extended parts of those regions cannot be computed due to numerical reasons. Both occurs predominantly in the polar night, when no photolysis happens and the tendency of the cumulated loss is supposed to be zero. All of the considered trace species show those overshoots as they are all subject to photolysis. Those effects are clearly numerical model fluctuations. Apart from those artifacts it can be recognized, that very little depletion occurs in the polar night regions. Therefore, the numerical effects are not expected to have a strong impact. The remainder of the atmosphere looks as anticipated from other work, e.g. [Ko et al., 2013], and general understanding, with relative loss increasing with altitude as less photons were absorbed and are still available for photolysis.

Now, Fig. 6.11 shows the difference in relative loss of N_2O from the chemPul-2000 and chemPul-2050 simulations. The relative loss is almost the same in both simulations, apart from some artifacts at single grid points where the relative loss implementation, as described in Sec. 3.2, led to artifacts already in the simulations that are compared. The use of a logarithmic colorbar in Fig. 6.11 should enable to see differences if there were any. Though again, seeing a strong change in the relative loss is not anticipated.

The differences in absolute loss are not shown here. For the species with strong relative changes in boundary conditions between 2000 and 2050, i.e.

- CF_2Cl_2 (-32%),
- $CFCl_3$ (-60%),

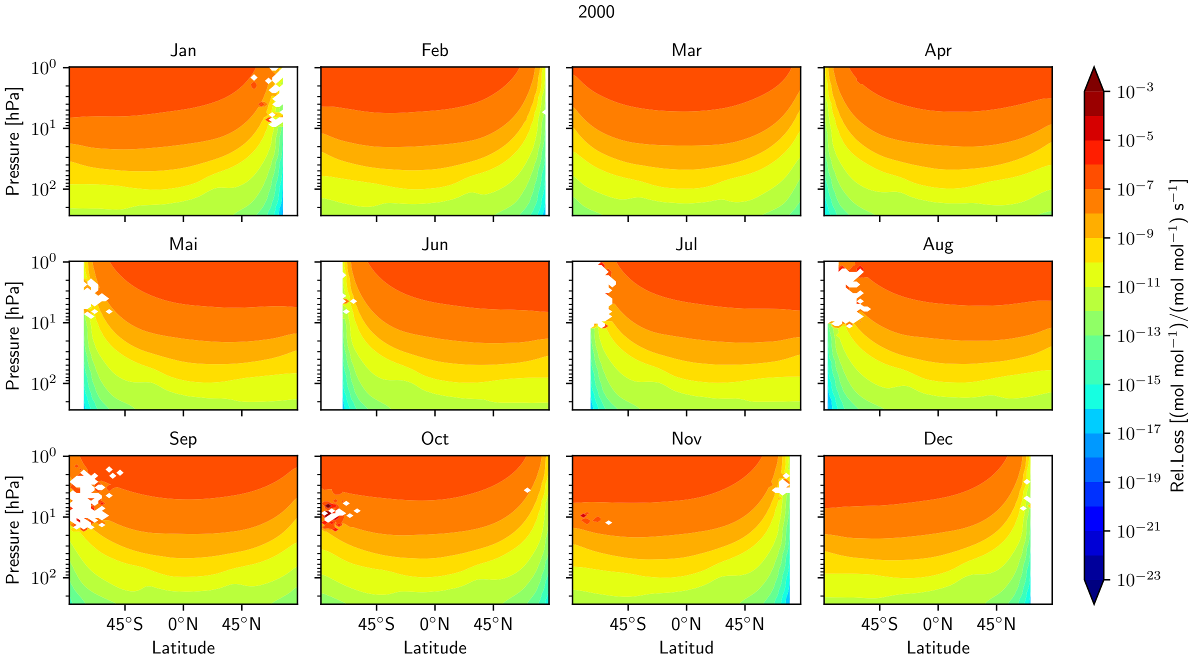

Figure 6.10: Monthly average relative loss of N_2O from the chemPul-2000 simulation in $(\text{mol mol}^{-1})/(\text{mol mol}^{-1})\text{s}^{-1}$.

- CCl_4 (-71%)
- and CF_2ClBr (-82%),

they are dominated by the changes in total abundance of the different species resulting in decreased loss accordingly. For the other species with smaller relative change in boundary conditions, i.e.

- N_2O (12%),
- CH_3Cl (-1%),
- CH_3Br (-4%)
- and CF_3Br (-4%),

regions of change in absolute loss along and opposite the predominant change of boundary emissions are found. Still, those changes show an combined effect of chemical depletion and transport. For example, even if overall N_2O increases in 2050, there are still regions where the overall loss decreases as less N_2O arrives there than in 2000 as the relative change in boundary condition is not as large. Most of changes opposite the predominant change remain relatively small. In addition, an anomalous change in the absolute loss cannot be linked directly to the relative changes in mixing ratio (e.g. Fig. 6.6 for N_2O) as a smaller absolute loss, might be linked to both, less of the species being present and therefore less loss or less of the species being depleted as there is less loss resulting in more of the species being present.

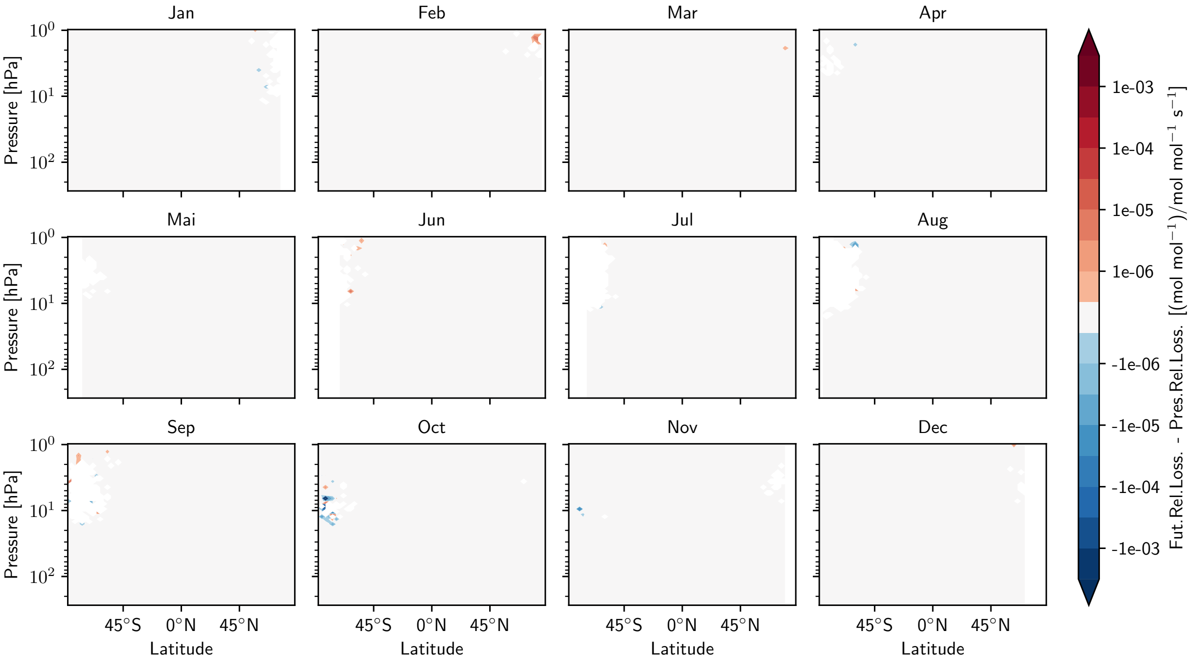

Figure 6.11: Difference of relative loss of N_2O 2050-2000.

Thus, it can be concluded, that the chemical depletion of the different species in itself is not the predominant influence on the changes in tracer mixing ratio presented in the previous Sec. 6.2, but rather the change in transport or the interplay of transport and chemical depletion determine the changes.

6.3 Changes in transport and depletion diagnostics

As age spectra and arrival time distribution are implemented as diagnostics, those shall be used to shed light on physical and chemical processes determining the changes between both chemPul simulations in mixing ratios of the investigated species. Therefore, Fig. 6.12 shows the change in mean AoA Γ derived from the age spectra for every month. The black contours give the relative change in mixing ratio of N_2O equal to the relative change in boundary condition, similar to Fig. 6.6. Predominantly, the mean AoA decreases in 2050 as expected from the strengthening of the BDC. Remembering Fig. 6.4, the deep branch of the BDC becomes weaker in JJA. Still, here we see a decrease in AoA. Therefore the decrease in AoA in JJA has to originate from other factors such as the increasing strength of the shallow branch and of upwelling in other seasons.

An increase in mean age Γ can be seen in the northern LMS in MAM in 2050. Similarly, the southern polar vortex shows an increase in mean AoA in October. As was already clear from Fig. 6.2, the southern polar vortex breaks down later in the 2050 simulation. This means, that the relatively old air inside the vortex (compare Fig.5.1) remains isolated for an extended time and thus leads to older air in October in the 2050 scenario. In addition, this increase in mean AoA in SH polar SON is consistent to the results by[Morgenstern et al., 2018, Li et al., 2018]. Furthermore, it can be noted, that right above the tropopause the change in mean AoA

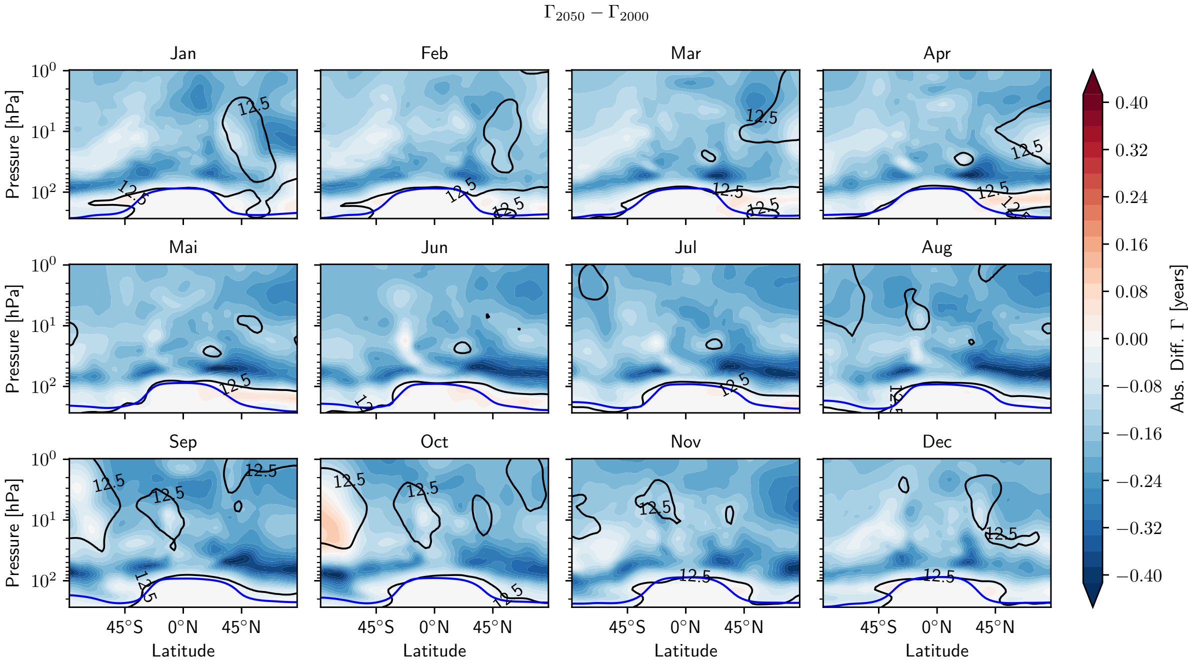

Figure 6.12: Absolute difference Γ derived from age spectra between 2050 and 2000. The black contours show the relative change in mixing ratio of N_2O of the same % value as the boundary condition, as already given in Fig 6.6.

is very small which is most visible in DJF and MAM, though in general AoA is very small. Above that (ca. 100 hPa) a region is present with the strongest decrease in mean AoA in 2050, specifically in the extratropics. This decrease is even stronger in the NH. This strong decrease is indicative of the stronger shallow branch of the BDC. Further, considering [Eichinger et al., 2019], changes in mixing might contribute to this decrease.

Bearing in mind Fig. 6.6 and 6.7, the regions with relatively low changes in vmr correspond to those of positive or small negative age differences here while the regions with relatively strong changes in mixing ratio correspond to stronger decrease in mean AoA (still, not over interpreting the uppermost stratosphere). The black contours of the relative vmr change are given as a reference for this statement. Though, this statement remains rather vague in the case of the DJF NH ML, the DJF NH LMS and the MAM NH polar region decrease in mixing ratio. Those regions can only be described as smaller changes in AoA compared to their imminent surroundings.

Similar regions of change in mean AoA could be obtained from the linear AoA tracer (not shown here). Thus, they are expected to correspond to physical processes and are not e.g. artifacts due to sampling biases.

To closer discuss how the change in mean AoA might describe the changes in tracer mixing ratios, the fractions of old air of the age spectrum will be discussed. The chosen limits for the fractions highlight different regions depending on the predominate mean AoA value.

First, Fig. 6.13 shows the change between the chemPul simulations in fraction of air younger than 0.5 years seasonally and Fig. 6.14 the change in fraction of air older than 2 years. This selection of limits is particular insightful for the lower stratosphere. In Fig. 6.13 the increase in

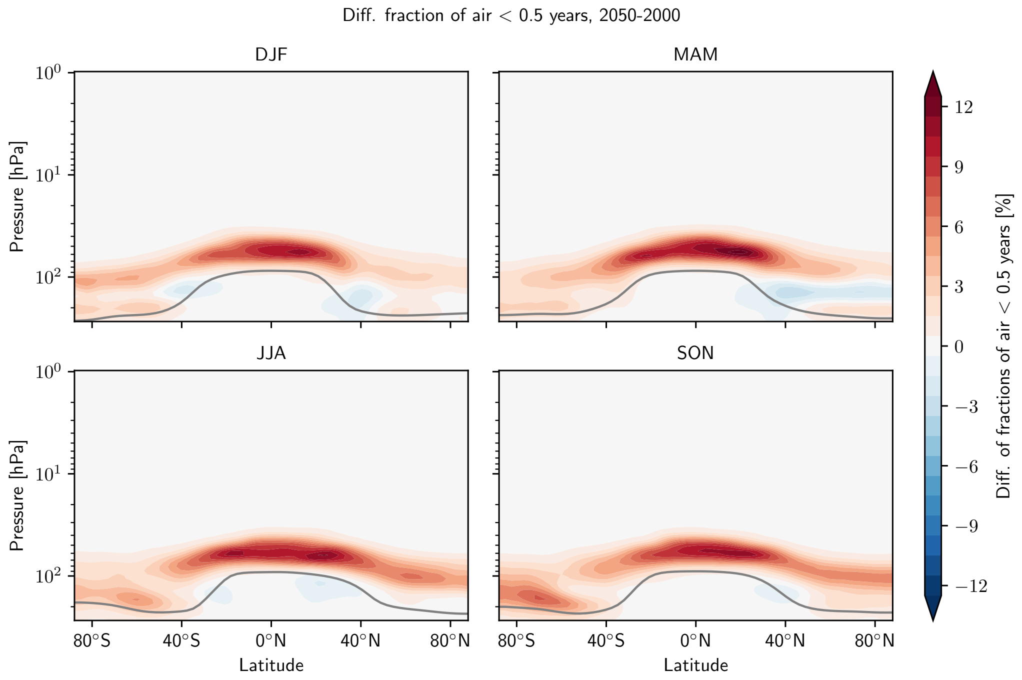

Figure 6.13: Change between 2000 and 2050 in fraction of air younger than 0.5 years determined from the age spectra.

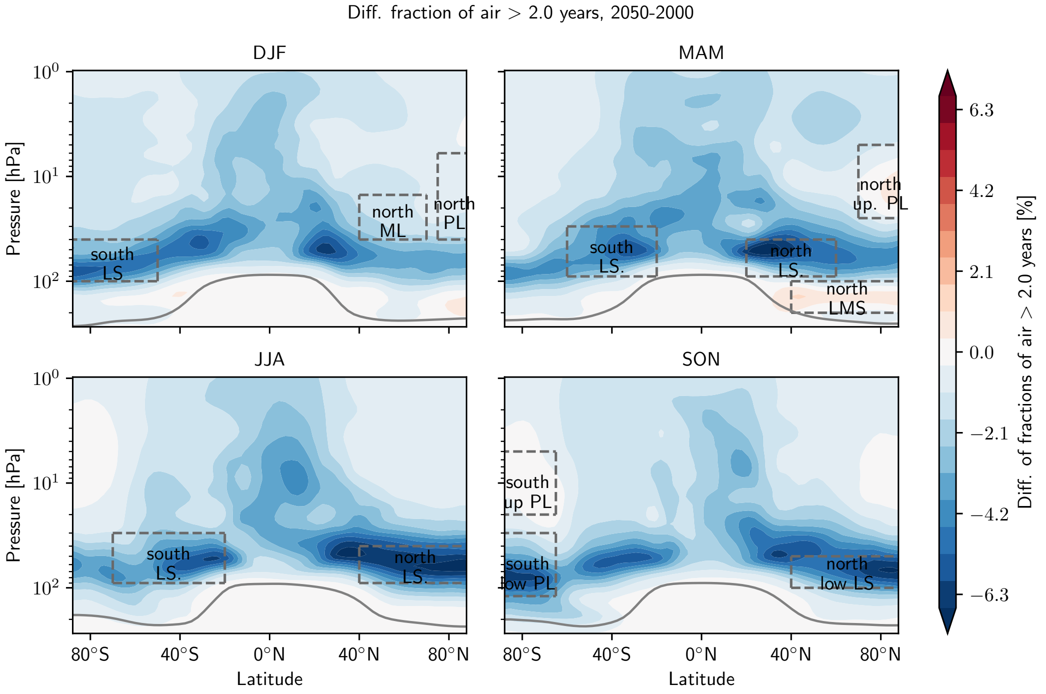

Figure 6.14: Change between 2000 and 2050 in fraction of air older than 2 years determined from the age spectra.

fraction of air younger than 0.5 years along the tropopause up to 80 hPa in the extratropics and 40 hPa in the tropics is visible for all seasons. The strongest increase is in the tropics corresponding to increased tropical upwelling. The clear exception to the increase is the already familiar MAM NH LMS, which shows a decrease in air younger than 0.5 years.

Fig. 6.14 shows the decrease in air older than 2 years for most of the stratosphere. The decrease is particular strong in the extratropical lower stratosphere. The only regions of slight increase or no decrease of air older that 2 years are the MAM NH LMS, MAM NH polar region and the SON SH polar region (the latter not visible on the color scale). The first two exceptions were already anticipated from the changes in mean AoA. The NH polar region in MAM was not as clear in the change in mean AoA, but from the fraction of old air it becomes clear, that there is a change in partitioning of the age spectrum different from the predominant change in partitioning in the stratosphere. Therefore for this region, too, part on the patterns in change in mixing ratios can be attributed to patterns in changes in the age spectra.

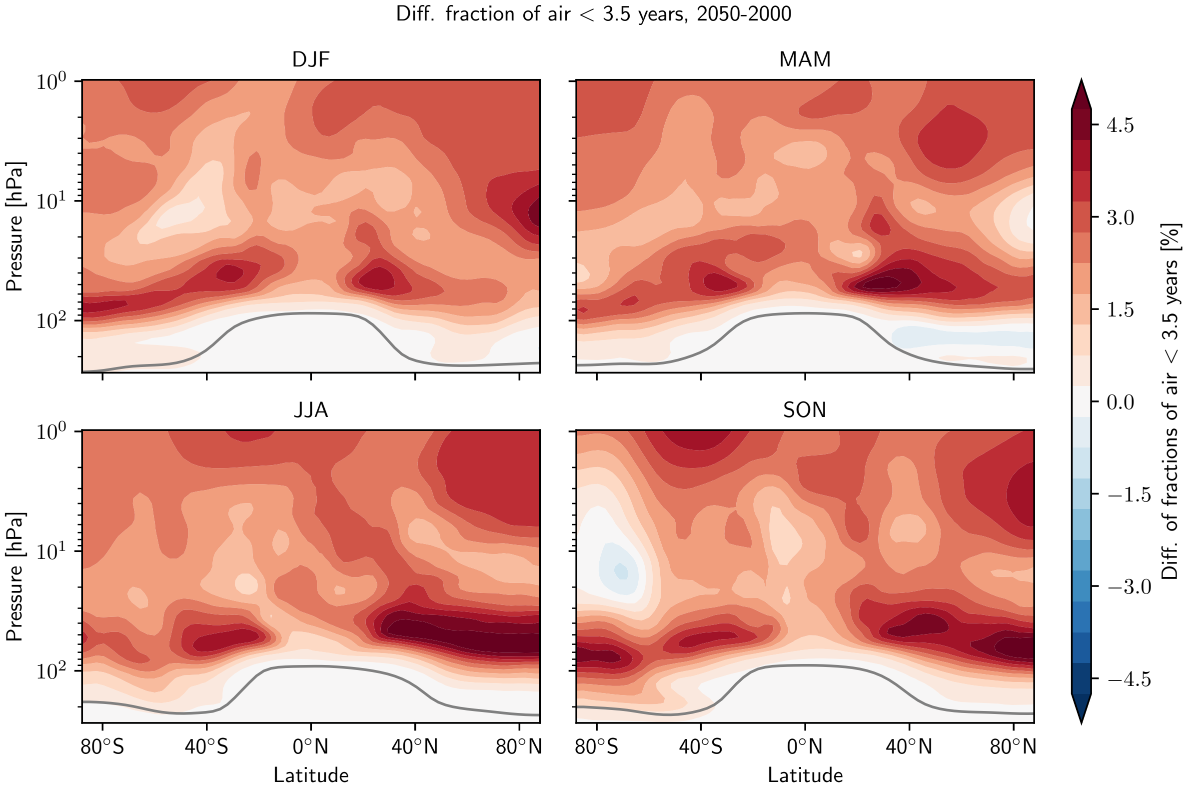

Figure 6.15: Change between 2000 and 2050 in fraction of air younger than 3.5 years determined from the age spectra.

In addition, the changes in fractions of air younger than 3.5 years and older than 5 years will be considered (Fig. 6.15 and 6.16). Those boundaries are particular useful to investigate the polar regions. Fig. 6.15 further illustrates the shift towards older air in 2050 for the MAM NH polar latitudes around 10 hPa and the SON SH polar regions, as those are the only regions that show an decrease in air younger than 3.5 years (SON SH), respectively close to no change (MAM NH). The change in fraction of air older than 5 years (Fig.6.16) shows the predominant shift towards younger age, and the shift towards older age for the MAM NH LMS and the SON

SH polar region.

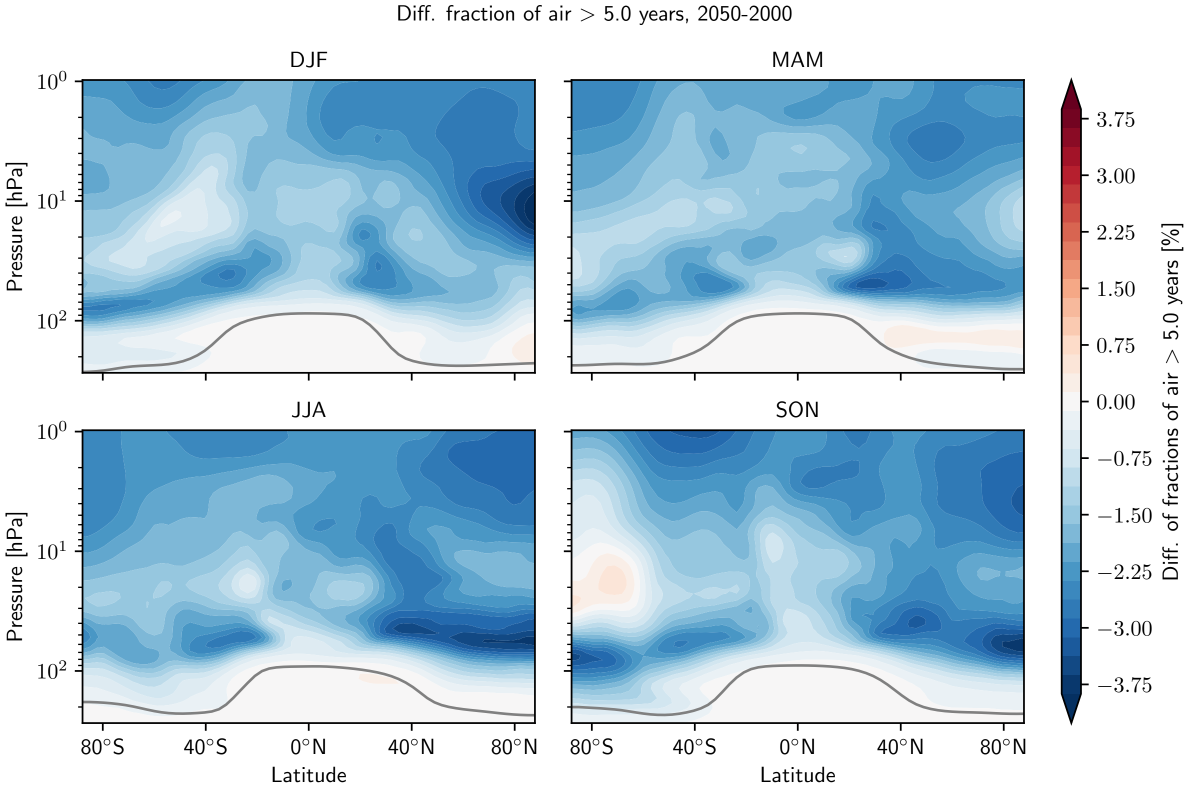

Figure 6.16: Change between 2000 and 2050 in fraction of air older than 5 years determined from the age spectra.

At this point, most of the patterns in the shifts in mixing ratio could be linked to changes in mean AoA and fractions of old and young air (excluding the upper stratosphere). One feature in mixing ratio change not covered by this explanation is that along the edges of the tropical pipe in SON. However, this region is subject to strong variability, as already shown in Fig. 3.3 and 5.3. Therefore, it is not to surprising, that this feature in the climatological mixing ratios cannot by attributed to AoA as a very simple explanation.

The other feature which is not well explained is the DJF NH ML feature. Though, the increase in young air is weaker than in the surroundings (See Fig.6.12). Thus, the feature does not fully contradict the hypothesis that most of the changes in mixing ratio can be linked to changes in dynamics visible in mean AoA, neither does it support it. It can be suggested, that as the polar vortex becomes weaker in 2050 than in 2000, the vortex air is less isolated. That would result in some of the already older, depleted vortex air leaving towards mid-latitudes. At the same time, some air from outside the vortex which is younger and less depleted could enter the vortex. This would result in a pattern that shows less relative mixing ratio change inside the vortex and and more relative mixing ratio change inside the vortex comparing 2000 and 2050.

Nevertheless, to further understand the patterns in change of vmr, the mean fractional release $\bar{f}$ and the path integrated lifetime $\bar{\tau}$ can be used which allows to further investigate the combined result of transport and chemical depletion. First, Fig. 6.17 presents the seasonal

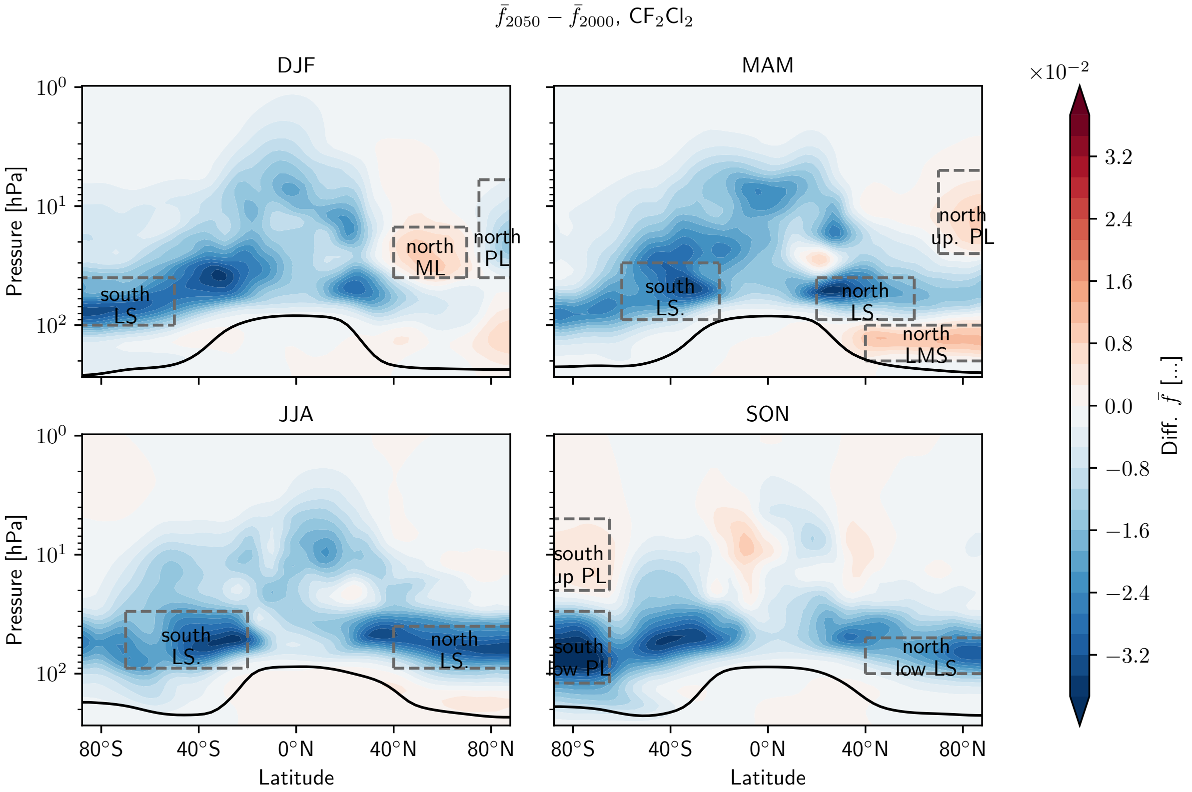

Figure 6.17: Difference in mean fractional release $\bar{f}$ of CF$_2$Cl$_2$ between 2000 and 2050.

change in mean fractional release between 2000 and 2050 for CF$_2$Cl$_2$. Please note, that as a fraction $\bar{f}$ does not have a unit but ranges from 0 to 1. The patterns in change of the mean fractional release are very similar for the different ODS. Again, this statement refers to as far as shorter lived ODS can spread through the atmosphere. No change in fractional release can be seen where the fractional release is already 1 in both simulations. For most of the atmosphere, the mean fractional release shows a decrease. This is anticipated, as already Fig. 6.6 showed more relative increase in mixing ratio, which corresponds to less of the initial species being released, which is described by a smaller $\bar{f}$. At the same time, regions that were already specified for less relative increase or even decrease in mixing ratios consistently present an increase in $\bar{f}$.

Next, the change in path integrated lifetime $\bar{\tau}$ will be considered. In that case, the investigated species fall in two groups, namely those with considerable tropospheric loss and those without. In the group with tropospheric loss are CH$_3$Cl, CH$_3$Br and CH$_3$CCl$_3$, though the latter is not considered for comparisons with 2050 as it is assumed to be no longer emitted. When looking at the path integrated lifetime directly, this group shows a small tropospheric lifetime. CF$_2$ClBr lies somewhat between both groups considering the strength of its tropospheric loss. The remaining trace gas species, i.e. N$_2$O, CF$_2$Cl$_2$, CFCl$_3$, CCl$_4$ and CF$_3$Br, do not show relevant tropospheric loss considering their overall loss patterns. Consequently, those species show a fairly large tropospheric $\bar{\tau}$.

As representation of the group with little tropospheric loss, Fig. 6.18 shows the relative change of the path integrated lifetime of CF$_2$Cl$_2$. As one would intuitively suggest, where the

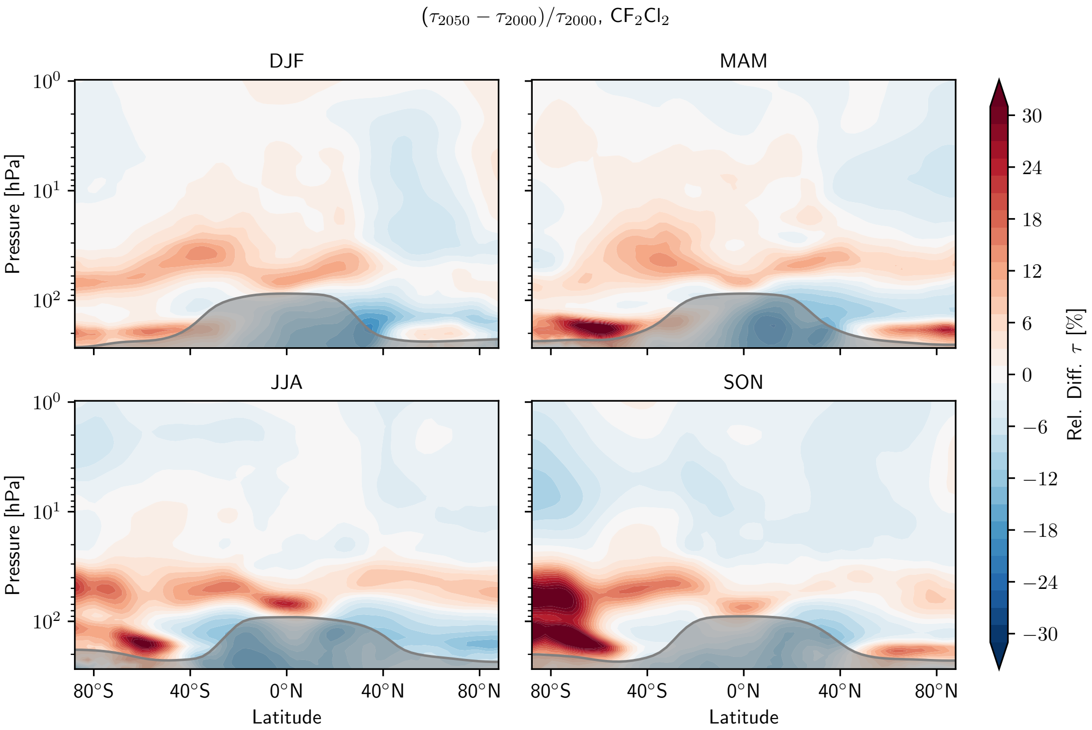

Figure 6.18: Relative change in % in path integrated lifetime $\bar{\tau}$ for CF_2Cl_2 between 2000 and 2050.

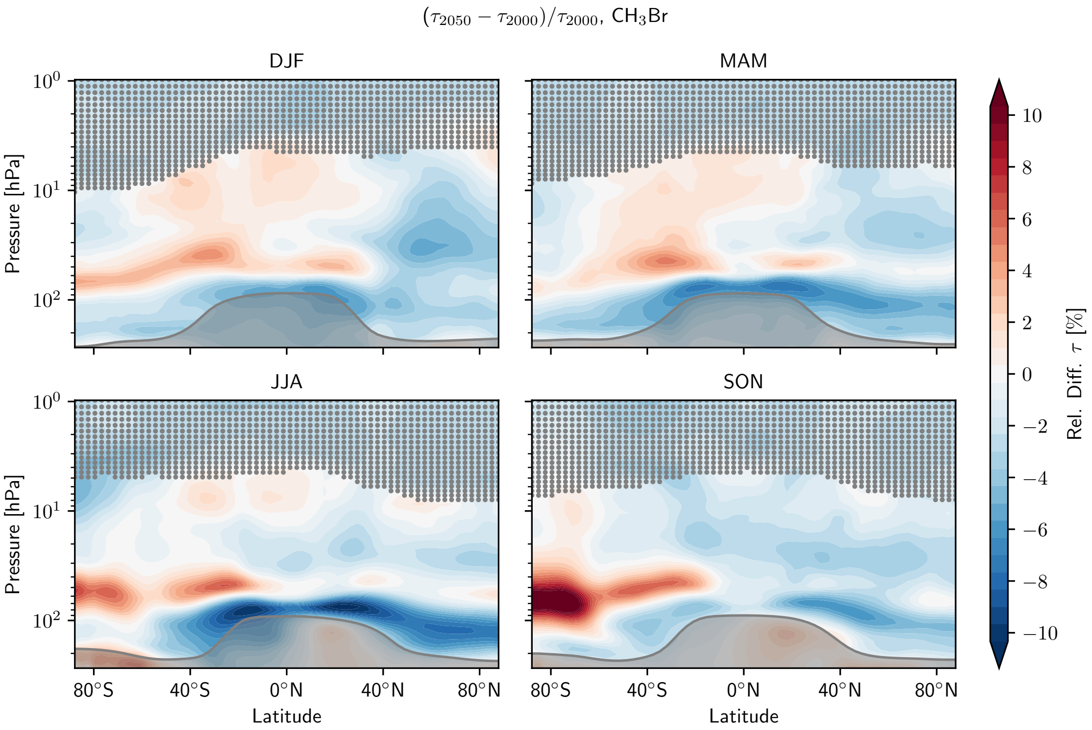

Figure 6.19: Relative change in % in path integrated lifetime $\bar{\tau}$ for CH_3Br between 2000 and 2050.

mean fractional release $\bar{f}$ of CF_2Cl_2 decreased in 2050, the path integrated lifetime increased and vice versa.

As representative of the group with tropospheric loss, Fig. 6.19 shows seasonal mean relative change the path integrated lifetime of CH_3Br. In the middle stratosphere, the patterns of the relative change of path integrated lifetime are similar to those of the other group. But in the lower/lowermost stratosphere an area of noticeable decrease in $\bar{\tau}$ in 2050 can be seen. This can be understood as the tropospheric sinks playing a stronger role probably due to enhanced stratosphere-troposphere exchange, considering studies suggest an increase in the future [Young et al., 2013, Kawase et al., 2011].

To better link the changes of path integrated lifetime and mean fractional release to the changes in the other transport distribution, the transport time distributions and transit time dependent fractional release and lifetime of the regions for the respective seasons were averaged. Those regions were already marked in Fig. 6.17. By the definition of those regions, Fig. 6.20 shows G, G^*, $G^\#$, $\tau(t)$ and $f(t)$ of CF_2Cl_2 for MAM NH LMS.

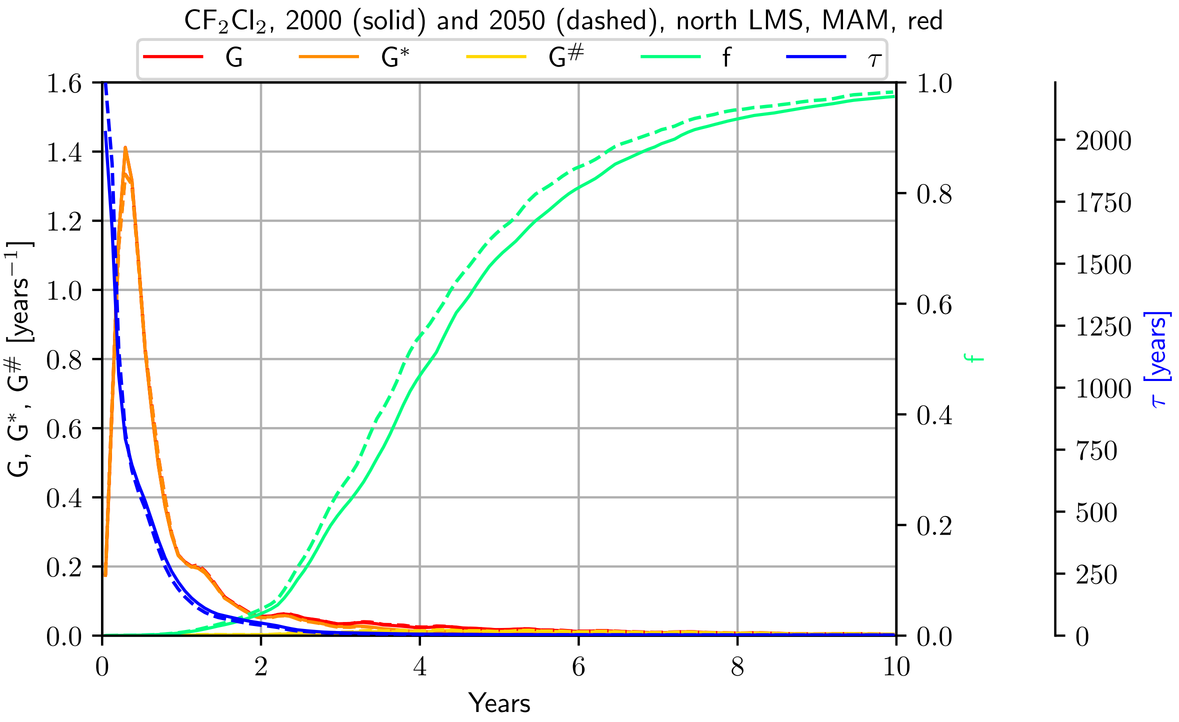

Figure 6.20: Transport distributions G, G^*, $G^\#$, $\tau(t)$ and $f(t)$ of CF_2Cl_2 (colors given in legend) in MAM in the NH LMS in 2000 (solid) and 2050 (dashed).

As the mean fractional release $\bar{f}$ can be described as the integral over the release time distribution $G^\#$, it can be seen for all regions, that $G^\#$ is lower in 2050 where $\bar{f}$ is lower and the other way around. For the transit time dependent fractional release $f(t)$ it is not as easily seen, how it relates to the changes in mean fractional release as the transit time dependent fractional release needs to be convoluted to obtain the mean fractional release. For most specifically considered regions, $f(t)$ is either roughly the same in 2000 and 2050 or in slightly higher in 2050, both for cases where the mean fractional release is higher or lower in

2050. What can be said for regions of the LS and the LMS is that age spectrum and arrival time distribution peak stronger, respectively earlier in cases, when $\bar{f}$ is lower in 2050 and the other way around. Expressed simplified that means, that as transport is faster (slower) there is less (more) time for chemical depletion. The other regions present distinct modes in the age spectra and arrival time distributions. Consequently, the shifts in those distributions are not as obvious, though the previous considerations of fractions of old and young air have already provided insight to this.

6.4 Relevance to mixing ratio projection

The discussion of the changes of path integrated lifetime $\bar{\tau}$ and mean fractional release $\bar{f}$ give rise to the question, whether those changes pose a relevant effect when discussing the transport and depletion of the trace gases. Assuming one had the correct $\bar{\tau}$ and G for the whole atmosphere for the year 2000 and wants to project the vmr in 2050, would the changes of $\bar{\tau}$ and G matter?

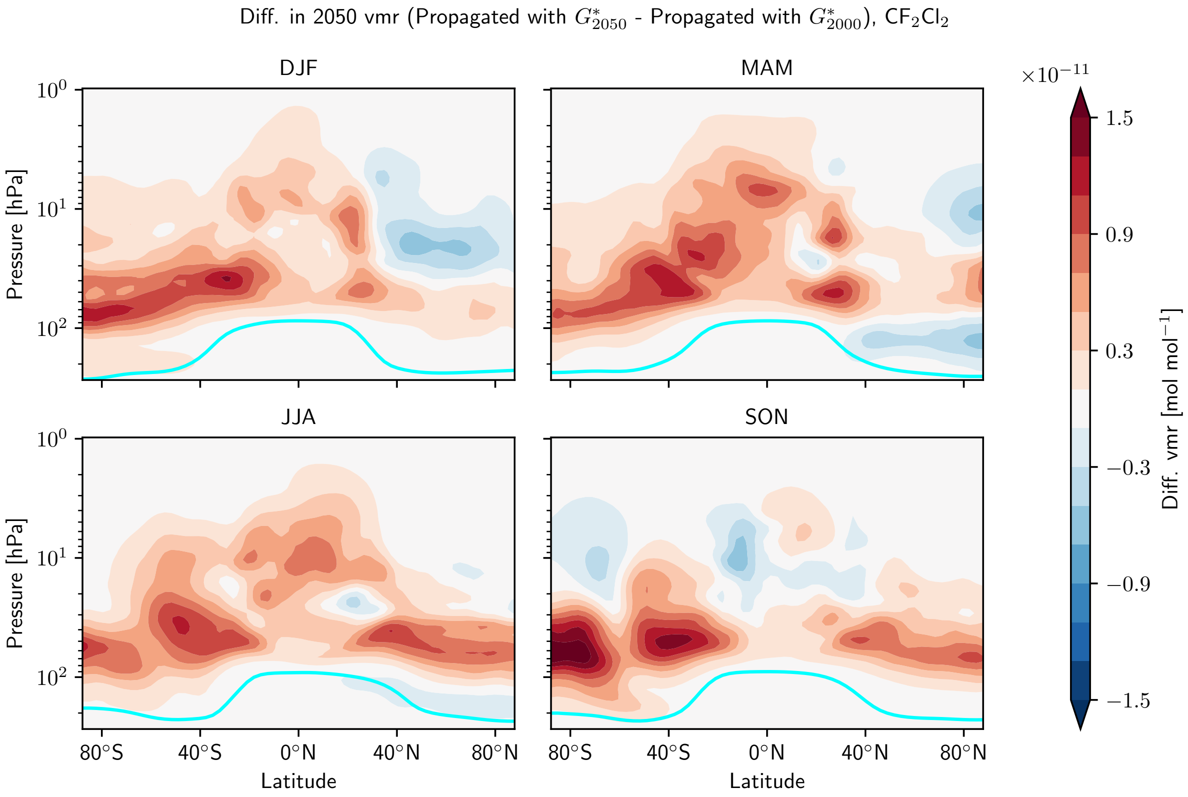

Figure 6.21: Difference of 2050 projected mixing ratio using G^*_{2000} and G^*_{2050} for CF_2Cl_2.

Fig. 6.21 considers exactly this question for the EMAC model world and shows the seasonal differences of CF_2Cl_2 mixing ratio projected from $G^*_{2000}(t)$ and $G^*_{2050}(t)$. This is equivalent to using age spectrum and transit time dependent lifetime. Here, G^* is considered instead of the path integrated lifetime with the age spectrum as this is even more accurate for projecting mixing ratios, as was already shown in Sec. 5.2, Fig. 5.11. Predominantly, it results in an underestimation of the mixing ratios when the changes in G^* are not considered. In the regions in the lower stratosphere where considerable tracer mixing ratio is present and most of the error of estimating occurs, the error in estimating the tracer mixing ratio reaches about 7.5%. The regions, which already showed changes opposite to the predominant change in the other diagnostics, can also be found in the differences of estimated mixing ratios. That means, that those regions are showing a decrease in estimated mixing ratio when applying G^*_{2050}.

To next consider the changes in projection of the product species, the resulting relative changes in the 2050 EESC estimates as of using the 2000 or 2050 release time distribution $G^\#$ are given in Fig. 6.22. As the organic fraction of the tracer tends to be underestimated (Fig. 6.21), when applying 2000 parameters, the respective products are mostly overestimated (Fig. 6.22). As EESC is already low in 2050, the largest change is in the lower stratosphere at about 15%. Overall, applying the 2050 parameters creates a picture in that the source species take more time to release the product species, seemingly leading to halogens being released for an extended amount of time.

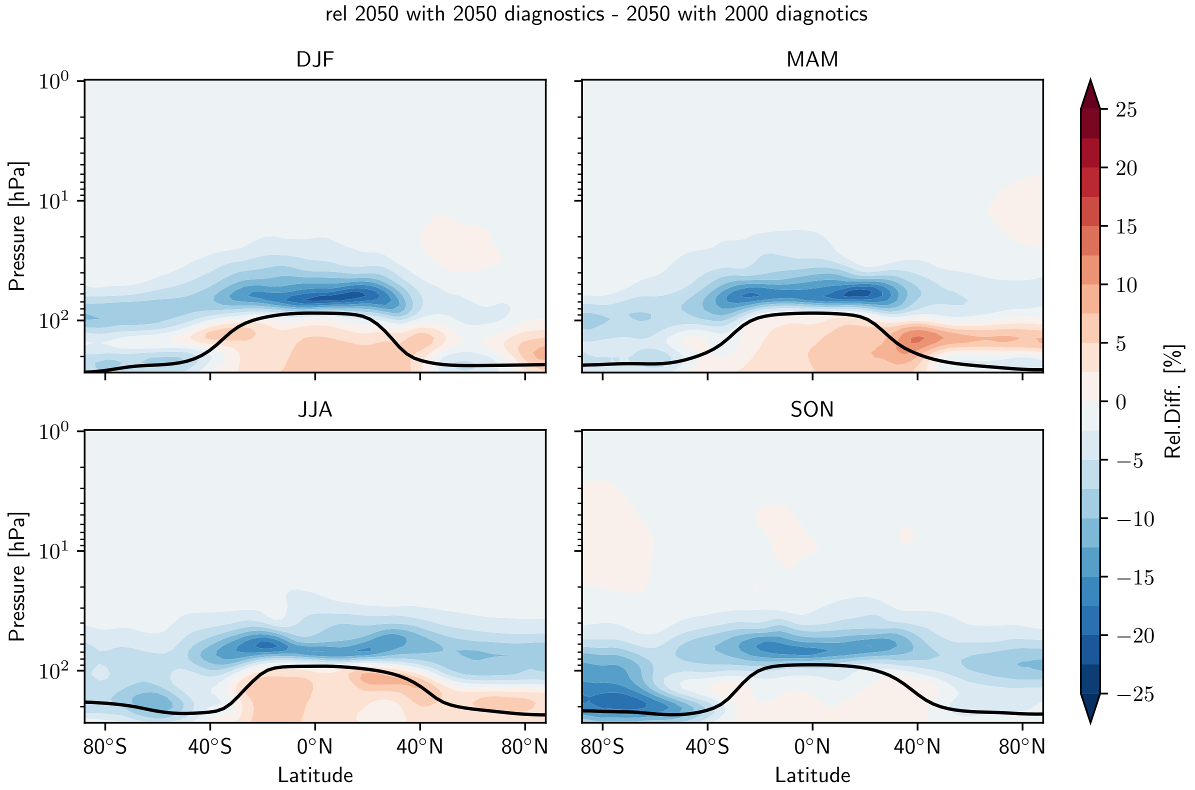

Figure 6.22: Difference of projected EESC using $G^\#_{2000}$ and $G^\#_{2050}$.

To be more specific, the example of EESC at $\Gamma = 3$ years from Fig. 5.12 is picked up again. Now, in Fig. 6.23 the EESC projection using the 2050 release time distribution at 60 hPa 40° N-60° N was added. As was already shown, $\bar{f}$ at this location is lower in 2050, meaning overall the resulting EESC is below the 2000 modeled EESC. The change in $\bar{f}$ is an approachable way of explaining the changes in EESC due to $G^\#$. Eq. 2.21 and 2.22 explained, how $\bar{f}$ can be exchanged in the EESC calculation. Rephrased, the previous statement means that $G^\#$ at this location tends to be lower and peak at later transit times in 2050, which contributes to the

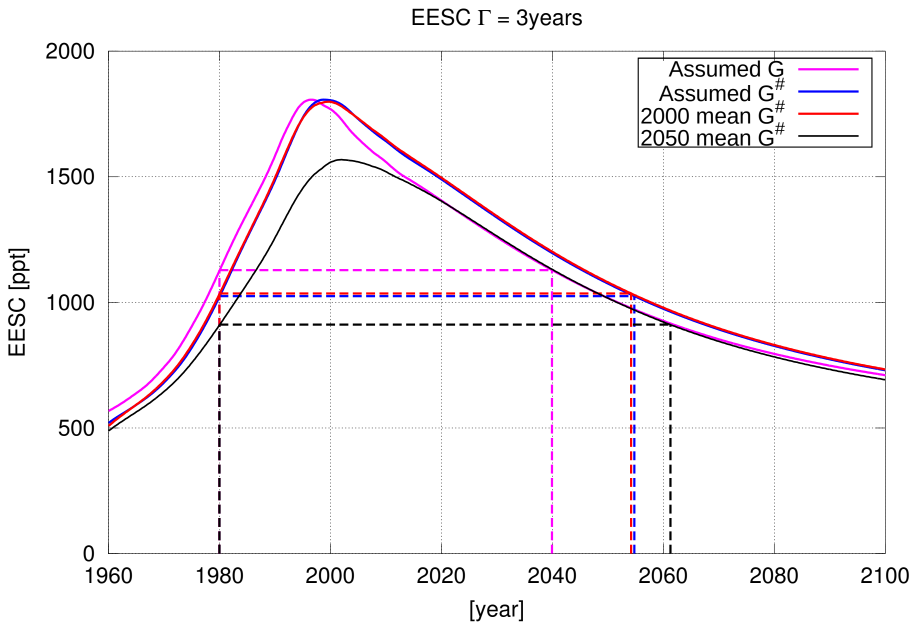

Figure 6.23: As Fig. 5.12, EESC for $\Gamma = 3$ years for assumed G and assumed and modeled $G^{\#}$, additionally the 2050 modeled $G^{\#}$.

resulting EESC being lower and peaking at later years. This understanding of the dependency of EESC and release time distribution was already considered at the end of Sec. 6.3 concerning the modeled and assumed $G^{\#}$. The apparent return date to 1980 EESC values shifts to 2061, if using the 2050 release time distribution, instead of 2054 for the 2000 release time distribution.

6.5 Discussion

The general line of thought of this chapter should now be wrapped up. First of all, by the explicit calculation of the transit time distribution for the individual species in this study, it is possible to quantify the impact of transport changes on source and product tracer mixing ratios. Hence, it could be seen, how the transport times in different regions are closely linked to the mixing ratios of the source tracers and their lifetime. The specifics of the mentioned regions will be considered in these closing remarks, while the general tendencies have already been presented.

In the extratropical lower stratosphere the differences in the streamfunction and mean AoA indicated the speeding up of the shallow branch of the BDC throughout the seasons. At the same time, a noticeable increase in local path integrated lifetime and a decrease in fractional release could be seen. The reduced time of residency leads to less depletion, as there are only weak sinks for the considered species in this region.

For species with noticeable tropospheric sinks (CH_3Cl, CH_3Br), a reduction in lifetime could be seen right above the tropopause that partly stretches into the aforementioned region of lower stratospheric increase in $\bar{\tau}$ (Fig. 6.19). As the fraction of air younger than 0.5 years increased in this region (apart from the MAM NH LMS) (Fig. 6.13), the reduction of lifetime is probably due to an enhanced influence of the tropospheric sinks with faster transport.

In the MAM NH LMS, a feature that shows opposite changes to the predominant changes could be seen across all considered measures, mixing ratio, mean AoA, fractions of old/young air, fractional release and path integrated lifetime. From those diagnostics and the transit time distributions (Fig. 6.20) it is clear, that the fraction of air that enters the region quickly (transit time shorter than 1 year) decreases. Accordingly the amount of older air increases. As the pathways for old air are typically following the deep branch of the residual circulation, those pathways are subject to considerable depletion. Consequently, compared to 2000 conditions, a larger fraction of the tracer is depleted, leading to an increase in fractional release and a decrease in local lifetime. Though, the question persists how specifically the fast pathway is weakened in 2050. A possible hypothesis would be that the strengthened subtropical jet (see Fig. 6.2) enhances the mixing barrier, inhibiting the in-mixing of young tropospheric air into the region.

Another very clear region with regards to all applied diagnostics is the SH SON polar region. As is already expected from established research, a delayed break-down of the polar vortex with ozone recovery is recognized [Ceppi and Shepherd, 2019]. In the mean AoA signal, we can see the increase in old air due to that delayed break-down. The air is still isolated as the polar night ends, and photolysis resumes. As source tracer richer air is inhibited from entering, the source tracer mixing ratio further decreases which leads to the particular decrease in mixing ratios that we see. This could also be recognized in increased fractional release and decreased lifetime. In the case of EESC, the resulting changes in the projected product mixing ratios could already be shown by the explicit determination of the transit time distributions (See Fig. 6.23).

Otherwise, the products that can be diagnosed directly are e.g. reactive chlorine, ClO_X or reactive bromine BrO_X. Here, ClO_X is considered, which is predominantly present in the SH polar vortex, as was explained in Sec. 2.2.2. The effects of the prolonged isolation and depletion in the SON SH polar region might even be visible in the relative change of ClO_X between 2000 and 2050, as given in Fig. 6.24. Despite the decrease of ODS emissions, a slight increase in ClO_X is apparent in the SON polar region, which is in line to the stable polar vortex with an decreased path integrated lifetime in 2050. Still, the equilibrium of the catalytic cycle and the strong tropospheric warming in the polar region, might also contribute to this change in ClO_X. Again, ClO_X is subject to further chemical processing, such that no distinct agreement between EESC and ClO_X is expected, especially since EESC is determined from the transient boundary condition time series while ClO_X is obtained directly from the time slice simulations.

Coming back to the discussion of the different regions, in the NH, the polar vortex becomes weaker in DJF with weakened gradient as was shown by the zonal mean zonal wind (Fig. 6.2). As the explanation of the signal in the different diagnostics requires some interpretation, it should be guided by the fact, that opposing effects to the SH polar vortex are anticipated, since the SH polar vortex strengthens while the NH vortex weakens. Therefore, the interpretation might be such, that due to the weaker vortex, more exchange between vortex air and outside air occurs. This means, that more old air which was more depleted can reach outside the vortex while younger, less depleted air enters the vortex. This then leads to the picture of relatively strong decrease in mean AoA in the polar vortex and weak decrease at the edge in DJF. Consequently, the mixing ratios of the source tracers are lower outside the vortex and higher inside. The change in fractions of input with a decrease inside the vortex and an increase follows this picture. Accordingly, the path integrated lifetime decreases along the vortex edge. Overall, because of weakened isolation, more potential for depletion is given, as

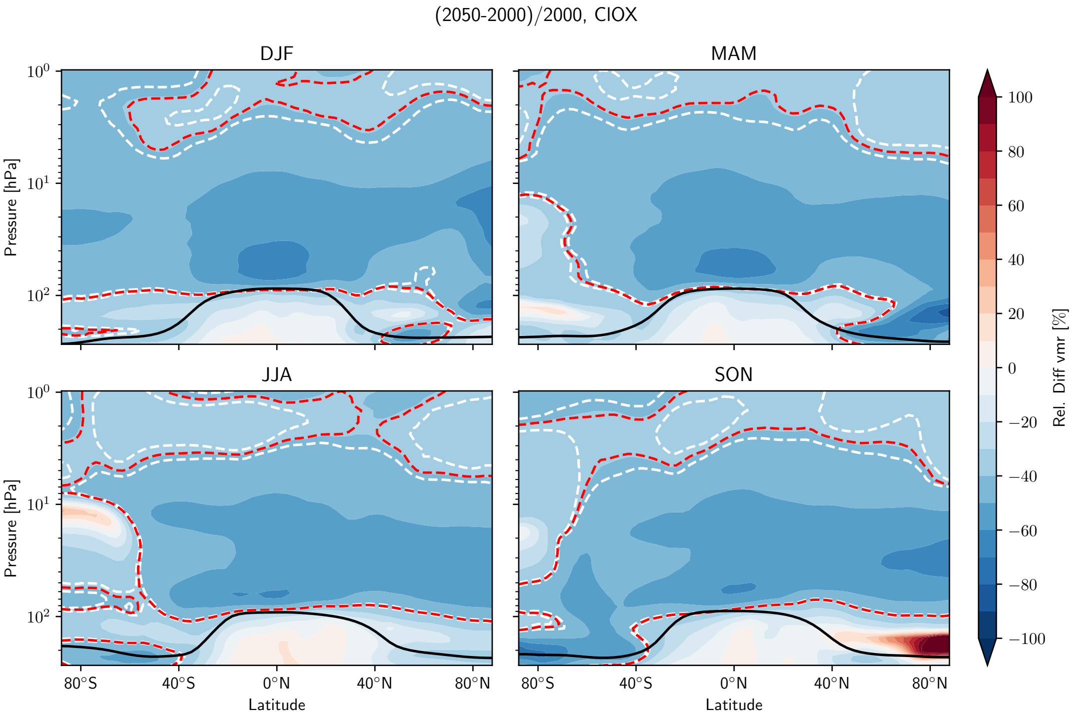

Figure 6.24: Seasonal relative change in ClO_X between 2000 and 2050. The red contour indicates the relative change in boundary conditions of chlorine containing species. The white contours indicate plus and minus 1% of that value.

air reaches illuminated regions and photolysis occurs. This would then lead to the decrease in mixing ratio overall in the NH polar region, as soon as the vortex breaks down in MAM. Also, the fraction of input increases and the local lifetime decreases throughout the region.

The respective changes in transport and depletion have shown to impact ODS and their products. Predominantly the mixing ratios of the projected source tracers are higher if the 2050 transport time distributions are considered while the mixing ratios of the product tracers are lower. This suggests, that the release of chlorine and bromine from ODS slows down due to the changes in transport. The total abundance of organic halogenated species injected into the stratosphere throughout the years is as the same in both calculations as the same boundary conditions are considered. Hence, a slowed down release of chlorine and bromine means, that while the release is slower, it persists for an extended amount of time. Whereat, the changes in the specific regions discussed in the previous paragraphs remain relevant for the projection of the source and product tracers. This clearly shows how valuable model studies are to facilitate an understanding of possible trends in distributions of tracers with chemical and radiative impact. Otherwise, typical product tracers that can be investigated, such as $\mathrm{ClO_X}$, are affected by both transport and further chemical processing. By means of the specifically determined transport time distributions, the impact of changed transport onto product tracers could be isolated.

Now, to put the results into perspective, two conclusive publications need to be mentioned, one being the review article about the BDC by [Butchart, 2014], the other being the Lifetimes Report by SPARC [Ko et al., 2013]. As of [WMO, 2018], most of the latter is still up-to-date.

It should be kept in mind, that this previous work relied on stratospheric or atmospheric lifetimes, rather than path integrated lifetime. This limits the comparability even though they are connected by integration (see also Chap. 5). Concerning ODS removal and a changing BDC, [Butchart, 2014] focuses on the work by [Butchart and Scaife, 2001] and [Douglass et al., 2008]. [Butchart and Scaife, 2001] find that the atmospheric lifetimes of CFC decrease as they are removed faster from the stratosphere due to increased mass exchange as the BDC accelerates using a GCM considering the period from 1992 to 2051. Often, this publication is cited in other work, to emphasize that a changing BDC can impact the removal of CFC. Considering several types of atmospheric models in simulations up to 2050 [Douglass et al., 2008] find, that the fractional release decreases in the middle and lower stratosphere which is offset by the increased influx of tropospheric air using a CCM. The decrease in (mean) fractional release is in agreement to what is in the present work. In the considered simulations they implemented the CFC as boundary condition mixing ratios, as was done here. However, they argue that the artificial surface flux introduced by the boundary condition mixing ratio impacts the apparent removal of the CFC. Similarly, [Cook and Roscoe, 2011] report a reduced burden and lifetime of ODS with increased BDS applying a simple model. In contrast, [Ko et al., 2013] conclude that even though boundary conditions lead to different tracer distributions and atmospheric burden compared to emissions, the lifetimes remain relatively unaffected. [Douglass et al., 2008] finds a noticeable model dependence in the relationship of mean AoA and fractional release. [Ko et al., 2013] state noticeable model dependence of the stratospheric lifetime of species that have stratospheric sinks, but report a clear correlation with the tropical mean AoA profile. For the period up to 2100 they report no clear trend between 2000 and 2100 in lifetime of tracers that are depleted in the stratosphere.

The existing work that predicts the effects of a changing BDC on ODS removal relies on simplified models or does not find clear trends in stratospheric lifetime. While the simple models are strong in attributing changes, the comprehensive models do not clearly show those connections. This illustrates the need, to understand the effects of transport changes onto tracer chemistry and distributions in a comprehensive environment. Further, the discussed model and implementation dependencies pose further challenges in separating the effects of changing transport and chemistry. At the same time, changes in processed tracers such as ozone or Cl_y require interpretation of the relevant process changes. Therefore, the present work provided further insight by implementing arrival time distributions. Based on changes in dynamics due to climate change, that are in accordance to state of the art understanding, a consistent interpretation of changes in tracer lifetime in separate regions of the stratosphere could be achieved. The regional investigation presented here, highlights differences in tracer lifetime and mixing ratios that were not documented so far. Though, it it clear, that the next step considering the transport time distribution approach would be to run it in a transient simulation with emissions rather than boundary condition mixing ratios.

CHAPTER 7

Concluding Remarks

Due to their radiative and chemical impact, it is important to understand the future distributions of tracers such as ODS in the stratosphere. This understanding relies on the understanding of dynamics and depletion. However, concerning the past evolution of tracer transport, differences in observation and model based AoA remained open questions, e.g. [Engel et al., 2017, Oberländer et al., 2013]. Along with that, as no realistic tracer is fully inert, the chemical processes need to be considered, too. An important measure of the chemical processing of a source tracer that is transported through the stratosphere is the fractional release. Though, the fractional release as defined [Ostermöller et al., 2017] has not yet been assessed in a CCM.

Therefore, the present work was focused on discussing atmospheric distributions of inert and chemically active tracers in a changing climate by means of transport time distributions. At this point, we return to the initial questions that were formulated to guide through this work to complete the considerations.

7.1 Summary and Conclusions

Are the currently used assumptions about the transport time distribution for an inert tracer valid? Are there systematic effects when deriving transport times (mean AoA) that result in uncertainties in trends?

To answer these questions, mean AoA and specifically its trend as a diagnostic of transport for inert tracers was discussed by the example of a SF_6 like tracer. Two methods to infer mean AoA from tracers based on the age spectrum with non-linear increasing boundary conditions, namely fit and convolution method, were discussed. It could be shown, that the apparent discrepancy in mean AoA trends in models and observations in [Engel et al., 2017, Engel et al., 2009] can be explained by the parameter selection when deriving mean AoA. The parameter selection is based on assumptions about the shape of the age spectrum. It could be shown that in the case of the fit method, SF_6 derived mean AoA values for both, observations and model, values shift to larger values the smaller the assumed ratio of moments and the larger the fraction of input, leading to a smaller negative or even positive trend. Similarly, it was presented, that when considering the convolution method, the same sensitivity in the beginning of the time series leads to the same systematic of small negative, respectively positive trends for smaller ratio of moments. As the observational trend was calculated using a relatively small ratio of moments (0.7 years) and a large fraction of input (98%), it became clear, that the mean AoA trend shifts to more negative, when applying a larger ratio of moments. In that case, the modeled and observed mean AoA trend agree within the margins of error. Further, it was discussed in context with other work and EMAC results, that such a larger ratio of moments might be more realistic. In general, recent research suggests age spectra which are broader, i.e. with a higher ratio of moments than 0.7 years, namely 1.25-2 years [Volk et al., 1997, Waugh et al., 1997, Ploeger and Birner, 2016]. Thus it can be said, that we can trust the negative mean AoA trends seen in EMAC and the present work contributed in resolving the long-lasting discrepancy of modeled and observed mean AoA trends by applying more appropriate assumptions about the age spectrum. Still, constraining the ratio of moments correctly from observations will require further research.

How do transport time distributions for chemically depleted tracers differ from those of inert tracers? How well do simple assumptions such as a path integrated lifetime hold?

For the first time, the transport time distributions of chemically depleted tracers and their products were explicitly calculated in a full three dimensional CCM (EMAC). The adequate description of the distribution of chemically depleted tracers by the transport time distributions could be confirmed in a three dimensional model. Specifically, it could be shown, that the assumption of a path integrated lifetime is suitable to describe the ratio between the age spectrum and arrival time distribution for most of the stratosphere, but not for the extratropical lower stratosphere. The simple approximations for the fractional release and transit time distribution in recent work on equivalent effective stratospheric chlorine could be discussed [Engel et al., 2018]. For the latter, in general, good agreement could be shown, though the impact of chemical loss appeared to be stronger in the simulation than in the simple assumption. The comparison to the measurements shown in [Leedham Elvidge et al., 2018] also made clear, that for a given mean AoA value, the assumed fractional release of a tracer seems to be smaller than the modeled. In the future, the obtained transit time distributions and the derived lifetimes and fractional release can be applied to aid in the interpretation of e.g. balloon or airborne measurements, as is clear by the discussion of the relation of mean fractional release and mean AoA in [Leedham Elvidge et al., 2018, Laube et al., 2013]. In addition, the availability of the path integrated lifetime from transit time distributions opens up further possibilities such as constraining the age spectrum itself (See first question and [Holzer and Waugh, 2015]).

What can transport time distributions tell about distributions of tracers and their products in a changing climate and how are they affected themselves?

Discussing the transit time distribution as a diagnostic tool in climate change scenarios allowed to attribute changes in tracer mixing ratio to changes in transport and chemistry separately for different regions of the stratosphere. Specifically, this compliments existing studies using simple models, that are strong in attributing [Butchart and Scaife, 2001, Cook and Roscoe, 2011], and using full CCM, that are aimed at providing a full picture [Ko et al., 2013]. For most of the stratosphere, the anticipated speeding up of the BDC in the future was seen, consistent with previous work [Abalos et al., 2019, Morgenstern et al., 2018]. This leads to a relative increase, respectively less relative decrease in source tracer mixing ratios, as less of them is yet depleted, which is also seen in the path integrated lifetime and the fractional release. This affects all transport time distributions irrespective of species. The regions in the stratosphere with opposing patterns of change could be discussed and explained, too. Overall, the link of features in the change of transport and chemical depletion resulting in certain tracer mixing ratio patterns could be well explained by means of transport time distribution diagnostics. Further, the changes seen in transport and depletion affect the expected tracer distributions in the future. Obtaining the transit time distributions of relevant ODS and N_2O in a high ODS levels and a future ODS scenario, provided detailed insight into the imposed changes in transport and chemistry onto ODS. The details of the recovery of the ozone layer in different regions are still subject to ongoing research [WMO, 2018]. Further, in the present work changes in diagnostics, such as EESC, were specifically determined, that are used in policy making. Probably most importantly, the results of this work point towards the possibility of a prolonged ozone hole in the SH high-latitudes which was possible to diagnose, as transit time distributions provide diagnostics of the combined effect of transport and depletion for separate regions.

7.2 Outlook

The results of this work concerning mean AoA trends from approximately inert tracer clearly show how beneficial the synergies of models and observations are. Models allow explicitly testing and constraining methods and assumptions applied to observations. This is particular relevant in applications such as transport time distributions where free parameters need to be constrained, to then derive further understanding.

The implementation of transport time distributions of chemical active tracers then complements the understanding of the combination of transport and depletion, which completes the range of possibilities to interpret realistic tracer distributions, as no realistic tracer is perfectly inert. The present work aids in closing gaps in the constraining of mean AoA, fractional release and lifetime based on tracer measurements. The insights of this work for constraining the age derivation from measurements are already considered in ongoing research [Linz et al., 2020].

Besides, the investigation of future projections showed what effect the changing climate might have on tracer distributions in certain regions. The observed spatial and temporal dependencies in the transit time distributions and derived measures obtained from the EMAC results highlight that simple assumptions do not provide the full picture and how important model simulations are in understanding the distribution of tracers in present and future climate. However, for a full interpretation, it would be highly interesting to do further research by e.g. considering a transient simulation. Further, it would be insightful, to test the transport time distributions of ODS prescribed by emissions rather than boundary condition mixing ratios. [Ko et al., 2013] stated that the shift from boundary condition mixing ratios to emissions changes tracer distributions but does not strongly impact lifetimes. But in the case of path integrated lifetime, the shift might have further impact. In addition, it would be of great interest to explore the link between the transport driven ODS changes and the changes in ozone.

Acronyms

List of used acronyms

AoA	Age of Air
BDC	Brewer-Dobson circulation
CCM	Chemistry-Climate Model
CCMI	Chemistry-Climate Model Initiative
CFC	Chlorofluorocarbons
CLaMS	Chemical Lagrangian Model of the Stratosphere
DJF	December January February
ECHAM	European Centre Hamburg general circulation model
EESC	Equivalent effective stratospheric chlorine
EMAC	ECHAM/MESSy Atmospheric Chemistry
ESCiMo	Earth System Chemistry integrated Modeling
ESM	Earth System Model
GHG	Green House Gases
HCFC	Hydrochlorofluorocarbon
JJA	June July August
LMS	Lowermost stratosphere
LS	Lower stratosphere
MAM	March April May
MESSy	Modular Earth Submodel System
ML	Mid-latitudes
NH	Northern hemisphere
ODS	Ozone depleting substances
PSC	Polar stratospheric clouds
QBO	Quasi Biennial Oscillation

SH	Southern hemisphere
SON	September October November
TEM	Transformed Eulerian mean
UTLS	Upper Troposphere Lower Stratosphere
UV	Ultraviolet

Bibliography

[Abalos et al., 2019] Abalos, M., Polvani, L., Calvo, N., Kinnison, D., Ploeger, F., Randel, W., and Solomon, S. (2019). New Insights on the Impact of Ozone–Depleting Substances on the Brewer–Dobson Circulation. *Journal of Geophysical Research: Atmospheres*, 124(5):2435–2451.

[Andrews et al., 2001] Andrews, A. E., Boering, K. A., Wofsy, S. C., Daube, B. C., Jones, D. B., Alex, S., Loewenstein, M., Podolske, J. R., and Strahan, S. E. (2001). Empirical age spectra for the midlatitude lower stratosphere from in situ observations of CO2: Quantitative evidence for a subtropical "barrier" to horizontal transport. *Journal of Geophysical Research: Atmospheres*, 106(D10):10257–10274.

[Andrews et al., 1987] Andrews, D., Holton, J., and Leovy, C. (1987). *Middle Atmosphere Dynamics*. International Geophysics. Elsevier Science.

[Ball et al., 2019] Ball, W. T., Alsing, J., Staehelin, J., Davis, S. M., Froidevaux, L., and Peter, T. (2019). Stratospheric ozone trends for 1985–2018: sensitivity to recent large variability. *Atmospheric Chemistry and Physics*, 19(19):12731–12748.

[Bönisch et al., 2011] Bönisch, H., Engel, A., Birner, T., Hoor, P., Tarasick, D. W., and Ray, E. A. (2011). On the structural changes in the Brewer–Dobson circulation after 2000. *Atmospheric Chemistry and Physics*, 11(8):3937–3948.

[Brewer, 1949] Brewer, A. W. (1949). Evidence for a world circulation provided by the measurements of helium and water vapour distribution in the stratosphere. *Quarterly Journal of the Royal Meteorological Society*, 75(326):351–363.

[Butchart, 2014] Butchart, N. (2014). The Brewer–Dobson circulation. *Reviews of Geophysics*, 52(2):157–184.

[Butchart and Scaife, 2001] Butchart, N. and Scaife, A. (2001). Removal of chlorofluorocarbons by increased mass exchange between stratosphere and troposphere in a changing climate. *Nature*, 410:799–802.

[Ceppi and Shepherd, 2019] Ceppi, P. and Shepherd, T. G. (2019). The role of the stratospheric polar vortex for the austral jet response to greenhouse gas forcing. *Geophysical Research Letters*, 46(12):6972–6979.

[Cook and Roscoe, 2011] Cook, P. A. and Roscoe, H. K. (2011). Changes in reactive stratospheric gases due to a change in brewer-dobson circulation: results from a simple model. *Atmospheric Science Letters*, 13(1):49–54.

[Daniel et al., 1995] Daniel, J. S., Solomon, S., and Albritton, D. L. (1995). On the evaluation of halocarbon radiative forcing and global warming potentials. *Journal of Geophysical Research: Atmospheres*, 100(D1):1271–1285.

[Dietmüller et al., 2017] Dietmüller, S., Garny, H., Plöger, F., Jöckel, P., and Cai, D. (2017). Effects of mixing on resolved and unresolved scales on stratospheric age of air. *Atmospheric Chemistry and Physics*, 17(12):7703–7719.

[Dobson et al., 1929] Dobson, G. M. B., Harrison, D. N., and Lawrence, J. (1929). Measurements of the amount of ozone in the earth's atmosphere and its relation to other geophysical conditions.-part II. *Proceedings of the Royal Society of London. Series A, Containing Papers of a Mathematical and Physical Character*, 122(790):456–486.

[Douglass et al., 2008] Douglass, A. R., Stolarski, R. S., Schoeberl, M. R., Jackman, C. H., Gupta, M. L., Newman, P. A., Nielsen, J. E., and Fleming, E. L. (2008). Relationship of loss, mean age of air and the distribution of CFCs to stratospheric circulation and implications for atmospheric lifetimes. *Journal of Geophysical Research*, 113(D14).

[Eichinger et al., 2019] Eichinger, R., Dietmüller, S., Garny, H., Šácha, P., Birner, T., Bönisch, H., Pitari, G., Visioni, D., Stenke, A., Rozanov, E., Revell, L., Plummer, D. A., Jöckel, P., Oman, L., Deushi, M., Kinnison, D. E., Garcia, R., Morgenstern, O., Zeng, G., Stone, K. A., and Schofield, R. (2019). The influence of mixing on the stratospheric age of air changes in the 21st century. *Atmospheric Chemistry and Physics*, 19(2):921–940.

[Engel et al., 2018] Engel, A., Bönisch, H., Ostermöller, J., Chipperfield, M. P., Dhomse, S., and Jöckel, P. (2018). A refined method for calculating equivalent effective stratospheric chlorine. *Atmospheric Chemistry and Physics*, 18(2):601–619.

[Engel et al., 2017] Engel, A., Bönisch, H., Ullrich, M., Sitals, R., Membrive, O., Danis, F., and Crevoisier, C. (2017). Mean age of stratospheric air derived from AirCore observations. *Atmospheric Chemistry and Physics*, 17(11):6825–6838.

[Engel et al., 2009] Engel, A., Möbius, T., Bönisch, H., Schmidt, U., Heinz, R., Levin, I., Atlas, E., Aoki, S., Nakazawa, T., Sugawara, S., et al. (2009). Age of stratospheric air unchanged within uncertainties over the past 30 years. *Nature Geoscience*, 2(1):28.

[Eyring et al., 2013] Eyring, V., Lamarque, J.-F., Hess, P., Arfeuille, F., Bowman, K., Chipperfield, M. P., Duncan, B., Fiore, A., Gettelman, A., Giorgetta, M., Granier, C., Hegglin, M., Kinnison, D., Kunze, M., Langematz, U., Luo, B., Martin, R., Matthes, K., Newman, P., Peter, T., Peter, T., Robock, A., Ryerson, T., Saiz-Lopez, A., Salawitch, R., Schultz, M., Shepherd, T. G., Shindell, D., Staehelin, J., Tegtmeier, S., Thomason, L., Tilmes, S., Vernier, J.-P., Waugh, D., and Young, P. (2013). Overview of IGAC/SPARC Chemistry-Climate Model Initiative (CCMI) Community Simulations in Support of Upcoming Ozone and Climate Assessments. Eyring et al. (2013), Overview of IGAC/SPARC Chemistry-Climate Model Initiative (CCMI) Community Simulations in Support of Upcoming Ozone and Climate Assessments, SPARC Newsletter no. 40, WMO-WRCP, Geneva, Switzerland, 48-66.

[Fritsch et al., 2019] Fritsch, F., Garny, H., Engel, A., Bönisch, H., and Eichinger, R. (2019). Sensitivity of age of air trends on the derivation method for non-linear increasing tracers. *Atmospheric Chemistry and Physics Discussions*, 2019:1–23.

[Garcia and Randel, 2008] Garcia, R. R. and Randel, W. J. (2008). Acceleration of the Brewer–Dobson Circulation due to Increases in Greenhouse Gases. *Journal of the Atmospheric Sciences*, 65(8):2731–2739.

[Garcia et al., 2011] Garcia, R. R., Randel, W. J., and Kinnison, D. E. (2011). On the Determination of Age of Air Trends from Atmospheric Trace Species. *Journal of the Atmospheric Sciences*, 68(1):139–154.

[Garny et al., 2014] Garny, H., Birner, T., Bönisch, H., and Bunzel, F. (2014). The effects of mixing on age of air. *Journal of Geophysical Research: Atmospheres*, 119(12):7015–7034.

[Giorgetta et al., 2002] Giorgetta, M. A., Manzini, E., and Roeckner, E. (2002). Forcing of the quasi-biennial oscillation from a broad spectrum of atmospheric waves. *Geophysical Research Letters*, 29(8):86–1–86–4.

[Haenel et al., 2015] Haenel, F. J., Stiller, G. P., von Clarmann, T., Funke, B., Eckert, E., Glatthor, N., Grabowski, U., Kellmann, S., Kiefer, M., Linden, A., and Reddmann, T. (2015). Reassessment of MIPAS age of air trends and variability. *Atmospheric Chemistry and Physics*, 15(22):13161–13176.

[Hall and Plumb, 1994] Hall, T. M. and Plumb, R. A. (1994). Age as a diagnostic of stratospheric transport. *Journal of Geophysical Research*, 99(D1):1059.

[Hauck et al., 2019] Hauck, M., Fritsch, F., Garny, H., and Engel, A. (2019). Deriving stratospheric age of air spectra using an idealized set of chemically active trace gases. *Atmospheric Chemistry and Physics*, 19(7):5269–5291.

[Holzer and Waugh, 2015] Holzer, M. and Waugh, D. W. (2015). Interhemispheric transit time distributions and path-dependent lifetimes constrained by measurements of SF 6 , CFCs, and CFC replacements. *Geophysical Research Letters*, 42(11):4581–4589.

[Jöckel et al., 2010] Jöckel, P., Kerkweg, A., Pozzer, A., Sander, R., Tost, H., Riede, H., Baumgaertner, A., Gromov, S., and Kern, B. (2010). Development cycle 2 of the Modular Earth Submodel System (MESSy2). *Geoscientific Model Development*, 3(2):717–752.

[Jöckel et al., 2005] Jöckel, P., Sander, R., Kerkweg, A., Tost, H., and Lelieveld, J. (2005). Technical Note: The Modular Earth Submodel System (MESSy) - a new approach towards Earth System Modeling. *Atmospheric Chemistry and Physics*, 5(2):433–444.

[Jöckel et al., 2006] Jöckel, P., Tost, H., Pozzer, A., Brühl, C., Buchholz, J., Ganzeveld, L., Hoor, P., Kerkweg, A., Lawrence, M., Sander, R., Steil, B., Stiller, G., Tanarhte, M., Taraborrelli, D., van Aardenne, J., and Lelieveld, J. (2006). The atmospheric chemistry general circulation model ECHAM5/MESSy1: consistent simulation of ozone from the surface to the mesosphere. *Atmospheric Chemistry and Physics*, 6(12):5067–5104.

[Jöckel et al., 2016] Jöckel, P., Tost, H., Pozzer, A., Kunze, M., Kirner, O., Brenninkmeijer, C. A. M., Brinkop, S., Cai, D. S., Dyroff, C., Eckstein, J., Frank, F., Garny, H., Gottschaldt, K.-D., Graf, P., Grewe, V., Kerkweg, A., Kern, B., Matthes, S., Mertens, M., Meul, S., Neumaier, M., Nützel, M., Oberländer-Hayn, S., Ruhnke, R., Runde, T., Sander, R., Scharffe, D., and Zahn, A. (2016). Earth System Chemistry integrated Modelling (ESCiMo) with the Modular Earth Submodel System (MESSy) version 2.51. *Geoscientific Model Development*, 9(3):1153–1200.

[Kawase et al., 2011] Kawase, H., Nagashima, T., Sudo, K., and Nozawa, T. (2011). Future changes in tropospheric ozone under representative concentration pathways (rcps). *Geophysical Research Letters*, 38(5).

[Ko et al., 2013] Ko, M. K. W., Newman, P. A., Reimann, S., and Strahan, S. E., editors (2013). *SPARC Report on Lifetimes of Stratospheric Ozone-Depleting Substances, Their Replacements, and Related Species*, volume No. 6. SPARC Office.

[Labitzke, 2007] Labitzke, K. (2007). Solar Variation and Stratospheric Response. *Space Science Reviews*, 125(1-4):247–260.

[Laube et al., 2013] Laube, J. C., Keil, A., Bönisch, H., Engel, A., Röckmann, T., Volk, C. M., and Sturges, W. T. (2013). Observation-based assessment of stratospheric fractional release, lifetimes, and ozone depletion potentials of ten important source gases. *Atmospheric Chemistry and Physics*, 13(5):2779–2791.

[Leedham Elvidge et al., 2018] Leedham Elvidge, E., Bönisch, H., Brenninkmeijer, C. A. M., Engel, A., Fraser, P. J., Gallacher, E., Langenfelds, R., Mühle, J., Oram, D. E., Ray, E. A., Ridley, A. R., Röckmann, T., Sturges, W. T., Weiss, R. F., and Laube, J. C. (2018). Evaluation of stratospheric age of air from CF_4, C_2F_6, C_3F_8, CHF_3, HFC-125, HFC-227ea and SF_6; implications for the calculations of halocarbon lifetimes, fractional release factors and ozone depletion potentials. *Atmospheric Chemistry and Physics*, 18(5):3369–3385.

[Levin et al., 2010] Levin, I., Naegler, T., Heinz, R., Osusko, D., Cuevas, E., Engel, A., Ilmberger, J., Langenfelds, R. L., Neininger, B., Rohden, C. v., Steele, L. P., Weller, R., Worthy, D. E., and Zimov, S. A. (2010). The global SF_6 source inferred from long-term high precision atmospheric measurements and its comparison with emission inventories. *Atmospheric Chemistry and Physics*, 10(6):2655–2662.

[Li et al., 2018] Li, F., Newman, P., Pawson, S., and Perlwitz, J. (2018). Effects of greenhouse gas increase and stratospheric ozone depletion on stratospheric mean age of air in 1960-2010. *Journal of Geophysical Research: Atmospheres*, 123(4):2098–2110.

[Li et al., 2012] Li, F., Waugh, D. W., Douglass, A. R., Newman, P. A., Pawson, S., Stolarski, R. S., Strahan, S. E., and Nielsen, J. E. (2012). Seasonal variations of stratospheric age spectra in the Goddard Earth Observing System Chemistry Climate Model (GEOSCCM). *Journal of Geophysical Research: Atmospheres*, 117(D5).

[Linz et al., 2020] Linz, M., Birner, B., Plumb, A., Gerber, E., Haenel, F., Stiller, G., Kinnison, D., and Neu, J. (2020). Age of air in the stratosphere from observations. European Geosience Union General Assembly.

[Linz et al., 2017] Linz, M., Plumb, R. A., Gerber, E. P., Haenel, F. J., Stiller, G., Kinnison, D. E., Ming, A., and Neu, J. L. (2017). The strength of the meridional overturning circulation of the stratosphere. *Nature Geoscience*, 10(9):663–667.

[Maiss and Levin, 1994] Maiss, M. and Levin, I. (1994). Global increase of SF6 observed in the atmosphere. *Geophysical Research Letters*, 21(7):569–572.

[Manzini et al., 2014] Manzini, E., Karpechko, A. Y., Anstey, J., Baldwin, M. P., Black, R. X., Cagnazzo, C., Calvo, N., Charlton-Perez, A., Christiansen, B., Davini, P., Gerber, E., Giorgetta, M., Gray, L., Hardiman, S. C., Lee, Y.-Y., Marsh, D. R., McDaniel, B. A., Purich, A., Scaife, A. A., Shindell, D., Son, S.-W., Watanabe, S., and Zappa, G. (2014). Northern winter climate change: Assessment of uncertainty in CMIP5 projections related to stratosphere-troposphere coupling. *Journal of Geophysical Research: Atmospheres*, 119(13):7979–7998.

[McIntyre and Palmer, 1984] McIntyre, M. E. and Palmer, T. N. (1984). The 'surf zone' in the stratosphere. *Journal of Atmospheric and Terrestrial Physics*, 46(9):825–849.

[Molina and Rowland, 1974] Molina, M. J. and Rowland, F. S. (1974). Stratospheric sink for chlorofluoromethanes: chlorine atom-catalysed destruction of ozone. *Nature*, 249(5460):810–812.

[Morgenstern et al., 2017] Morgenstern, O., Hegglin, M. I., Rozanov, E., O'Connor, F. M., Abraham, N. L., Akiyoshi, H., Archibald, A. T., Bekki, S., Butchart, N., Chipperfield, M. P., Deushi, M., Dhomse, S. S., Garcia, R. R., Hardiman, S. C., Horowitz, L. W., Jöckel, P., Josse, B., Kinnison, D., Lin, M., Mancini, E., Manyin, M. E., Marchand, M., Marécal, V., Michou, M., Oman, L. D., Pitari, G., Plummer, D. A., Revell, L. E., Saint-Martin, D., Schofield, R., Stenke, A., Stone, K., Sudo, K., Tanaka, T. Y., Tilmes, S., Yamashita, Y., Yoshida, K., and Zeng, G. (2017). Review of the global models used within phase 1 of the Chemistry–Climate Model Initiative (CCMI). *Geoscientific Model Development*, 10(2):639–671.

[Morgenstern et al., 2018] Morgenstern, O., Stone, K. A., Schofield, R., Akiyoshi, H., Yamashita, Y., Kinnison, D. E., Garcia, R. R., Sudo, K., Plummer, D. A., Scinocca, J., Oman, L. D., Manyin, M. E., Zeng, G., Rozanov, E., Stenke, A., Revell, L. E., Pitari, G., Mancini, E., Di Genova, G., Visioni, D., Dhomse, S. S., and Chipperfield, M. P. (2018). Ozone sensitivity to varying greenhouse gases and ozone-depleting substances in CCMI-1 simulations. *Atmospheric Chemistry and Physics*, 18(2):1091–1114.

[Newman et al., 2007] Newman, P. A., Daniel, J. S., Waugh, D. W., and Nash, E. R. (2007). A new formulation of equivalent effective stratospheric chlorine (EESC). *Atmospheric Chemistry and Physics*, 7(17):4537–4552.

[Newman et al., 2006] Newman, P. A., Nash, E. R., Kawa, S. R., Montzka, S. A., and Schauffler, S. M. (2006). When will the antarctic ozone hole recover? *Geophysical Research Letters*, 33(12).

[Oberländer et al., 2013] Oberländer, S., Langematz, U., and Meul, S. (2013). Unraveling impact factors for future changes in the Brewer–Dobson circulation. *Journal of Geophysical Research: Atmospheres*, 118(18):10,296–10,312.

[Oberländer-Hayn et al., 2015] Oberländer-Hayn, S., Meul, S., Langematz, U., Abalichin, J., and Haenel, F. (2015). A chemistry-climate model study of past changes in the brewer-dobson circulation. *Journal of Geophysical Research: Atmospheres*, 120(14):6742–6757.

[Ostermöller et al., 2017] Ostermöller, J., Bönisch, H., Jöckel, P., and Engel, A. (2017). A new time-independent formulation of fractional release. *Atmospheric Chemistry and Physics*, 17(6):3785–3797.

[Ploeger and Birner, 2016] Ploeger, F. and Birner, T. (2016). Seasonal and inter-annual variability of lower stratospheric age of air spectra. *Atmospheric Chemistry and Physics*, 16(15):10195–10213.

[Plumb et al., 1999] Plumb, I. C., Vohralik, P. F., and Ryan, K. R. (1999). Normalization of correlations for atmospheric species with chemical loss. *Journal of Geophysical Research: Atmospheres*, 104(D9):11723–11732.

[Polvani et al., 2020] Polvani, L. M., Previdi, M., England, M. R., Chiodo, G., and Smith, K. L. (2020). Substantial twentieth-century arctic warming caused by ozone-depleting substances. *Nature Climate Change*, 10(2):130–133.

[Polvani et al., 2019] Polvani, L. M., Wang, L., Abalos, M., Butchart, N., Chipperfield, M. P., Dameris, M., Deushi, M., Dhomse, S. S., Jöckel, P., Kinnison, D., Michou, M., Morgenstern, O., Oman, L. D., Plummer, D. A., and Stone, K. A. (2019). Large impacts, past and future, of ozone-depleting substances on brewer-dobson circulation trends: A multimodel assessment. *Journal of Geophysical Research: Atmospheres*, 124(13):6669–6680.

[Prather, 2007] Prather, M. J. (2007). Lifetimes and time scales in atmospheric chemistry. *Philosophical Transactions of the Royal Society A: Mathematical, Physical and Engineering Sciences*, 365(1856):1705–1726.

[Ray et al., 2017] Ray, E. A., Moore, F. L., Elkins, J. W., Rosenlof, K. H., Laube, J. C., Röckmann, T., Marsh, D. R., and Andrews, A. E. (2017). Quantification of the SF6 lifetime based on mesospheric loss measured in the stratospheric polar vortex. *Journal of Geophysical Research: Atmospheres*, 122(8):4626–4638.

[Ray et al., 2014] Ray, E. A., Moore, F. L., Rosenlof, K. H., Davis, S. M., Sweeney, C., Tans, P., Wang, T., Elkins, J. W., Bönisch, H., Engel, A., Sugawara, S., Nakazawa, T., and Aoki, S. (2014). Improving stratospheric transport trend analysis based on SF_6 and CO_2 measurements. *Journal of Geophysical Research: Atmospheres*, 119(24):14,110–14,128.

[Rayner et al., 2003] Rayner, N. A., Parker, D. E., Horton, E. B., Folland, C. K., Alexander, L. V., Rowell, D. P., Kent, E. C., and Kaplan, A. (2003). Global analyses of sea surface temperature, sea ice, and night marine air temperature since the late nineteenth century. *Journal of Geophysical Research: Atmospheres*, 108(D14).

[Roeckner et al., 2006] Roeckner, E., Brokopf, R., Esch, M., Giorgetta, M., Hagemann, S., Kornblueh, L., Manzini, E., Schlese, U., and Schulzweida, U. (2006). Sensitivity of Simulated Climate to Horizontal and Vertical Resolution in the ECHAM5 Atmosphere Model. *Journal of Climate*, 19(16):3771–3791.

[Schoeberl et al., 2005] Schoeberl, M. R., Douglass, A. R., Polansky, B., Boone, C., Walker, K. A., and Bernath, P. (2005). Estimation of stratospheric age spectrum from chemical tracers. *Journal of Geophysical Research*, 110(D21).

[Shepherd, 2014] Shepherd, T. (2014). Atmospheric circulation as a source of uncertainty in climate change projections. *Nature Geoscience*, 7:703–708.

[Shepherd and McLandress, 2011] Shepherd, T. G. and McLandress, C. (2011). A Robust Mechanism for Strengthening of the Brewer-Dobson Circulation in Response to Climate Change: Critical-Layer Control of Subtropical Wave Breaking. *Journal of the Atmospheric Sciences*, 68(4):784–797.

[Stiller et al., 2012] Stiller, G. P., von Clarmann, T., Haenel, F., Funke, B., Glatthor, N., Grabowski, U., Kellmann, S., Kiefer, M., Linden, A., Lossow, S., and López-Puertas, M. (2012). Observed temporal evolution of global mean age of stratospheric air for the 2002 to 2010 period. *Atmospheric Chemistry and Physics*, 12(7):3311–3331.

[Thompson et al., 2015] Thompson, D. W. J., Barnes, E. A., Deser, C., Foust, W. E., and Phillips, A. S. (2015). Quantifying the Role of Internal Climate Variability in Future Climate Trends. *Journal of Climate*, 28(16):6443–6456.

[Volk et al., 1997] Volk, C. M., Elkins, J. W., Fahey, D. W., Dutton, G. S., Gilligan, J. M., Loewenstein, M., Podolske, J. R., Chan, K. R., and Gunson, M. R. (1997). Evaluation of source gas lifetimes from stratospheric observations. *Journal of Geophysical Research: Atmospheres*, 102(D21):25543–25564.

[Waugh et al., 1997] Waugh, D. W., Hall, T. M., Randel, W. J., Rasch, P. J., Boville, B. A., Boering, K. A., Wofsy, S. C., Daube, B. C., Elkins, J. W., Fahey, D. W., Dutton, G. S., Volk, C. M., and Vohralik, P. F. (1997). Three-dimensional simulations of long-lived tracers using winds from MACCM2. *Journal of Geophysical Research: Atmospheres*, 102(D17):21493–21513.

[WMO, 2018] WMO (2018). *Scientific Assessment of Ozone Depletion: 2018, Global Ozone Research and Monitoring Project - Report No. 58.* WMO (World Meteorological Organization), Geneva, Switzerland.

[Yang et al., 2018] Yang, H., Waugh, D. W., and Holzer, M. (2018). Decoupling the effects of transport and chemical loss on tropospheric composition: A model study of path-dependent lifetimes. *Journal of Geophysical Research: Atmospheres*, 123(4):2320–2335.

[Young et al., 2013] Young, P. J., Archibald, A. T., Bowman, K. W., Lamarque, J.-F., Naik, V., Stevenson, D. S., Tilmes, S., Voulgarakis, A., Wild, O., Bergmann, D., Cameron-Smith, P., Cionni, I., Collins, W. J., Dalsøren, S. B., Doherty, R. M., Eyring, V., Faluvegi, G., Horowitz, L. W., Josse, B., Lee, Y. H., MacKenzie, I. A., Nagashima, T., Plummer, D. A., Righi, M., Rumbold, S. T., Skeie, R. B., Shindell, D. T., Strode, S. A., Sudo, K., Szopa, S., and Zeng, G. (2013). Pre-industrial to end 21st century projections of tropospheric ozone from the atmospheric chemistry and climate model intercomparison project (ACCMIP). *Atmospheric Chemistry and Physics*, 13(4):2063–2090.

Danksagung

Dank sei zunächst Hella Garny ausgesprochen für die Möglichkeit, die Arbeit anzufertigen, sie auf Konferenzen zu präsentieren, und die Betreuung und Begutachtung. Ein Dank geht auch an Thomas Birner für den Input zur Arbeit und das Zweitgutachten.

Den Kollegen der Abteilung ESM (und EVA) sei für die angenehme Arbeitsatmophäre. Besonders gedankt sei dabei Martin Dameris für seinen Beitrag zum Gelingen dieser Arbeit. Des Weiteren möchte ich Patrick Jöckel, Roland Eichinger und Franziska Winterstein für die technische Unterstützung danken. Speziell seien auch meine Bürokollegen erwähnt, die für angenehme Ablenkung gesorgt haben. Harald Bönisch gilt ein Dank für den interessanten und hilfreichen fachliche Input. Dank gilt auch den Kollegen am FZJ, die die Zeit fachlich bereichert haben.

Danke auch an Freunde und Familie. Dabei sei Christoph erwähnt, für seine Tipps zum fertig schreiben. Annette und Ernst für ihre anhaltende Unterstützung.

Danke auch an Mariano für sein schier endloses Unterstützungsvermögen.